



Magma Vesiculation and Nature of the Explosive Activity in the 2011 Grímsvötn Eruption

Rebecca A. Lynch



Faculty of Earth Sciences
University of Iceland
2015

MAGMA VESICULATION AND NATURE OF THE EXPLOSIVE ACTIVITY IN THE 2011 GRÍMSVÖTN ERUPTION

Rebecca A. Lynch

60 ECTS thesis submitted in partial fulfillment of a
Magister Scientiarum degree in Geology

Advisor

Professor Þorvaldur Þórðarson

External Examiner

Dr. John A. Stevenson

M.Sc. committee

Professor Þorvaldur Þórðarson

Professor Bruce F. Houghton

Faculty of Earth Sciences

School of Engineering and Natural Sciences

University of Iceland

Reykjavik, May 2015

Magma Vesiculation and Nature of the Explosive Activity in the 2011 Grímsvötn Eruption

The 2011 eruption of Grímsvötn volcano, Iceland

60 ECTS thesis submitted in partial fulfillment of a M.Sc. degree in Geology

Copyright © 2015 Rebecca A. Lynch

All rights reserved

Faculty of Earth Sciences

School of Engineering and Natural Sciences

University of Iceland

Sturlugata 7, Askja

101, Reykjavík, Reykjavík

Iceland

Telephone: 525 4000

Bibliographic information:

Rebecca A. Lynch, 2015, Magma Vesiculation and Nature of the Explosive Activity in the 2011 Grímsvötn Eruption, M.Sc. thesis, Faculty of Earth Sciences, University of Iceland.

ISBN XX

Printing: Háskólaprent, Fálkagata 2, 107 Reykjavík
Reykjavík, Iceland, May 2015

Abstract

Grímsvötn is a basaltic, subglacial volcano and is the most active volcano in Iceland. It is known for phreatomagmatism and historically large fissure eruptions from its associated fissure swarm. The Grímsvötn central volcano erupted in 2004 from vents in the SW corner of the caldera, and again in 2011 from the same vent with more explosive intensity, magma volume and up to 19km-high eruption plume, suggesting an event of Plinian intensity. The deposits of the 2011 eruption consists of six alternating pumice lapilli and ash-grade units that raise questions about the potential role of magma outgassing in driving fragmentation and about the explosive nature of the 2011 eruption. To assess the degassing and fragmentation characteristics of this eruption, density measurements of 1200 clasts, from 12 samples spread across the three pumice lapilli units and quantitative image analysis were performed for four selected clasts from the lapilli units. The mean vesicularities are uniform, between 78.8% and 87.8%, indicating a degassed and fully expanded magma column upon magma disintegration. This high level of vesicularity resulted in convoluted bubble textures. Bubble-to-bubble interaction resulted in significant bubble coalescence, thin vesicle walls and collapse, as well as the formation of possible tube-like degassing pathways. The highly expanded and effective degassed magma column indicates volatile driven disintegration of the magma upon eruption. However, the alternating lapilli pumice and ash-grade units can be explained by (i) changes in eruption intensity or (ii) two stages of fragmentation, where an initial fragmentation to predominantly lapilli-size pumices is driven by expansion of magmatic gases (i.e. dry eruption) and a second-stage fragmentation induced by (a) passive (quenched fragmentation) or (b) explosive (fuel-coolant-like) interaction of magma and external water.

Útdráttur

Grímsvötn er basalt megineldstöð undir Vatnajökli og tilheyrir samnefndu eldstöðvakerfi. Hún er ein virkasta eldstöð landsins og þekkt fyrir sín freatómagmatísku sprengigos. Eitt mesta gos Íslandssögunar, Skaftáreldar, átti sér stað á sprungusveim Grímsvatnakerfisins árið 1783. Lítið sprengigos varð í gíg í suðvesturhorni Grímsvatnaöskjunnar árið 2004. Sami gígur gaus árið 2011, en nú með mun meiri ofsa og framleiddi stærðargráðunni meira af basískri gjósku. Gosmökkurinn í þessu sprengigosi steig í allt að 19 km hæð, sem gefur til kynna að aflið í gosinu var sem samsvarar plínísku gosi. Gjóska sem myndaðist í gosinu samanstendur af sex einingum, þar sem þrjár vikureiningar skiptast á við þrjár öskuríkar einingar. Þessar einingar, sér í lagi vikurlögin, vekja spurningar um framlag kvikugasa og afgösunar til sundrunar á kvikunni og afslins sem keyrði gosið áfram. Leitast er til að svara þessum spurningum með því að mæla ákveðna eðliseiginleika vikurkornanna, nefnilega rúmþyngd (= blöðrumagn) þeirra ásamt stærðardreifingu blaðra í völdum vikurkornum. Í heildina var rúmþyngd 1200 vikurkorna var mæld. Vikurkornin eru frá 12 sýnum (100 korn/sýni) sem ná yfir allar vikureiningarnar. Blöðrustærðardreifingin var mæld með myndgreiningu á fjórum vandlega völdum kornum, sem ná einnig yfir allar vikureiningarnar. Blöðrumagn vikurkornanna er hátt og einsleitt. Það spannar bilið 78.8% til 87.8%, sem gefur til kynna að kvikan sem myndaði vikureiningarnar var fullþanin vegna afgösunar þegar hún sundraðist efst í gosrásinni. Blöðrumynstrið í vikurkornunum er flókið og sýnir að vöxtur og árekstrar blaðra á milli leiddu til verulegs blöðrusamruna, afmyndunar á formi blaðranna ásamt myndun rörlaga holrýma sem hugsanlega eru megin afgösunarpípurnar. Hátt blöðrumagn (vesicularity), stærðardreifing (vesicle size distribution) og fjöldapétteleiki (vesicle number density) gefur sterklega til kynna að sundrun kvikunnar og sprengivirknin í fösunum sem mynduðu vikureiningarnar í 2011 gosinu var keyrð áfram af útleysingu og þennslu kvikugasa. Þessi afgösun kemur til vegna þrýstifalls í gosrásinni þegar kvikan rís hratt til yfirborðs. Aftur á móti, skýrir þetta ekki myndun öskuríku eininganna. En sú þríendurtekna skipting í vikur- og öskuríkar einingar sem einkennir 2011 gjóskuna er hægt að skýra á tvennan hátt (i) með því að breyta afli gossins, þar sem vikuríku einingarnar myndast við ofsafengnari sprengivirkni en þær öskuríku eða (ii) með tveggja stiga sundrun á kvikunni, þar sem upphafsstigið er vikurmyndun sem er keyrð áfram af afgösun og þennslu kvikugasa og seinna stig sundrunar sem felur í sér samspil utanðkomandi vatns og kviku, þar sem sundrun kvikunnar getur verið keyrð áfram af (a) hraðkælingu (passive quenched fragmentation) eða (b) tætingu í tengslum við hvellsuðu vatns í beinu sambandi við kviku (þ.e. fuel-coolant interactions).

Contents

List of Figures	ix
List of Tables	xi
Variables and Abbreviations	xiii
Acknowledgements	xvii
1. Introduction	1
2. Geology of Iceland	3
2.1. Origin of Iceland	3
2.2. Volcanic zones and their products	5
3. Grímsvötn	9
3.1. Grímsvötn Volcanic System	9
3.2. The 2011 Grímsvötn eruption	15
4. Magmatic volatiles and fragmentation	21
4.1. Density measurement techniques	24
4.2. Other ways of assessing degassing processes	25
5. Methodology	27
5.1. Field sampling	27
5.2. Density and vesicularity measurements	28
5.2.1. Selecting representative samples	31
5.3. Preparing the samples for imaging	31
5.4. Image strategy and acquisition	32
5.5. Image rectification	36
5.6. ImageJ	38
5.6.1. Software analysis	38
5.6.2. Data organization	39
6. Results	47
6.1. Stratigraphy	47
6.2. Density and vesicularity measurements	52

Contents

6.3. Image analyses	58
6.3.1. Vesicle size distribution	60
6.3.2. Vesicle volume distribution	60
6.3.3. Vesicle number density	63
7. Discussion	67
8. Conclusions	73
References	77
A. Appendix	93

List of Figures

2.1. Bathymetry map of the North Atlantic	4
2.2. Geological map of Iceland	5
3.1. Maps of study area	13
3.2. GPS vertical displacement at Grímsvötn caldera rim	14
3.3. Earthquake activity at Grímsvötn caldera, 1994-2007	14
3.4. Seismic tremor and earthquakes during the 2011 Grímsvötn eruption	15
3.5. GPS measurements from Grímsvötn caldera, 1997-2013	16
3.6. Grímsvötn 2011 ash dispersal map	19
3.7. Grímsvötn 2011 SO_2 cloud map	19
4.1. Solubility of H_2O and CO_2	21
4.2. Processes of volatiles in the conduit	23
5.1. G2011 sampled section	27
5.2. Grid nest vs exponential nest imaging approach	34
5.3. 11 image exponential nest	34
5.4. Induced error and minimum vesicle size	36
5.5. Example of SEM imaging process	37

LIST OF FIGURES

6.1. Eruption column height with time	47
6.2. Stratigraphic column, G2011 deposit (1 of 2)	50
6.3. Stratigraphic column, G2011 deposit (2 of 2)	51
6.4. Measured mean density	53
6.5. Calculated mean vesicularity	53
6.6. Density and vesicularity histograms (1 of 3)	54
6.7. Density and vesicularity histograms (2 of 3)	55
6.8. Density and vesicularity histograms (2 of 2)	56
6.9. Decoalesced SEM images	59
6.10. Vesicle size distribution	61
6.11. Vesicle volume distribution with mode analyses	62
6.12. Vesicle number density vs vesicularity	64
6.13. Mass discharge rates vs vesicle number density	65

List of Tables

2.1. 30 volcanic systems of Iceland	7
3.1. Eruption history of Grímsvötn Volcanic System	11
3.2. Timeline of Grímsvötn 2011 eruption	18
6.1. Plume height and mass discharge rate	49
6.2. Mean density and mean vesicularity	52
6.3. SEM imaged clasts	58
6.4. Number density of vesicles	63
A.1. Vesicularity values	93

Variables and Abbreviations

A_p : Total image area in pixels (pixels^2)

A_R : Reference area (mm^2)

A_{RM} : Reference area for the magnification (mm^2)

A_{RMT} : Total area from the images in the reference magnification (mm^2)

a.s.l.: Above sea level

A_T : Total image area in mm (mm^2)

A_v : Area of the vesicle (mm^2)

BND : Bubble number density

CVSD : Cumulative vesicle size distribution

CVVD : Cumulative vesicle volume distribution

EqD : Equivalent diameter of a vesicle (mm)

EVZ : East Volcanic Zone

F_a : Adjusted volume fraction

f_{bin} : Frequency of vesicles in the bin (unitless)

F_v : Volume fraction

G2011 : Grímsvötn 2011

G_e : Edge-vesicles mean greyscale value (unitless)

GIMP : GNU Image Manipulation Program

Variables and Abbreviations

G_p : Phenocryst greyscale value (unitless)

GRIM : Continuous GPS station located on Grímsfjall, the nunatak at the top of the caldera rim of Grímsvötn central volcano

G_v : Vesicles mean greyscale value for all vesicles in image (unitless)

GVS : Grímsvötn Volcanic System

H : plume height (km)

Hbar : Mean projected height by a spinning particle about a randomly oriented axis that changes (mm)

IMO : Icelandic Meteorological Office

KR : Kolbeinsey Ridge

m : Mass (g)

MAR : Mid-Atlantic Ridge

MFCI: Molten-fuel-coolant interaction

MIB : Mid-Iceland Belt

MORB : Mid-ocean ridge basalts

NA : Number density of vesicles (mm^{-2})

$(NA)_B$: Bulk number of vesicles for a unit area (mm^{-2})

NA_{bin} : Number of vesicles in the bin per unit area (mm^{-2})

$(NA)_P$: Number of vesicles per unit area (in a particular bin), adjusted for phenocrysts (mm^{-2})

NA_T : Total vesicles per area of the clast (mm^{-2})

n_f : Number of pieces of wax film used on clast

NV : Number density of vesicles per unit volume (mm^{-3})

NV>L : NV greater than vesicle size

NVm : Number density of vesicles per unit volume adjusted for melt (mm^{-3})

NVZ : North Volcanic Zone

ÖVB : Öräfi Volcanic Belt

P_f : phenocryst fraction (unitless)

Q : dense rock equivalent discharge rate (m^3/s)

RR : Reykjanes Ridge

RVB : Reykjanes Volcanic Belt

SEM : Scanning Electron Microscope

SF : Scale factor (pixels/mm)

SG_c : Specific gravity of the clast

SISZ : South Iceland Seismic Zone

SVB : Snæfellsnes Volcanic Belt

TFZ : Tjörnes Fracture Zone

USGS : U.S. Geological Survey

v : Volume (ml)

V : Vesicularity (%)

V_f : Vesicle fraction (unitless)

VG/VL : Volumetric ratio of vesicles (G, gas) to melt (L, liquid)

V_I : Vesicles included in reference area

Vol_s : Volume of sphere with equivalent diameter of Hbar (mm^3)

VSD : Vesicle size distribution

V_v : Percentage of vesicles by volume (%)

Variables and Abbreviations

VVD : Vesicle volume distribution

w_a : Weight of clast in air (g)

w_b : Weight of ballast (g)

w_f : Weight of wax film (g)

WVZ : West Volcanic Zone

w_w : Weight of clast in water on ballast (g)

x : Class size number

XRCMT : X-ray computed microtomography

α : Alpha values(unitless)

ρ : Density (g/ml)

ρ_c : Density of the clast (g/cm^3)

ρ_w : Density of water (g/cm^3)

ρ_{DRE} : Density of DRE (g/cm^3)

Acknowledgements

This thesis would not have come together in this form if it were not for the help I have received along the way.

From the University of Iceland, many thanks to Jónas Guðnason for collecting the samples in the first place and for taking the time to help me at the beginning of the lab work and with using the SEM. I am very grateful for the help of Sigurður Jakobsson, as he spent many days helping to find the best way to prepare the samples and was invaluable at this stage of the project. A great deal of thanks also to Will Moreland, for kindly answering my countless questions about ImageJ.

A special thanks to Þorvaldur Þórðarson for his supervision, ideas and support throughout the project. I'd also like to thank Bruce Houghton for his time and kindness. It was a privilege to have his advice. Many kind thanks to John Stevenson for reviewing the thesis and coming to Iceland for the defence.

An integral part of my support team and the reason this thesis is complete and on schedule, my boyfriend Sven deserves more than my humble thanks. Thank you for motivating me to do the best I can, for listening to my complaints and for believing in me. I am grateful every day to have you in my life and think the best thing about moving to Iceland was meeting you.

I would also like to thank my parents, sister, other family members and friends. While it might have seemed a bit far to move to Iceland, you have been nothing but supportive. Despite the physical ocean between us, the bond between us has only grown stronger. I suspect the distance between Halifax and Victoria will do the same.

1. Introduction

Beautiful landscape features, volcanoes create puzzling questions for scientists in unique parts of the world. Volcanic eruptions do not always follow a set of obvious guidelines when occurring and can be unpredictable natural hazards. They can pose large threats to vast populations of the world that live on their flanks [1], [2], can cause widespread short-term climatic changes from gas emissions [3] [4], can create ash plumes that interfere with aircraft engines [5] [6] and can spread large amount of ash over local and distant regions, causing crop failure and health hazards for people and livestock [7].

Advancements in volcanic eruption detection and monitoring are occurring [8] [9]. However, with more information about the subsurface processes that occur immediately before an eruption, characterization of volcanoes and their style of eruptions could be improved [10] [11]. The vesiculation, degassing and fragmentation that occurs to magmas during their rise in the conduit, affects the explosivity, gas emissions and types of products that occur during an eruption ([12], [13]). Understanding their relationships can prove helpful in predicting the style and magnitude of future eruptions of a studied volcano or volcanoes of similar characteristics, and could lead to better methods of monitoring and detecting volcanic eruptions.

This thesis focuses on the vesiculation and fragmentation of magma from the 2011 Grímsvötn eruption, which was the most intense and largest in Iceland in 50 years [14]. This volcano is particularly interesting because it is located under Europe's largest glacier and is Iceland's most active central volcano, Grímsvötn [15]. The Grímsvötn Volcanic System has produced one of the most devastating eruptions in Iceland since its settlement in 870 AD, the 1783-4 AD Laki eruption [7]. Perhaps an even larger hazard is its subglacial caldera lake from which Grímsvötn has powerful and often eruption-driven jökulhlaups [16] [17]. For hazard mitigation and prediction it is important to understand the inner workings of the Grímsvötn Volcanic System, the plumbing system beneath the central volcano, as well as under the fissure swarm. Grímsvötn's eruptive products give us insight into the complex magmatic plumbing that feeds the central volcano as well as the fissure swarm of the system. What happens in the shallow conduit of the plumbing system governs what type of eruption will occur. This research attempts to characterize the vesicularity, degassing and fragmentation patterns of pumice lapilli clasts with the aim to understand how and why this eruption was so explosive. Hence, the objectives of this thesis are to answer

the following questions about the 2011 event:

- What are the density and vesicularity of the pumice lapilli clasts from this eruption and how do they change over the course of the eruption?
- What is the vesicle size distribution of the pumice lapilli clasts and how does it change over the course of the eruption?
- What can these values tell us about the eruption style, especially fragmentation and degassing of magma that occurred during this eruption?

Chapter 2 begins with presenting background information on the geology of Iceland. Chapter 3 covers the information about the Grímsvötn Volcanic System and about the 2011 eruption of Grímsvötn specifically. Chapter 4 looks at magma fragmentation processes. The methodology chapter, Chapter 5, delves into the research that underpins the key elements of the thesis with the intention of providing a good summary. Chapter 6 first enumerates the results of the density and vesicularity measurements and calculations and the details about the number density of vesicles, the vesicle volume distribution and the vesicle size distribution. Chapter 7 provides a discussion of the results of the thesis, including the vesicularity changes and the vesicle size distributions and explores the implications for magmatic processes such as degassing, fragmentation, magma-water interaction and explosivity. Finally, Chapter 8 contains concluding remarks.

2. Geology of Iceland

2.1. Origin of Iceland

Iceland is located on a plateau on the northern Mid-Atlantic Ridge (MAR), a divergent plate boundary. The interaction between this spreading center and a mantle plume that is thought to have begun 24 million years ago, is what gives Iceland approximately $300,000 \text{ km}^2$ in area including the shelf, of which $103,000 \text{ km}^2$ is above sea-level (a.s.l.) [18]. Some of the more prominent features of Iceland include volcanoes, geothermal areas, glaciers, earthquakes, and deserts. When these features are found in conjunction with one another they can create some impressive phenomena, such as within-glacier volcanism, which is the focus of this paper [19].

The hotspot of Iceland is thought to be fed by a deep mantle plume and the superimposed mid-ocean ridge system. The centre of the mantle plume is currently located in Central Iceland, between Hofsjökull and Vatnajökull at $64^\circ 40' \text{N}$ and $18^\circ 10' \text{W}$ [18] [20]. The partial melting of the mantle derived material, within the plume, is the source of the magmatism and volcanism in Iceland. The plume started during the opening of the North Atlantic Ocean 56-61 Ma [18]. Bjarnason [18] believes that the source lies at least 450 km deep in the upper mantle, as shown by a seismic low-velocity anomaly, however the true depth of the source is still debated. It is usually agreed that hotspots are sourced from the mantle, but the nature of the conduit system and depth of the mantle plume are generally not well known [22] [23] [24]. This hotspot has helped to create the Icelandic plateau with an anomalously thick crust. Average oceanic crust is 7.1 km and between 5.0-8.5 km thick at the extremes [25] whereas Icelandic crust ranges from the thickest crust at the centre of the mantle plume of 40 km thick, 35 km thick in East Iceland with thin crust away from the mantle plume and less than 20 km thick in the Northern Volcanic Zone [26]. As seen in Figure 2.1, the anomalous volcanism also stretches in the form of the Greenland-Iceland-Ridge and the Faroe-Iceland-Ridge, which may be trails of the hotspot. It is still uncertain if the Icelandic hotspot is a fixed point and its expression could be used to trace its path with respect to time [18] [27].

Glaciers currently cover about 11% of Iceland's surface, primarily by five large ice caps and over twelve smaller glaciers on high peaks [28]. The largest ice cap, Vatna-

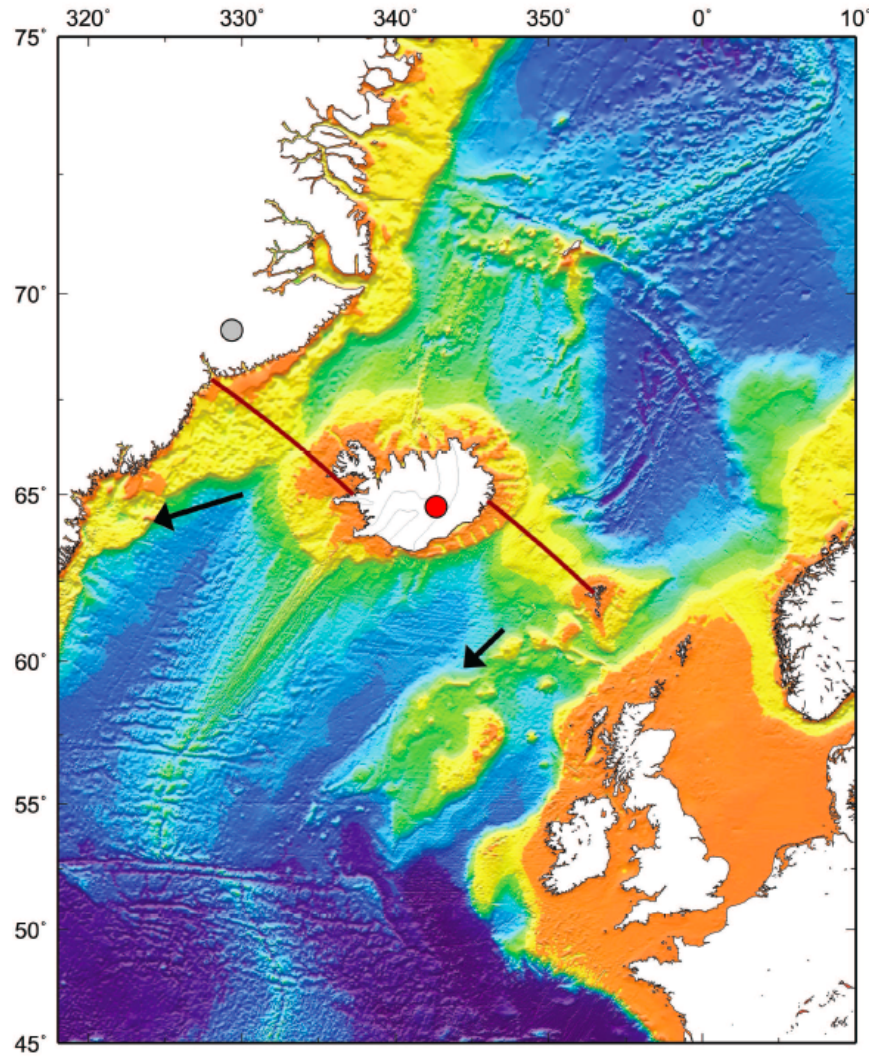


Figure 2.1: A bathymetry map of the North Atlantic, showing the extent of the Icelandic plateau. Grey dot is the location of the hotspot at 40 Ma [20]. Red dot shows the supposed current location of the hotspot. Red lines indicate the Greenland-Iceland-Ridge (west) and Faroe-Iceland Ridge (east), possible hotspot tracks. The arrow represent absolute plate motions; North American: 26 mm/yr, Eurasian: 15 mm/yr [21]. From Bjarnason (2008) [18].

jökull, covers 8,100 km^2 and has six mountain ranges beneath it, including Grímsfjall and Bárðarbunga, with Grímsfjall having the central volcano Grímsvötn that will be the focus of this study [28].

2.2. Volcanic zones and their products

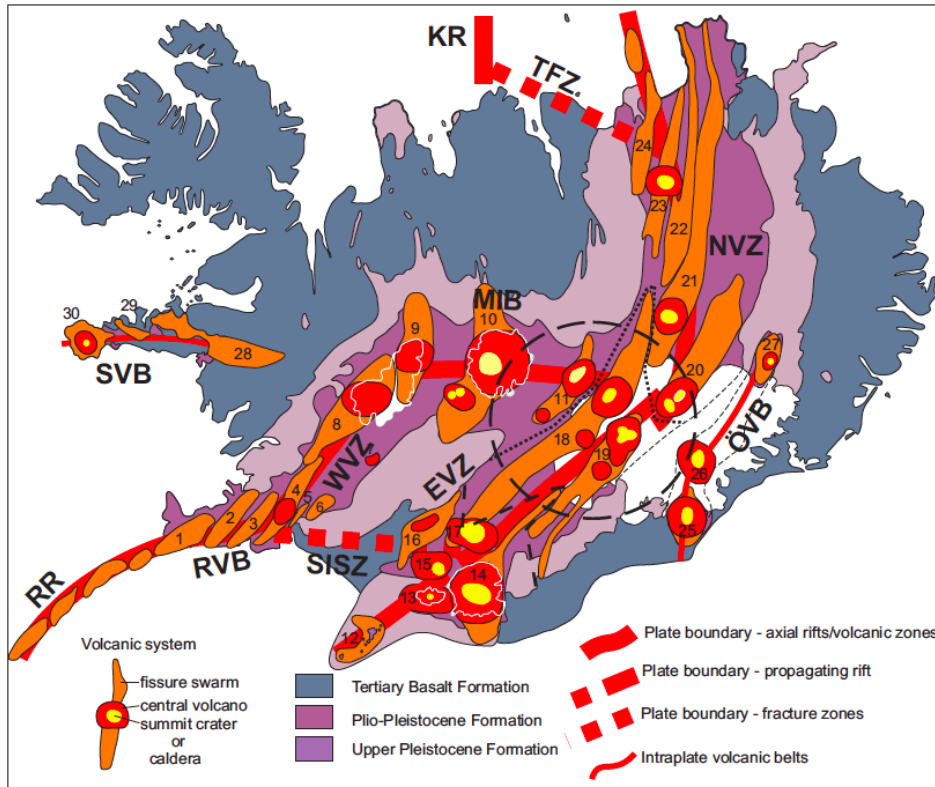


Figure 2.2: Geological map of Iceland and the 30 volcanic systems of Iceland. Major geological formation divisions are shown. Main faulting and volcanic zones are labelled: RR, Reykjanes Ridge; RVB, Reykjanes Volcanic Belt; SISZ, South Iceland Seismic Zone; WVZ, West Volcanic Zone; MIB, Mid-Iceland Belt; EVZ, East Volcanic Zone; NVZ, North Volcanic Zone; TFZ, Tjörnes Fracture Zone; KR, Kolbeinsey Ridge; ÖVB, Öræfi Volcanic Belt; SVB, Snæfellsnes Volcanic Belt. From Thordarson and Höskuldsson (2008) [29].

The main volcanic zones of Iceland are depicted in Figure 2.2. The rift and mantle plume interact, creating belts of faulting and volcanic activity. The main axial rift zone, where most of the spreading and plate growth occurs, contains the Western Volcanic Zone (WVZ) and the Northern Volcanic Zone (NVZ), which are connected by the Mid-Iceland Belt (MIB) and are characterized by tholeiitic magmatism. The Reykjanes Volcanic Belt (RVB) in the South and the Tjörnes Fracture Zone (TFZ) in the North also join the main part of the axial rift zone to the complete Mid-Atlantic Ridge (MAR) system. The Eastern Volcanic Zone (EVZ) is a propagation zone that is extending to the southwest through the crust that already exists. It will become an axial rift ultimately, switching from the WVZ and is the most active area of Iceland currently. The EVZ has tholeiitic magmatism in the northern portion and

somewhat alkalic in the southwest [29] [30]. Intra-plate belts also exist in Iceland; the Öraefi Volcanic Belt (ÖVB) to the east and the Snæfellsnes Volcanic Belt (SVB) to the west. The (ÖVB) has been thought to be a very early stage rift [31] and the SVB an old rift that is reactivated and now propagating to the east-southeast [30]. Grímsvötn is at the north-eastern part of the EVZ, in the region that is primarily tholeiitic basalt and is the most active region.

Within the volcanic zones are 30 volcanic systems: twelve have a fissure swarm (elongated area of activity) and a central volcano (concentrated area of activity). The others may have a central domain instead of a central volcano (Figure 2.2 and Table 2.1). Grímsvötn system (Figure 2.2, number 19) located in the EVZ, has an embryonic fissure swarm and a central volcano. All of the volcanic systems in Iceland have had eruptions in the Holocene except Esjufjöll and Snæfell [29].

The igneous rocks that are primarily present in Iceland can be divided into three series; alkalic, transitional alkalic and tholeiitic [32]. The mid-ocean ridge basalts, MORB, are most closely related to the tholeiitic basalts. Generally, the mildly alkalic basalts are found in the SVB, ÖVB and the southern EVZ. The tholeiitic basalts are found in the axial rift represented by the RR, RVB, WVZ, MIB, northern part of the EVZ, NVZ, TFZ and KR. In the last 1100 years, the volume of erupted magma was 82% from the EVZ, 13% from the RVZ-WVZ, 2.5% from the NVZ and 2.5% from the intraplate volcanic belts (ÖVB and SVB) [30].

The basaltic volcano eruptions in Iceland can have a number of settings, such as subaerial, subaqueous, emergent subaqueous, subglacial and within-glacier environments. The types of eruptions can be "dry" magmatic effusive and explosive, which are typical of subaerial environments, wet effusive, typically confined to subaqueous settings (i.e. pillow lava) and "wet" explosive (i.e. phreatomagmatic), which typify subaqueous emergent and within-glacier settings, but also in subaerial environments when the rising magma comes in contact with external water. The explosive type is the focus of this research. It can involve the fragmentation of magma in the conduit or vent when it is rising, producing pyroclastics, gases such as H_2O , CO_2 and SO_2 and lithic fragments [33] [12] or explosive interaction between magma and external water in a fuel-coolant type interaction [34] [35] [36].

Subaerial magmatic eruptions in Iceland tend to be of the flood lava type; more effusive and less explosive, producing lava shields like Skjaldbreidur at a central vent and mixed cone rows if along a long fissure. Effusive magmatic eruptions can also create spatter rings or cones. Subaerial phreatomagmatic eruptions are more vigorous and produce tuff cones like the Hverfjall tuff cone at Mývatn and if on long fissures, rows of tuff cones. It is the interaction with water that creates the necessary conditions for ash production that is typical of tuff.

Subglacial and submarine eruptions can be of several types. Effusive subglacial

Table 2.1: 30 volcanic systems of Iceland. Numbers are according to map of Figure 2.2. Fissure swarm scale: xxx = mature, xx = moderate maturity, x = early stages. Central volcano: cv = central volcano, d = central domain. Modified from Thordarson and Larsen (2007) [30] and Thordarson and Höskuldsson (2008) [29].

	Volcanic zone	Name	Fissure swarm	Central volcano
1	RVZ	Reykjanes/Svartsengi	xxx	d
2	RVZ	Krýsuvík	xxx	d
3	RVZ	Brennisteinsfjöll	xxx	d
4	WVZ	Hengill	xxx	cv
5	WVZ	Hrómundartindur		d
6	WVZ	Grímsnes	xx	d
7	WVZ	Geysir		d
8	WVZ	Prestahnjúkur	xxx	cv
9	WVZ	Hveravellir	xx	cv
10	MIB	Hofsjökull	xxx	cv
11	MIB	Tungnafellsjökull	xx	cv
12	EVZ	Vestmannæyjar	xx	d
13	EVZ	Eyjafjallajökull		cv
14	EVZ	Katla	x	cv
15	EVZ	Tindfjöll		cv
16	EVZ	Hekla-Vatnafjöll	xx	cv
17	EVZ	Torfajökull		cv
18	EVZ	Bárðarbunga-Veidivötn	xxx	cv
19	EVZ	Grímsvötn	x	cv
20	NVZ	Kverkfjöll	xxx	cv
21	NVZ	Askja	xxx	cv
22	NVZ	Fremrinámur	xxx	d
23	NVZ	Krafla	xxx	cv
24	NVZ	Theistareykir	xxx	d
25	ÖVB	Öræfajökull		cv
26	ÖVB	Esjufjökull		cv
27	ÖVB	Snæfell		cv
28	SVB	Ljósufjöll	x	d
29	SVB	Helgrindur (Lýsuskard)	x	d
30	SVB	Snæfellsjökull		cv

eruptions can create pillow lava cones or ridges when the lava is erupted under wet conditions. Within-glacier eruptions with effusive and explosive phases can form móberg structures, which are broad mounds of consolidated hyaloclastite or essentially a tuff breccia that was formed under water or ice and is rich in glass. Eruptions that have an effusive-explosive-effusive pattern will create tuyas or table mountains [30]. These landforms are steep-side and flat on the top because they erupt under ice or water and are layers of breccia and hyaloclastite on top of pillow lava [19]. Subglacial central volcanoes will have a wider variety of volcanoclastic deposits, including magmatic and phreatomagmatic fall and surge deposits, volcanoclastic gravity current deposits, tillites, as well as subaerial and pillow lavas. An example is Grímsvötn. Other volcanoes, such as Snaefellsjökull, are more of the stratovolcano type and are typified by a sequence of alternating lava and pyroclastic fall and flow deposits. There are also multivert systems, like Katla and Torfajökull and monogenetic single cones or cone rows, like Eldfell. Other forms are monogenetic volcanic events that formed in submarine or subglacial environments, such as the Surtsey activity in the mid-1960s and the Gjálp eruption under Vatnajökull glacier [30].

The wide variety of volcanic forms means that Iceland has had almost all types of eruption styles. In historical times, there have been eruptions of Hawaiian style including flood lavas like Eldgjá in 934-940 [4] or Laki 1783-1784 [7], Strombolian like Heimaey in 1973 [37] and Plinian and Phreatoplinian like Askja in 1875 [38] [39] and Surtseyan, the variety that is typified by the shallow water explosive eruption of Surtsey in 1963 [40].

3. Grímsvötn

3.1. Grímsvötn Volcanic System

The Grímsvötn Volcanic System is a part of the Eastern Volcanic Zone and is located in both the rift-zone and the central mantle plume area of the Icelandic plume. It also lies both under Vatnajökull and extends to the southwest of the glacier. As shown in Figure 3.1b, it has two central volcanoes and a fissure system; the principal Grímsvötn central volcano, Thórdarhyrna (Þórðarhyrna) central volcano and the NE-SW fissure system [41]. The central volcanoes have eruptions under the glacier, while the fissure system is partially subglacial and partially subaerial. Grímsvötn central volcano is basaltic and is considered the most active in Iceland with 1-2 eruptions per decade on average [15] [42]. In the last century, eruptions have occurred nearly every 5-10 years except during the period between 1954 - 1983, which was a relatively quiet period for the Grímsvötn volcano[43]. It is located underneath Vatnajökull on the west-central side (Figure 3.1a) and reaches an elevation of 1725 meters a.s.l. [15].

Eruptions of the fissure swarm can be subaerial or subglacial and effusive or explosive. They can also be a mixture of effusive or explosive, with both magmatic and phreatomagmatic phases. The Gjálp subglacial eruptions in 1938 and 1996 [44] took place between Grímsvötn and Barðarbunga, on a 6 km long fissure under 550-750 m of ice. The eruption in 1996 was explosive and broke through the ice in 31 hours and caused a significant jokulhlaup [44]. The Laki flood lava eruption of 1783-1784 was located on the fissure swarm southwest of the glacier. It was a mixed event with 10 distinct explosive phases followed by longer-lasting phases of predominately effusive activity [7]. It erupted 15 km^3 of basaltic lava from a fissure of 27 km in length and lasted eight months. The explosive episodes of this eruption had a large impact on the population of Iceland. This eruption expelled sulphur dioxide and fluoride gas that devastated the population [7] [30]. It caused large amount of livestock and crops to die and led to a widespread famine in Iceland, killing nearly one quarter of the Icelandic population. The sulphuric plumes from this eruption also caused temperatures to drop in many places in the Northern Hemisphere. Examples of impacts include causing drought in India and crop failure in parts of Europe, leading to many more deaths. This eruption is one of the earliest examples that scientists

use to conclude that volcanic eruptions can alter climate [7].

Within the Grímsvötn system is a composite caldera of 50 km^2 . It is comprised of three nested calderas; one at the north, the east and the south, which is the main caldera [45]. All eruptions at the Grímsvötn central volcano are subglacial and are commonly phreatomagmatic [15] [30] [43]. The main complex has a 30 km^2 subglacial caldera lake where meltwater accumulates and is the location of the powerful geothermal area of Grímsvötn (Figure 3.1c) [46]. The glacial surface above the geothermal area is depressed and ice flows into the depression from all other directions [15].

Most of the eruptions of Grímsvötn are in the caldera, specifically along a fault on the southern caldera, that lies below the glacier of 50-200 m thick ice. Most eruptions here are explosive and break through the ice quickly, like the 1998 eruption. The 2004 eruption took 30 minutes. Once the activity melts through the ice, the eruption becomes subaerial and phreatomagmatic from the interactions with meltwater. Eruptions of Grímsvötn are usually small to moderate sized, between 0.01 and 0.5 km^3 dense rock equivalent (DRE) tephra erupts and they last several days to weeks, although the tephra does not usually deposit beyond the glacier [30] [47] [29]. The eruptions of the Grímsvötn Volcanic System, the GVS, from the last 110 years are listed in Table 3.1.

The evidence for a shallow magma chamber in the GVS is seen by gravity and magnetic surveys [45] [50]. Using the inversion of earthquakes, a low-velocity body of about 20 km^3 and up to around 3 km deep, was described by Alfaro et al. (2007) [50]. With shear-wave studies, it was said that there is a pure or high percentage partial melt area below the Grímsvötn volcano that represents the magma chamber. It is a maximum 7-8 km in the E-W direction and 4-5 km in the N-S direction, perhaps in the fashion of a sill-like magma chamber of less than 1 km thickness. This second area of partial melt seems to be at depths of 3-4 km [50]. Gudmundsson and Milson (1997) [45] propose that a magma chamber at Grímsvötn is probably located at the level of neutral buoyancy beneath the caldera, at approximately 1.5 km depth in the crust.

Grímsvötn has an interesting history of jökulhlaups, both as a productive geothermal area and an active volcano. The subglacial lake at Grímsvötn is the largest one in Iceland and releases its flood the outwash plain, Skeiðarársandur [51] [28]. Current data shows that the lake level rises by 10-15 m per year. When the water level has undergone a 80 to 100 m of rise, the jökulhlaup usually occurs. Jökulhlaups have occurred every 1-10 years and can last from two days to four weeks (Björnsson, 1988, 2003). The question still remains if a jökulhlaup is caused by eruptions or if a jökulhlaup can trigger an eruption. For example, a fissure eruption in Grímsvötn, namely the Gjalp eruption of 1996 (4.0 km^3 of ice melted), produced a large jökulhlaup due to the eruption remaining subglacial for a long period of time, allowing

Table 3.1: The eruption history of Grímsvötn Volcanic System over the last 110 years. Modified from Jude-Eton (2013) [47]. Additional information from Gudmundsson and Bjornsson (1991) [48] and Caseldine et al. (2005).

1902	Grímsvötn and Thórdarhyrna.
1910	Possibly Grímsvötn, western Vatnajökull location [49] .
1919	Volcano uncertain.
1922	Eruption certain. Thought to be Grímsvötn caldera [48].
1933	North of Grímsvötn caldera.
1934	Near south caldera wall.
1934	Volcano Uncertain: Vatnajökull.
1938	8 km N of Svartibunki.
1954	Opening in glacier, although likely a steam explosion, not eruption [48].
1983	Southern Grímsvötn caldera wall.
1996	Subglacial Gjálp fissure eruption.
1998	S caldera wall.
2004	SW caldera.
2011	SW caldera, same vent as in 2004.

quick melting of ice and accumulation of water in the lake. However, the eruptions in the Grímsvötn caldera lake tend to break through the overlying ice in 10-20 minutes, resulting in much less ice melting (on the order of about 0.1 km^3) [44] [17] [51]. These eruptions cause water to accumulate and increased pressure but do not change the mass, as the ice that was above the lake melts and accumulates as water and does not usually trigger a jökulhlaup. A jökulhlaup may however trigger an eruption from the pressure release that occurs from the lake emptying. This pressure release may also cause explosions from boiling in the subglacial hydrothermal area [51].

Grímsvötn seismic and deformation signals are important indicators of pending eruptions. Grímsvötn has a shallow magma chamber and may show signs of recharging from inflation signals with GPS measurements. The continuous GPS measurements have been conducted at Grímsfjall since just before the 2004 eruption and showed vertical displacement from glacial isostatic adjustment and magma accumulation in the shallow magma chamber. The GPS also showed horizontal movement from magma pressure changes, moving outward from the caldera during inflation periods between eruptions and inward during the eruptions themselves [52] [53]. Figure 3.2 shows the vertical displacement of the GPS station at the caldera rim, GPS station GRIM and continuous GPS station GFUM (17.26660°W and 64.40676°N). Uplift occurs before the 1998 eruption and subsidence again after the eruption, indicating a drop in pressure. Pressure increase began again after the 1998 eruption, surpassing the level of displacement of the previous eruption by 2003, until it finally erupted in 2004. Using a Mogi model to indicate the source at a depth of $<1.6 \text{ km}$, Sturkell et al. (2003) determined that in order to reach the critical pressure for a new eruption to take place at Grímsvötn, at least 0.15-0.20 m of vertical uplift from the 1998 level would be required. This level was exceeded in September 2004, or almost two months before the eruption in 1 November 2004 [54].

Prior to the 2004 and 2011 eruptions of Grímsvötn, earthquake activity showed similar patterns, of a slow increase in the number of earthquakes in the years before the eruptions and almost no events afterwards. Figure 3.3 shows the increase in earthquake activity in the years and months leading up to the eruption the 1st of November 2004 and the dramatic increase in the days prior to the eruption. The data also shows a period of nearly no seismic activity following the eruption [55]. A continuous seismic station at Grímsvötn was active from 2002 onward and data prior to 2002 was collected intermittently. The 1998 eruption can be seen in the increase in activity as well. The GPS data and the earthquake patterns have allowed for some predictions before the past eruptions, specifically pointing towards eruptions occurring at the southwestern flanks of the Grímsvötn volcano when the magma accumulates at shallow depths and the pressure exceeds a threshold of the strength of the crust [53].

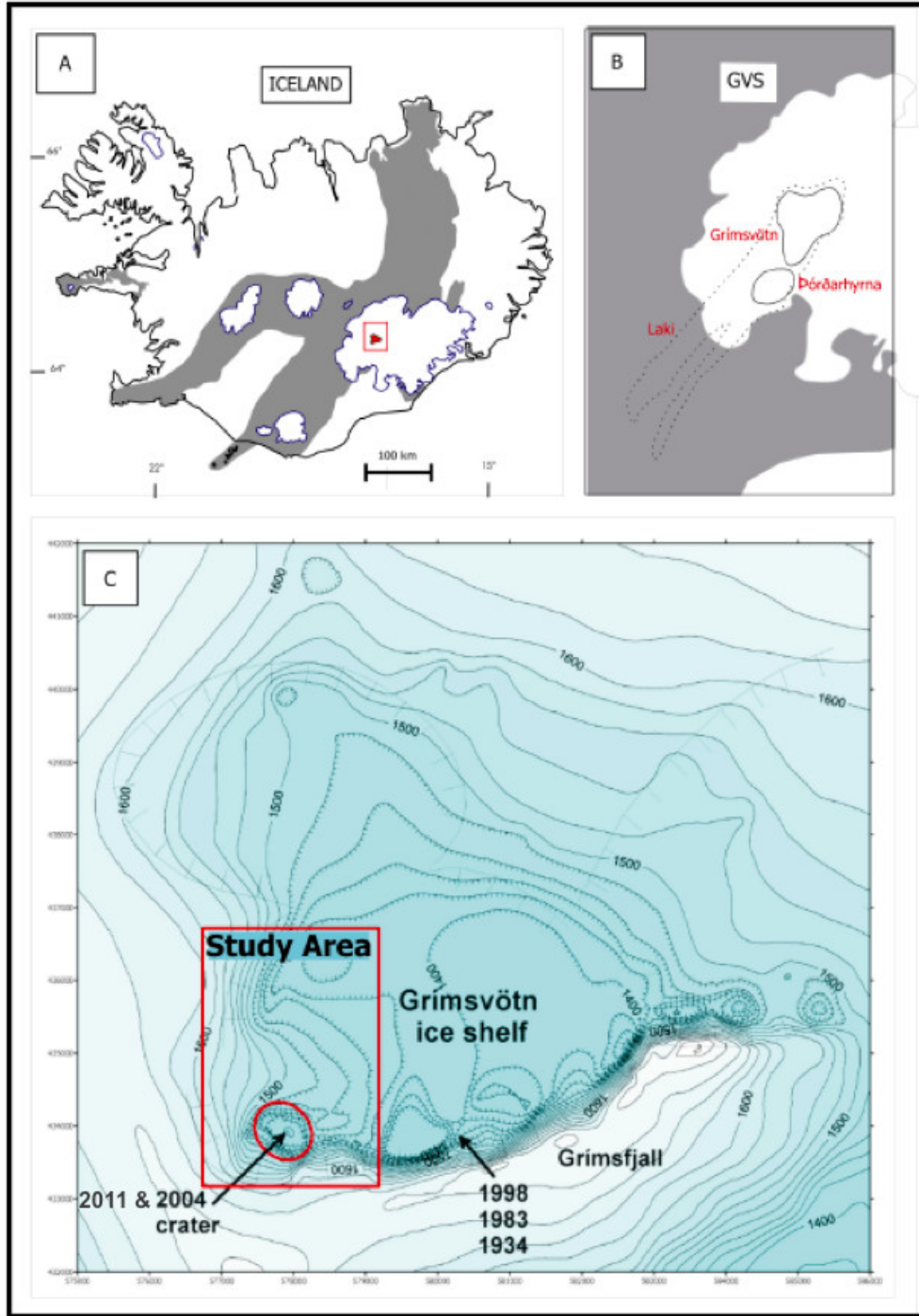


Figure 3.1: Maps of the study area. A) Map of Iceland with Grímsvötn central volcano in red. Grey shaded areas are locations of volcanic zones of Iceland. B) Central volcanoes of Grímsvötn in black outline. Dotted line is fissure area. Modified after Thordarson and Self, 1993 [7] C) Locations of past and current eruptions of Grímsvötn. Contours show the glacier's surface. Modified from Jude-Eton et al. (2010) [15].

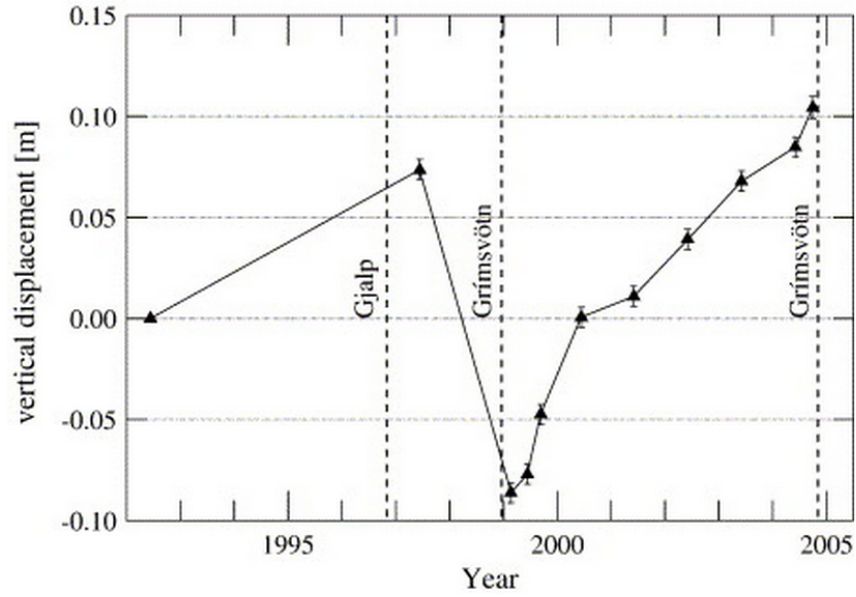


Figure 3.2: Vertical displacement of a GPS station at the caldera rim of Grímsvötn. Reference point is at Jökulheimar [52].

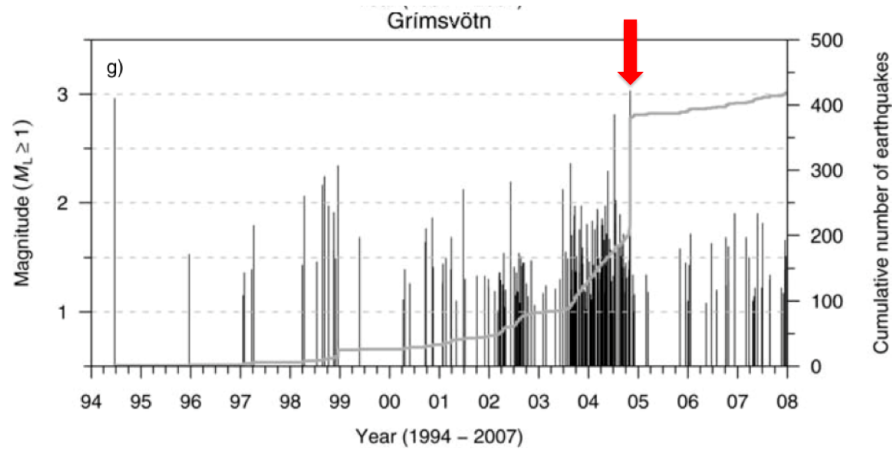


Figure 3.3: Earthquake activity increased in the years and months before the 2004 eruption at the Grímsvötn caldera and dramatically in the days before the eruption. The onset of the 2004 eruption is indicated with a red arrow. From Jakobsdóttir (2008) [55].

3.2. The 2011 Grímsvötn eruption

From 2004, leading up to the eruption in 2011, a GPS continuous station at the Grímsvötn caldera rim (GFUM) showed semi-steady inflation on the scale of a few centimetres per year (Figure 3.5a). This is the same pattern as seen leading up to the 2004 eruption. The GPS station was moving South-East and upward. This movement was taken to indicate pressure build-up and magma accumulating in a storage zone at shallow depth beneath Grímsvötn volcano. Increased seismic activity and geothermal output had been observed in the months leading up to the eruption [8] [53].

Minutes prior to the 2011 eruption, a noticeable decrease in depth of loci of seismic activity was observed and the activity migrated from a depth of 2 to 4 km to a depth of < 1 km [8]. The maximum amount of earthquakes occurred in the hours before the eruption, including 40 earthquakes of up to magnitude 3.1 (Figure 3.4). The low frequency seismic tremor also increased 30 minutes before the eruption indicating magma moving towards the surface [8].

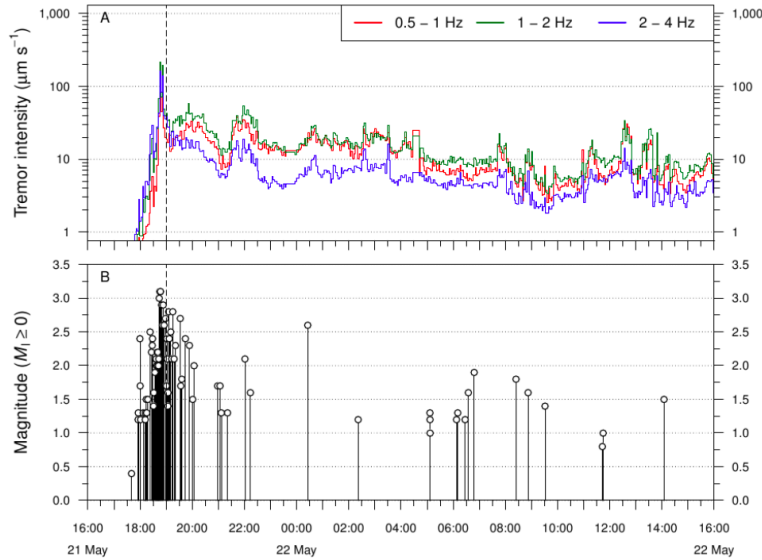
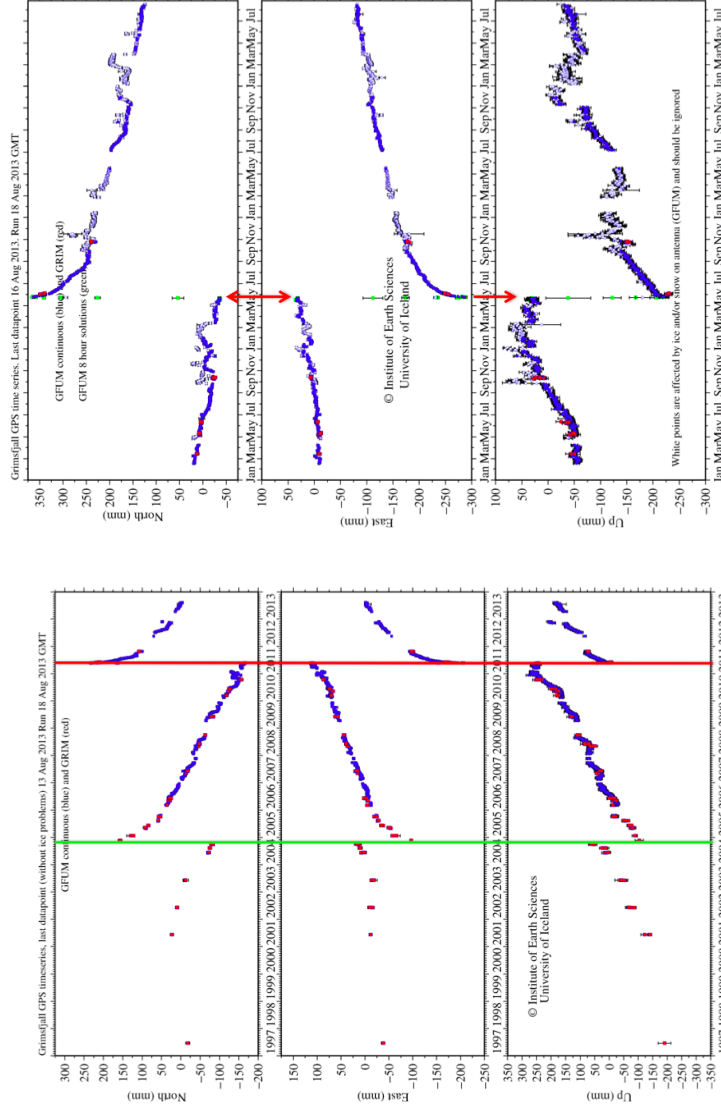


Figure 3.4: Seismic tremor and earthquakes at the seismic station on Mt. Grímsfjall during the 2011 Grímsvötn eruption. From Hreinsdottir et al. (2014) [8].



(a) GPS measurements at Grímsfjall since 1997. Green line, onset of 2004 eruption; Red line, onset of 2011 eruption. (b) GPS measurements from at Grímsfjall since January 2010. Red arrows, onset of 2011 eruption.

Figure 3.5: GPS measurements from GFUM and GRIM stations at the Grímsvötn caldera rim from IMO and Hreinsdóttir at the Institute of Earth Sciences, University of Iceland [56].

In the very first hours of the eruption, the continuous GPS station on Mt. Grímsfjall (approximately 5 km from the eruption) showed horizontal displacement of 20 cm to the north, 15 cm to the west and subsidence of 10 cm. In the first two days, the station had moved horizontally 50 cm to the northwest and had subsided 25 cm [14]. Overall movements of the GPS station during the eruption were approximately 40 cm north, 35 cm west and a displacement of 25 cm downward in the vertical direction (Figure 3.5b).

The eruption started under the glacier at 17:30 UTC, 21 May 2011 at the southwestern caldera rim, the same section of the south bounding caldera fault as the 2004 eruption (Figure 3.1c) [14]. The eruption was quick to melt through the 50-200 m of ice above the lake and at 19:00 UTC the eruption came through the glacier, becoming a subaerial eruption and ash was being ejected. At the peak of the eruption, the plume reached a height of 20 km [14] and extensive ash fallout was experienced in southeast Iceland (Figure 3.6).

High alert was placed on the Skeiðarársandur, the floodplain south of the glacier, as the rivers in this area can become heavily flooded due to a jökulhlaup. This did not occur. It is deduced that a jökulhlaup did not take place because such an event had occurred on 31 October 2010, from Grímsvötn and for that reason the water level was rather low in the caldera lake [14]. The jökulhlaup in October 2010 was preceded the night before by an earthquake of magnitude 3.0 at Mt. Grímsfjall [14]. Another possible reason for the jökulhlaup not taking place in conjunction with the May 2011 eruption of Grímsvötn is that the eruption took place in the same location as the 2004 eruption. Hence, little ice was left to melt at the vent [51] [15].

The 2011 eruption produced ash and basaltic pumice and it was unusual in that it showed that a basaltic volcano can sustain a sizeable explosive eruption [57]. The proximal deposit is the focus of this study and was alternating medium to coarse pumice lapilli and fine, ash-grade units (Figures 6.2 and 6.3). The high plume dispersed radially at the beginning of the eruption, then to the south and finally to the NW. The plume contained very little tephra, primarily fine ash. The main tephra dispersal was from a section of the plume that collapsed below 10 km and was carried by strong northerly winds to the SSW. The tephra from the plume was deposited across most of the country, however it was focused south of the vent (Figure 3.6). At a distance of 7 km from the vent, thickness of the tephra deposit was 170 cm, while at 35 km from the vent nearly 10 cm was deposited [8]. The estimated total erupted volume of dense-rock equivalent (DRE) is around $0.27 \pm 0.07 \text{ km}^3$ [8] [58].

Sulphur that degasses from hotspot volcanoes such as Grímsvötn, can add a significant mass to the atmosphere [59]. The sulphur that was released from the eruption of Grímsvötn in 2011 was measured and was an order of magnitude greater than in 2004. The plume was mapped using ultraviolet measurements from the Ozone

Table 3.2: Timeline of 2011 Grímsvötn eruption (times in UTC). All information from the updates of the Icelandic Meteorological Office [14].

21/05 17:30●	Spike in tremor activity detected and earthquake activity began, with the largest magnitude 3.0.
21/05 19:00●	Ash detected as eruption broke through surface of the glacier. Earthquakes diminished at this time and seismic tremor reached a high, then decreased after 22:00.
21/05 21:00●	Ash plume rose to 20 km.
22/05 12:00●	Height of ash plume decreased to 10 km. Concentration of fallout of tephra was to the south and lightening strikes were frequent (60-70 per hour). The last earthquakes detected were in the afternoon, 22/05.
23/05 17:00●	In one hour, beginning at 17:00, 300 lightening strikes were recorded.
24/05 21:00●	Ash plume was at a height of 5 km although the activity was in pulses. Activity was in 4 tephra cones and was surrounded by meltwater.
25/05 02:10●	Ash plume was at 12 km, then subsided.
25/05 02:20●	No ash plume detected.
25/05 03:30●	Steam plume of 5 km detected.
25/05 15:00●	No further ash plume anticipated (IMO).
26/05 16:00●	Only ash at eruption site (IMO, HI) reported.
28/05 07:00●	Eruption ended.

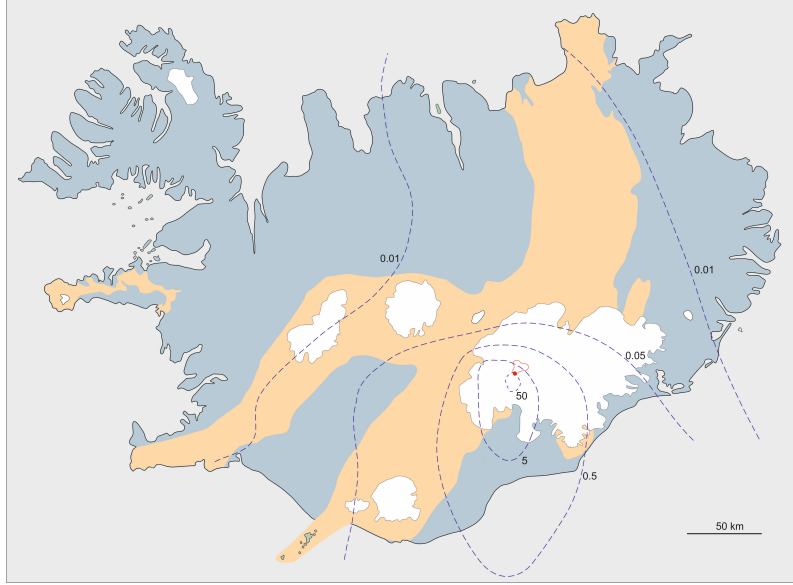


Figure 3.6: A draft isopach map of the tephra from the G2011 event showing outline of selected isopachs. Modified in 2015 from unpublished map by Magnús T. Guðmundsson, Ármann Höskuldsson and the G2011 eruption team.

Monitoring Instrument of NASA's satellite Aura [58]. The maximum peak of SO_2 was around 0.3 Tg on 23 May and the SO_2 cloud dispersed and decayed after this date, completely disappearing by early June. While the ash cloud had moved south on the 23 May and then east on the 24 May from the eruption site, the SO_2 moved northwest in the stratosphere. Figure 3.7 shows the map of the cloud dispersals on 23 May, two days after the eruption began.

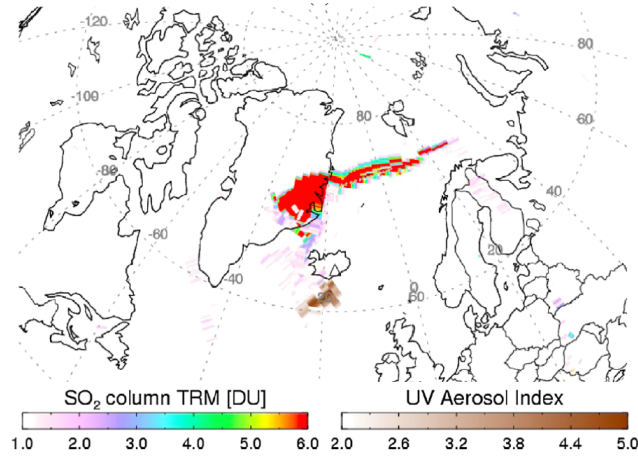


Figure 3.7: Map of SO_2 cloud (reds and blues) and ash cloud (brown) on 23 May, from the 2011 Grímsvötn eruption.

The Grímsvötn eruption products were tholeiitic basalt that had a silica content of

around 50% SiO_2 , which is typical of previous Grímsvötn products [14] [15] [58]. The groundmass is composed of glass with variable microlite content; some are free of microlites and some are heavily crystallized groundmass [58]. To compare the ash, the 2011 Grímsvötn ash was coarser and had a lower silica content of 50% than the Eyjafjallajökull 2010 ash, which was finer and had a silica content of 63% [14]. G2011 tephra displayed MgO and TiO_2 values of similar values to historic eruption of Grímsvötn, of 4.5-5.75 wt% MgO and 2.6-3.4 wt% TiO_2 . Some tephra of G2011 tends to be slightly more enriched in TiO_2 than historic Grímsvötn eruption products and has similar MgO values. G2011 tephra has FeO values of between 12.5-14.5 wt%, with some values below historic Grímsvötn tephra, which tends to be above 13.0 wt% (supplementary data from [58]).

4. Magmatic volatiles and fragmentation

Basaltic magmas, the focus of this study, are formed through partial melting in the upper mantle. They contain volatiles including H_2O , CO_2 , sulphur, chlorine, and fluorine species [59]. Magmas can also have multicomponent vapor phases with H_2O , CO_2 , H_2S , SO_2 , Cl_2 , F_2 and noble gases. H_2O is the most abundant magmatic volatile and is a function of magma composition. The solubility of a volatile species is strongly pressure dependent but does not vary much according to magma composition (Figure 4.1). Because of its higher abundance, approximately 0.1-0.4 wt% for a normal MORB or up to 1.5 wt% in an enriched MORB, H_2O plays the largest role of the volatiles on magma physical properties, crystallization and eruptive style and will be the focus of this chapter [59].

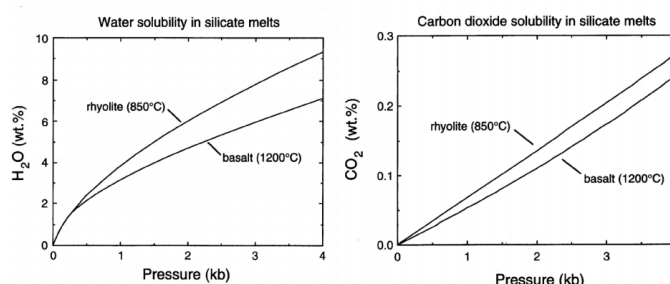


Figure 4.1: The solubility of H_2O and CO_2 [60]

Oceanic tholeiitic basalts (which are a similar composition to Grímsvötn tholeiitic basalts) usually have 1-2% volatiles, whereas alkalic basalts can be richer in volatiles, up to 7%. The difference between oceanic tholeiites and Grímsvötn tholeiites may be their volatiles content however, as Grímsvötn's 2011 eruption was explosive, whereas oceanic basalts tend to be more effusive [61]. Wolff and Sumner [61] state that shallow storage of magma, such as in the case of the Grímsvötn magma reservoir, can be expected to have little CO_2 in the exsolving volatiles. Most eruptions from shallow magma chambers have more H_2O , because nonequilibrium degassing from rapid exsolution at low pressures can increase the H_2O concentration instead of CO_2 .

While in the magma chamber, gases are dissolved in the magma because the pres-

sure is high. When the magma begins rising in the volcanic conduit, the pressure decreases and the physical properties of the magma changes. As it rises to the surface, the pressure decreases to a point where nucleation begins and gas bubbles form from the volatiles leaving the solution. However, not all volatiles exsolve or act in the same way. CO_2 exsolves from magma much earlier than H_2O and SO_2 , which in turn exsolve before Cl and F volatiles. Many MORB magmas are already supersaturated in CO_2 and they have a solubility which is nearly 30 times lower than H_2O (Figure 4.1), which is why CO_2 degasses first [59]. This mean that CO_2 may exsolve at greater depths and pressures than H_2O and a significant amount of volatile bubbles may be lost before an eruption occurs [33].

Magmas can be undersaturated or saturated with respect to H_2O in the storage zone. This has important implications as volatiles will begin to degas from magma when they are saturated. If the magma is saturated in the storage zone, the volatiles will begin to nucleate, or grow bubbles, as the magma is leaving the storage zone. If it is undersaturated, the magma needs to rise and become supersaturated in H_2O before bubbles can nucleate. Supersaturation will depend on the energy that is required and the surface tension that makes a fluid attracted to another molecule between the interface of two fluids. If H_2O cannot get to the bubble, the bubble will grow slower upon decompression. The pressure decreases as the magma ascends, allowing the concentration of dissolved volatiles to increase above the equilibrium solubility and vesicles to nucleate. Supersaturation can happen when magma ascends quickly, allowing insufficient time for volatiles to diffuse into bubbles that already exist. Bubble growth may occur instead of nucleation if volatiles exsolve and the vapor expands. Bubble growth will be limited by the rate of flow of the melt (volume growth that can be accommodated), diffusion rate of volatiles and the rate at which they exsolve, and the change in the solubility from decompression. [62]. These process are depicted in Figure 4.2.

H_2O degassing will raise the freezing point (liquidus temperature) of the magma. If the H_2O is taken out very rapidly from the solution, the physical properties of the magma will change rapidly as well. This means that microlites will usually begin to crystallize and therefore you have expanding bubbles and a stiffening magma changing the viscosity of the magma at the same time. Crystals will support heterogeneous nucleation because of the lower energy between a solid and vapor compared to melt and vapor [62].

Once bubbles have been formed in the magma, they will continue to grow and may begin to touch or coalesce. At the extreme, a foam might evolve, with polyhedral bubble shapes [63]. However, a more likely scenario is that bubbles explode from overpressure. When vesiculation reaches 75% to 83% bubbles interfere with each other and growth is constrained and models show that when vesicularity reaches 75% threshold, explosivity occurs [12] [11]. Things that may stop the vesiculation process include:

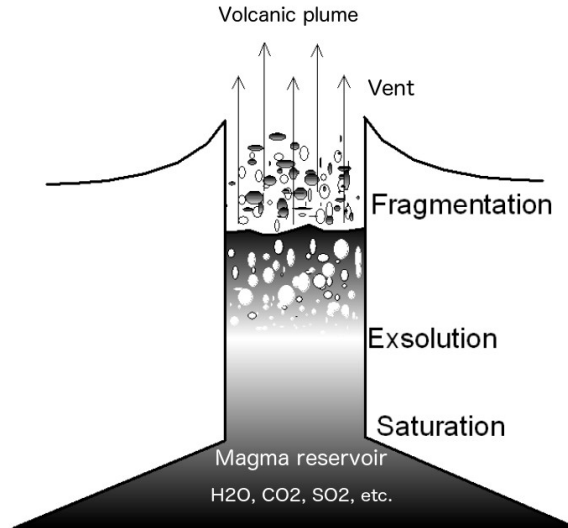


Figure 4.2: During the ascent of magma from the magma reservoir to the vent, volatiles go from saturation in the magma, to exsolution, nucleation and fragmentation of the magma upon reaching the surface. Modified from Sparks (1978) [12].

- shallow depth reservoirs with non-explosive degassing [64] or collapse of bubbles at depth [65]. This will lead to no eruption occurring or an effusive eruption.
- vesicles breaking, causing fragmentation. This will mean a dry explosive eruption occurs when the volatiles exsolve [11].
- interaction of magma with water, causing cooling and fragmentation. This will mean a wet explosive eruption occurs with steam and possibly vesiculated magma [34] [35] [36].

The volume of gas in the conduit increases from degassing to a level where the liquid magma fragments and the gases cause the fragments to explode violently. It is the volume and pressure changes, and the rate of the volume change from the volatiles exsolving from the magma, that causes the magmatic fragmentation [12] [34] [35]. The ascent and fragmentation process is depicted in Figure 4.2 and generally applies to H_2O , the primary volatile, as well as to a lesser extent, SO_2 .

There are two basic mechanisms that can drive fragmentation; the expanding (exsolving) magmatic gases and the interaction of magma with water or ice, causing phreatomagmatic fragmentation [66]. The expansion that occurs in the conduit from degassing can be the cause of eruptions. Alternatively, it can be caused by

fragmentation that happens from rapid decompression, such as when bubbles leave the already vesiculated magma [67]. On the other hand, water can play a role in fragmentation by chilling the magma. The mechanism for a phreatomagmatic eruption involves magma cooling from the interaction with water and rapid contraction of the magma, in conjunction with gas pressure changes causing fragmentation [68] [69]. The water that is added to the volcanic system during a phreatomagmatic eruption is heated quickly when it comes in contact with magma and expands. This interaction can cause what is called a molten-fuel-coolant interaction, (MFCI) [34] [35] [36].

MFCI in the case of magma and water, has the water or steam acting as the coolant in the reaction. Explosions occur from the large volume difference in thermal expansion between water and magma, so that when hot melt cools from the interaction with a cooler water, much less space is available for the expansion of the heated water. A volcanic MFCI can be broken down into four steps: (1) hydrodynamic mixing, (2) a trigger (3) fine fragmentation, and (4) vaporization and expansion [70]. The hydrodynamic mixing of water and magma causes vapour films to collapse and contact of the substances occurs, with heat transfer increasing. Fine fragmentation processes are initiated and the area of direct contact continues to increase quickly, creating positive feedback for further fine fragmentation. Eventually, from the heat flux increasing to the water, the water becomes superheated and will vaporize. This steam expands and can drive explosive phreatomagmatic activity and further fragmentation [70].

4.1. Density measurement techniques

The methods that were used for this thesis are described in detail in the Methodology chapter. The density and vesicularity measurements of the clasts followed the procedure laid out by Houghton and Wilson (1989) [11]. This technique was chosen because it is readily available with simple tools, quick for several hundreds of clasts and reliably gives reproducible results. An alternative to this method is to measure density using an He-pycnometer [71]. An He-pycnometer measures the volume of an object, porous or not, by measuring gas displacement and then calculates the density by the ratio of mass to volume.

There are many techniques for determining vesicle texture but the image analysis technique of Shea et al. (2010) [10] was chosen because of its effort to become the new standard that will allow for comparisons of different studies. It was also chosen because it offers a relatively efficient and simplistic way of collecting a large amount of data. Another option for determining vesicle texture in volcanic samples is X-ray computed microtomography (XRCMT). This technique can use multiple 2D samples

of a slice of rock which are converted to a 3D illustration of the sample and was first used by Sahagian and Proussevitch (1998) [72] and more recently by a number of others [73] [74] [75] [76] [77]. Okumura et al. (2009) [78] used this technique to study sheared samples and it is a good technique for deformed samples, basaltic lavas and some scoria but it is not adequate for thin glass walls in pumice like the type that were examined in this research [79] [80] [81]. Thin glass walls are so small they would become lost during imaging with this technique, causing artificially inflated vesicularity values. It also cannot reconstruct broken bubble walls easily. The technique of Shea et al. (2010) [10] does not have issues with small objects and allows for reconstruction of broken bubble walls.

Measuring 3D particles in two dimensions has a flaw in general since the probability that the particle is cut directly at its centre is unlikely. Statistical techniques are applied to make 2D data into equivalent volumes that takes into account the probability of cutting bubbles in different planes and attempts to correct the problems that arise from elongated particles [10]. There have been several models to correct for possible intersections of objects [72] [82] [83] [84]. This thesis used the method of Sahagian and Proussevitch (1998) [72] for correcting vesicle size and distributions. Their method uses geometric bins, while their older research used linear bins that didn't account for smaller objects as well [85]. The method is quick and uses iterations of number density but it does not account for elongated objects. This method would also not work well for sheared vesicles because it assumes a given aspect ratio for the whole sample. Pumice generally shows no definite direction of elongation for the whole population and so even if a spherical distribution is not perfectly accurate, it is a better representation than a defined aspect ratio that does not suit the majority of the bubbles [86].

4.2. Other ways of assessing degassing processes

There are several other studies that have been done to assess degassing processes in ways other than with density and vesicularity measurements. Sparks (1978) [12] performed some of the initial numerical modelling of bubble formation and growth. The models considered diffusion and decompression, magma ascent rates, viscosity of magma, gas solubility, gas content and diffusivity for determining bubble growth rates for basaltic explosive and rhyolitic explosive eruptions. Further to Sparks' work, other numerical modelling has been done. Toramaru (2006) [87] performed a series of experiments and a model for bubble formation, using the BND (bubble number density) decompression rate meter method. Masotta and Keppler (2014) [88] used in situ observations of bubble growth in various melts to study the BSD. Gaonac'h et al. (2005) [89] modelled bubble growth from vesicle number densities with a power law using cross sections of pumice samples and then used the bubble

distributions for indicating rheology and eruption characteristics. Simakin et al. (1999) [90], Blower et al. (2001) [91] and Klug et al. (2002) [92] also performed similar research, with power law bubble distributions for a variety of samples. Lovejoy et al. (2004) [93] attempted to model the coalescence of bubbles with a higher-order calculation that accelerates as vesicularity increases, with some background coalescence equations coming from Sahagian (1985) [94] and Gaonac'h et al. (1996b)[95].

Other varieties of studies have focused on alternatives to bubble distributions to infer eruptive styles or characteristics of the ascent of magma through the conduit. Johnson et al. (2008) [96] used volatiles, degassing and crystallization to look at the plumbing system of a cinder cone. The gas content and elements for melt inclusions, groundmass, and tephra crystallinity were examined. Hartley et al. (2014) [97] used melt inclusions to look at degassing of CO_2 from basaltic fissure eruptions and Lloyd et al. (2014) [98] used an ion microprobe to look at melt inclusions in order to relate the volatile concentrations in them to ascent rates and depths. Moitra et al. (2013) [99] quantified vesicle shape in clasts of seven different explosive eruptions, using the results to infer the importance of structural changes from decompression of magma and bubble growth on explosive eruptions of varying types. Wright et al. (2009) [100] measured the pore structure of clasts to determine porosity, permeability and electrical characteristics and tried to relate them to eruption conditions. Other studies in the same vein (Clarke et al. (2002) [101], Melnik and Sparks (2002a,b) [102] [103]) measured volcanic samples to use the permeability and porosity relationship to estimate gas overpressure.

Gonnermann and Manga (2003) [104] looked at viscous shearing as a mechanism for fragmentation in both effusive and explosive eruptions. They also suggested, in the opposing views from the norm, that fragmentation might be important for magma degassing but inhibit instead of help explosive eruptions from occurring.

5. Methodology

5.1. Field sampling

As members of the 25-31 July 2011 eruption expedition to Vatnajökull, Jónas Guðnason, Bruce Houghton and Ármann Höskuldsson, collected clast density samples from the tephra at a proximal section. The section is at $64^{\circ}23.393\text{N}$ $17^{\circ}22.608\text{W}$, a few kilometres south of the vent of the 2011 Grímsvötn deposit, in a west-east oriented crevasse. A photograph of the sampled section can be seen in Figure 5.1. The density clast samples were collected from lapilli dominated units within the tephra sequence, from sections labelled as B, D, and F in Figure 5.1 and in Figures 6.2 and 6.3. In total 12 samples were collected from relatively narrow stratigraphic levels within the stratigraphic sections to ensure that the clasts in each sample were representative for a specific point in time during the eruption.

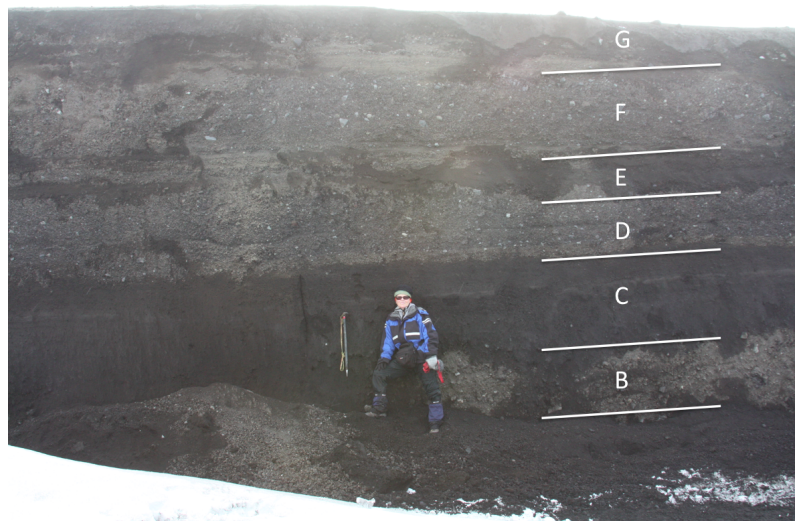


Figure 5.1: A photograph of the sampled section of the 2011 Grímsvötn eruption tephra deposit, at $64^{\circ}23.393\text{N}$ $17^{\circ}22.608\text{W}$. Photo from Magnús Tumi Guðmundsson.

5.2. Density and vesicularity measurements

The method used to determine density and vesicularity is that of Houghton and Wilson (1989) [11]. The samples were cleaned using a sonic bath and dried at 110°C for 24 hours. The clasts of each of the 12 sections were sorted and arranged from 1-100, from smallest to largest. Sample 18P only had 98 clasts available for the measurements. The samples were surveyed for groups of clasts with different macroscopic features such as colour and morphological shape, and all samples had clast populations that were relatively uniform. Clasts were 16-32 mm in size and were selected for measurement because this size range best preserves the vesicle size population at time of magma disintegration as well as be readily available for sampling in most pyroclastic deposits.

The densities of the clasts were determined using Archimedes' Principle by weighing the clasts in air and in water. Archimedes' Principle says that the buoyant force that is exerted on an object that is submerged in water will be equal to the weight of the water that was displaced by the object. Since 1 ml of water is approximately 1 g at 1 atm pressure and 4 °C, this relationship helps us to calculate the volume of an object and hence, along with the weight in air, we can calculate the density of the clast.

All of the measurements and calculations for the densities and vesicularities of the clasts can be found in Appendix A. The following paragraphs describes the methods of measurement and calculation.

Simply, density is calculated with mass of an object divided by its volume.

$$\rho = \frac{m}{v} \quad (5.1)$$

where

- ρ = density (g/cm^3)
- m = mass (g)
- v = volume (ml)

The mass is calculated by weighing the clast and the volume is calculated through Archimedes' Principle from the displacement of water [105].

The density of each clast was determined by first weighing the clast in air to a

precision of 1/100 of a gram. Each clast was then wrapped in a wax film of known weight and labelled 1 through 100, from smallest clast to largest clast. The wax was used because it can be cut into squares of known weight and provides a waterproof barrier, sealing vesicles in the clasts. It is malleable and with body heat is molded to the larger contours of the clasts. The number of squares of wax used to entirely cover the clast was recorded and then the weight of each clast in water was also recorded. An alternative to the wax film used to create a waterproof barrier are a silicone-based aerosol spray that can be used for fabrics to create a waterproof layer and is useful for pumice that is micro vesicular as the spray is considered to have negligible mass and can simplify calculations.

After the clasts were given a waterproof wax barrier, the clast was weighed in water. To suspend the clast in the water, a set up of an upright T-shaped metal rod was used, with a metal stick with a open-coil metal ball at the end, in which the clast was placed. If the clast floated, it was weighed down with a small steel ballast and the weight of the ballast was subtracted from the measured weight to get the wet weight of the clast.

The specific gravity, can then be calculated with the following equation:

$$SG_c = \frac{w_a}{w_a - [w_w - w_b + (w_f \cdot n_f)]} \quad (5.2)$$

where

- SG_c = specific gravity of the clast
- w_a = weight of clast in air (g)
- w_w = weight of clast in water on ballast (g)
- w_b = weight of ballast (g)
- w_f = weight of wax film (g)
- n_f = number of pieces of wax film used on clast

To get the density of each clast using specific gravity, the specific gravity was multiplied by the density of water, which is approximately 1 g/cm^3 .

$$\rho_c = SG_c \cdot \rho_w \quad (5.3)$$

where

- ρ_c = density of the clast (g/cm^3)
- ρ_w = density of water (g/cm^3)

The density can then be converted to a vesicularity through the following equation:

$$V = \frac{100(\rho_{DRE} - \rho_c)}{\rho_{DRE}} \quad (5.4)$$

where

- V = vesicularity (%)
- ρ_{DRE} = density of DRE (g/cm^3)

The ρ_{DRE} is the density of the dense rock equivalent, or DRE. The DRE is a non-vesicular juvenile clast of tephra and in this research $\rho_{DRE} = 2.75 g/cm^3$ based on Sigmarsson et al. (2013) [58] calculations. This value comes from measurements of density of non-vesicular juvenile clasts of the same composition as the density sample clasts.

The density values of the 100 clasts from each sample were then binned to determine frequencies of the density measurements. These values were graphed in histograms. The vesicularities were also graphed in histograms by the same method (Figures 6.6 to 6.8). These histograms were used in the next section for selecting representative samples.

The sources of uncertainty within the density measurements include the human error of measurement and recording, the proper application of wax film for waterproofing the clast, and weighing down clasts that are floating in water properly. In an attempt to minimize errors when weighing and recording the weight of the clasts, clasts were arranged and weighed in increasing size order. When waterproofing clasts with the wax, it was important to carefully cover all vesicles and great care was taken in this process to minimize errors. Due to their high vesicularity, many of the clasts could float in water. They were weighed down with a ballast for weighing the clasts in water and the weight of the ballast was subtracted from the weight in order to minimize weight errors, in a case where the clast could float.

5.2.1. Selecting representative samples

The samples were chosen for further investigation based on a few criteria. The first criterion was that the selected sample should be representative of a time equivalent horizon in the tephra deposit (i.e. a short time interval during the eruption). Secondly, the clasts should be between 16-32 mm. Lastly, the sample set should cover all, or as many, phases of the eruption as possible. In some cases, the size of the clast was considered, as the method for making plugs required that the clast was small enough to fit into a small cylinder of diameter approximately 25 mm. To retain the integrity of the clasts, it was better not to break the clast and having smaller clasts to make the plug allowed for using the entire clast during the impregnation stage as described in the next section.

5.3. Preparing the samples for imaging

The clasts that were chosen for further investigation of vesicles, were imaged in the SEM. These clasts were first made into plugs of less than 17 mm thickness. Thin sections were not made because the clasts were highly vesicular and making a thin section of 30 microns, while retaining bubble walls and ensuring that all vesicles were filled with epoxy, would be challenging.

The eight clasts were first cleaned in a sonic bath for five minutes and dried at 110° for 30 minutes. The clasts were then put individually into small plastic cylinders with a bottom but no cap. Each cylinder was first coated with a thin layer of Buehler Release Agent (2,2,4-trimethylpentane) to prevent sticking of the epoxy. An epoxy was mixed from 5.00 parts Buehler EpoThin Epoxy Resin and 1.95 parts Buehler EpoThin Epoxy Hardener. A very small amount of Keystone blue dye from Logitech was mixed into the epoxy. The blue dye was used to provide contrast, for viewing the vesicles in scanned images and with the naked eye more easily. The epoxy was then poured into the cylinder, covering the clast. The cylinder was placed in a vacuum which was evacuated to allow the epoxy to impregnate the vesicles. By using a vacuum, the epoxy boils, filling as many of the clasts' bubbles as possible. The sample was in the vacuum until it boiled for one to two minutes. After the cylinder was removed from the vacuum, the clast was transferred to a different cylinder without a bottom, which was adhered to a silicone mat. This cylinder was also coated in release agent and the clast was oriented with the flattest side down. The epoxy was poured on top, to a maximum of 25 mm height. The sample was placed in a pressure chamber, which was held at 2 bars, and was left overnight to harden.

When the clast was removed from the cylinder, it was labelled with a diamond scribe and one side was sanded down to a surface that exposed the sample and the filled vesicles. This was first done on a Hillquist Thin Section Machine, which is a thin section water saw and grinder unit. After it was roughly ground to the surface of the clast, microgrit sand paper of 280, 400, 600 and 1000 sizes were used to polish the surface. The samples were placed in a sonic bath for 5 minutes, dried and then examined in an optical microscope to observed if all the vesicles has been filled. Any additional bubbles that were not filled during the initial impregnation, and were now exposed on the surface, were filled. To do this, a small batch of epoxy was made and using a small spatula tool, a thin layer was spread on the surface. The sample was placed in the vacuum to boil the epoxy and the surface was smoothed again with another thin layer of epoxy before it was put in the pressure chamber overnight again to dry. After it was dry, the surface was polished, and extra care was taken to make the surface as smooth as possible, removing scratches but not the epoxy from the vesicles or breaking the vesicle walls. The same microgrits of sand paper were used and additionally, 1500 and 2000 grit were used. Final polishing was performed using the Buehler MetaServ 250 Grinder-Polisher with the Vector Power Head. Samples were placed in the device with various grits of 9, 3, 1 and 0.3 microns. The semi-automatic grinder-polisher's applied force was set to 8.89 N (2 lbs) for up to two minutes at the different grits. Water and a liquid grit were also applied to help lubricate the samples. After the final polishing, the samples were cleaned in a sonic bath for five minutes and dried. The samples were now ready to be imaged in a scanner.

5.4. Image strategy and acquisition

The methods used for image acquisition are derived from the work of Shea et al. [10]. It is through image analysis that vesicle distributions are determined.

The largest vesicles are best first imaged by a scanner. The 8 uncoated samples were imaged with the CanoScan 5600F scanner at 1200dpi. These images were assessed for clarity of bubble walls and some were repolished according to the steps in the section above and reimaged. Of the eight samples, only four were chosen to be used for the rest of the analysis as some plugs did not provide a good enough image on the scanner to continue and, in the interest of being concise because of the time needed for image acquisition and rectification, four samples were determined to be a good number to represent the eruptive products of this eruption.

Once each plug had been imaged with the scanner, a gold coating was applied to the surface for use in the SEM. The coating is necessary for increasing electrical conductivity of the sample that is needed for the imaging process. The Cressington

Sputter Coater 108auto was used to apply a thin gold layer to the surface. The sample was placed in a small chamber and the air was removed to create a vacuum in the chamber. The coater was turned on and the gold target in the chamber was bombarded with argon gas particles. This causes a glow discharge between the anode (the gas) and the cathode (the gold target), called sputtering, whereby the gold atoms are deposited on the surface of the sample. The sample was removed and then placed on the stage of the SEM. A metal tape was applied from the top surface of the sample touching the gold coating to the base of the stage which is also metal. This ensures good conductivity for the imaging process.

The Hitachi TM3000 SEM was used in backscattered electron imaging mode. Images were achieved by loading the sample, evacuating the chamber to create a vacuum, turning on the computer program and changing the contrast and brightness of the image until the image was nearly binary, with the black being the bubbles and the white being the pumice walls (melt). By zooming in and out, and using a nested image technique, each sample was imaged as shown in Figure 5.3.

The methods of Shea et al. [10] were reviewed to determine the best strategy of imaging with the minimum necessary photos to be taken to allow the maximum number of samples to be processed in the available time. A grid system with 25 images, where for example, 1 scan at 5x magnification is taken and then 8 images at each of 25x, 100x and 250x is taken was not used because it provides very similar amounts of objects per melt area as shown in Figure 5.2. The 73 grid system uses a similar technique but imaging more surface area of the sample. The grid options use far more images, requiring more time to process images and collect the data than with the exponential nest option (Figure 5.2d). A possible problem that the grid nest avoids is the user-induced bias of assessing heterogeneities. If the sample is homogenous in terms of the bubble distributions and texture, then the exponential nest should represent the whole sample well. If instead, it has various regions of heterogeneities, then the user may miss these variations, introducing a bias in the data. The grid nest avoids this by systematically scanning large areas of the sample.

Images for this study were taken in accordance with the exponential nesting strategy described above, but with slight modification. The strategy is illustrated in Figure 5.3. The first 5x magnification image was taken with the scanner and the following images were taken with the SEM. The 4 images were taken at 50x magnification because the SEM used does not allow for lower magnifications and were taken in an overlapping fashion in an effort to cover a larger area to replace the 25x image that is recommended. Also, the Image Magnification Ratio (IMR) was modified slightly from the standard technique. Instead of 2 images at 25x, only 1 image was used and 3 images at 100x were used instead of 2. These changes were made to ensure adequate coverage of the vesicles in each sample. Rules that were followed to determine the best strategy and number of images are in line with those put forth by Shea et al. [10]. Considerations were made for:

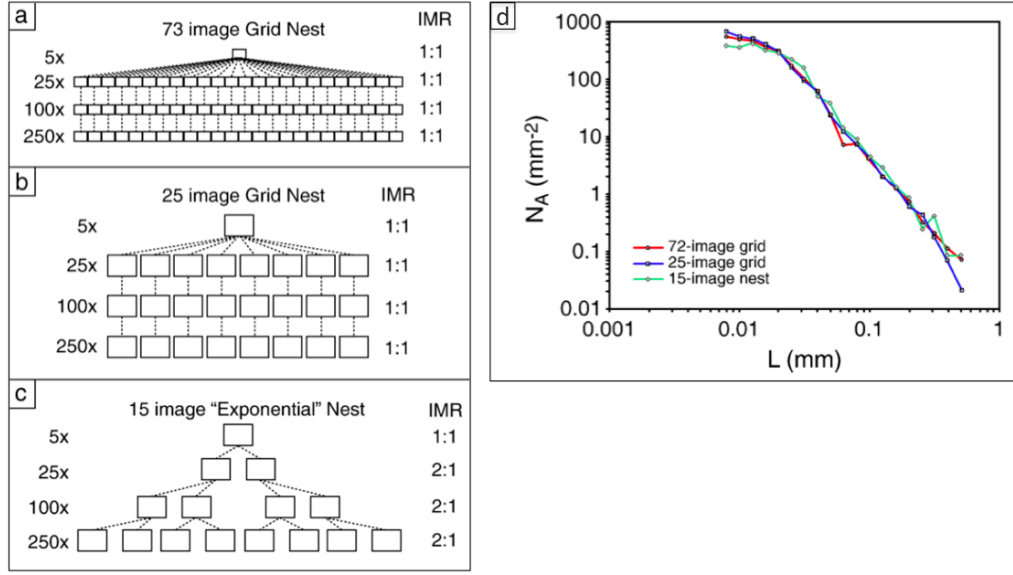


Figure 5.2: The grid nest imaging vs exponential nest imaging approach. From Shea et al. (2010) [10].

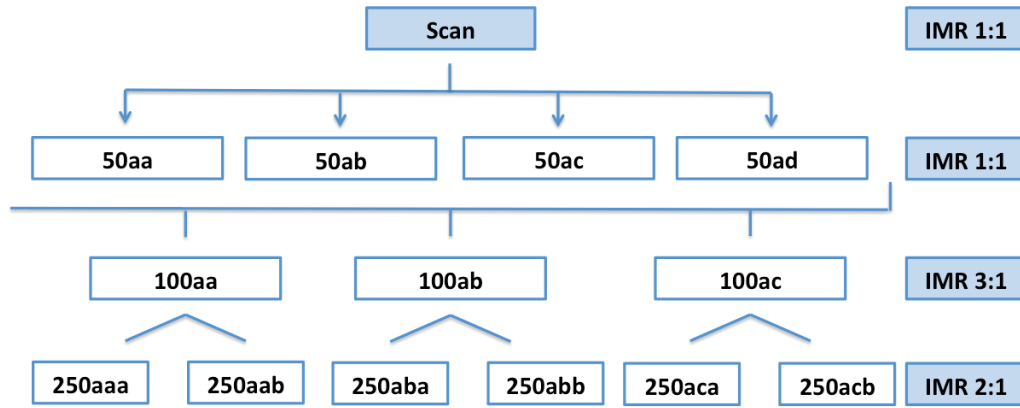


Figure 5.3: Illustration of the 11 image exponential nest used in this research.

- Homogeneity of the individual clasts
- Time needed to take images and rectify them
- Range of vesicle sizes
- Acceptable error percentage
- Number of vesicles per image
- Overlap of vesicles in images

All four samples were homogeneous enough to the degree that the exponential nest strategy was deemed the most effective option, as user-bias would be minimal and it would be the most time-efficient strategy. In addition, the high vesicularity of the samples means that fewer nests are needed for a good representation of the vesicle populations.

The lowest magnification was chosen to be at least 1-2 orders of magnitude larger than the largest bubbles. The highest magnification was chosen so that the smallest vesicles are imaged adequately. Figure 5.4 shows the calculations of Shea et al. [10] for assessing the error that one incorrect pixel introduces to the measurements based on diameter of the vesicle and the magnification of the image. If a spherical bubble is imaged at a magnification and is partially covered by a square pixel, with the remainder of the pixel covering the melt, the bubble area will be overestimated and an error will be introduced. The error produced by one erroneous pixel depending on the size of the vesicle (Figure 5.4a). The smallest vesicle imaged in the Grímsvötn 2011 samples was 13 pixels in equivalent diameter. This would produce less than a 1.5% error and is deemed satisfactory for this study. Using this same equivalent diameter as the minimum size vesicle imaged at a 250x magnification (Figure 5.4b), the smallest vesicle can be adequately represented by a 15 pixels equivalent diameter at approximately 250x magnification with 0.6% error with the erroneous placement of one pixel. For comparison, accepting a 1.3% error at a magnification of 250x, the smallest vesicle would need to have an equivalent diameter of approximately 4 microns or 7 pixels.

Shea et al. [10] recommend having at least 10 objects per image at the highest magnifications and not more than 100 of the smallest sized objects. All of the samples satisfy this requirement at 250x. The magnifications that were used were also chosen based on having a certain degree of overlap of vesicles at each magnification.

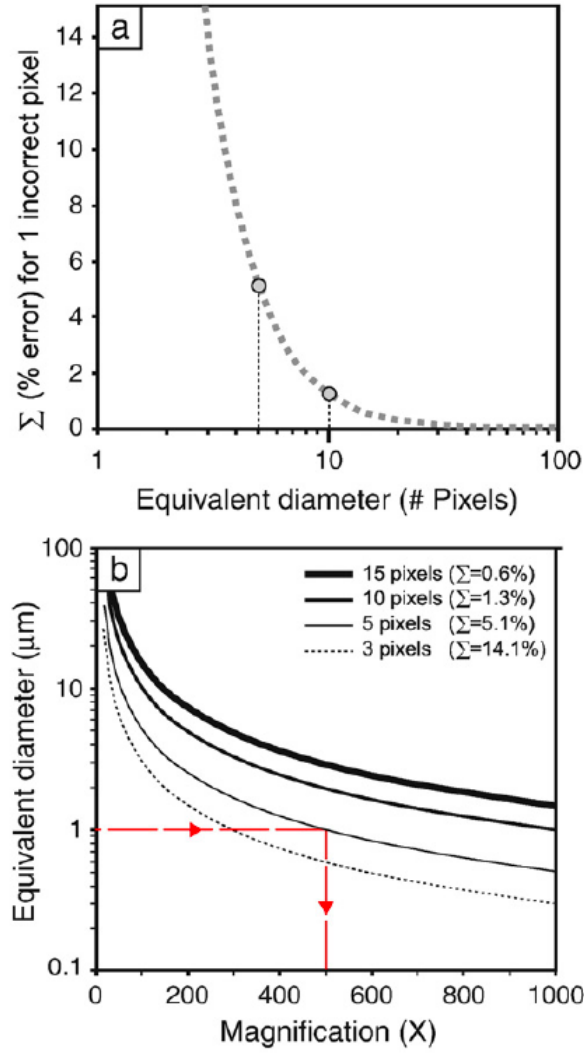


Figure 5.4: a) The error from the misrepresentation of one pixel given the size of the vesicle. b) Minimum vesicle diameter for given magnifications. From Shea et al. (2010) [10].

5.5. Image rectification

After the images were taken with the scanner and the SEM, the images were rectified using the GNU Image Manipulation Program (GIMP) [106]. This was done to make the images binary (all pixels are black or white only) as the software in the next step identifies the objects in binary. The scans were done first by outlining the visible and largest vesicles in black and colouring the melt in, in white. The SEM images are grey scale and this process is a bit faster in GIMP [106], as one can make a second layer from the original and select the threshold tool to make an image binary. The next step was to clean the image as much as possible to match the original.

Additionally, areas between vesicles must be 3 pixels or greater. Any phenocrysts were made black as well and must be included on a separate layer for use in the ImageJ software separately [107]. Once the images were cleaned, the bubbles must be decoalesced. This was done with care in order to preserve bubble walls. Again, this must be done with 3 pixels in between bubbles. Figure 5.5 shows an example of the original image (a), the cleaned image (b), the image with crystal added (c), and the final decoalesced image (d) that then was analysed with the ImageJ software [107]. The final image is exported and saved in TIFF file format.

The greatest amount of uncertainty here is introduced by manually decoalescing the vesicles. The vesicles were decoalesced by examining the textures and shapes of the vesicles and by considering the physics behind how a smaller and larger bubble interact with each other. However, if the vesicles are systematically decoalesced more than necessary, it can affect calculations for the vesicle size distribution, vesicle volume distribution, and vesicle number density. For example, if all vesicles are systematically decoalesced to be 50% smaller than they are in reality, the vesicle size distribution will shift to smaller vesicle sizes but the distribution pattern would remain the same.

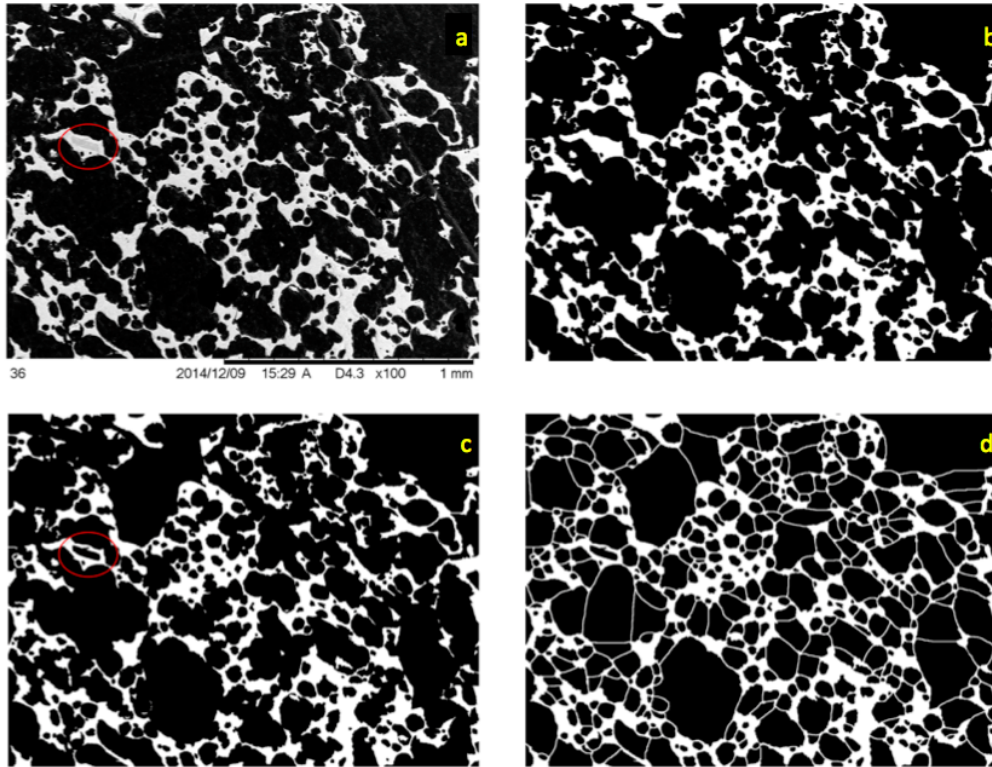


Figure 5.5: Clast 19P 74, imaged at 100x magnification. a) Original SEM image. Red circle is crystal. b) Image cleaned in GIMP. c) The image with the crystal added, as seen in the red circle. d) Final decoalesced image.

5.6. ImageJ

ImageJ is a software that is written in Java, is in the public domain and is available for free download at the National Institute of Health (NIH) website [107]. It was developed by Wayne Rasband at the NIH in Maryland, USA and can be used with most operating systems. Detailed user guides are also available at the website. It was developed for image processing and analysis in the medical field but its uses extend beyond this into other types of image processing. ImageJ can perform many processing techniques on various image files but the primary file format used in this research was TIFF and the common tasks performed were to edit, analyze and process, the details of which are described in the next section [107].

5.6.1. Software analysis

The ImageJ software technique applied in this study was set out by Bruce Houghton and coworkers at the School of Ocean and Earth Science and Technology at the University of Hawai'i at Manoa [107].

Each corrected and decoalesced image from the SEM and scanner was opened in their TIFF file format in ImageJ and processed separately. The first step is to make the image binary in ImageJ. Smoothing then takes place using the "open" feature. This performs an erosion and then dilation to remove individual pixels and to smooth some objects minorly. Before performing the smoothing, iterations was set to 1 to ensure this process only occurred once and count was set to 4. The count value lets the program know that a pixel should only be removed or added if the 4 adjacent pixels are a different colour from the individual pixel. The next step involves the "analyse->measure" tool. This gives the mean greyscale value for the vesicles of the image and is used later in the data organization step. This value gives an indication for the relative proportion of black (vesicles) versus white (walls) in the area of the image. White is given the value 0, and black is the value 255. The value will lie somewhere between these values based on the ratio of white and black in the image. This value is later referred to as the vesicles mean greyscale value, G_v .

The next step was to select the vesicles which were touching the edges of the image so that these partially imaged vesicles would not be used in further calculations. With these selected vesicles, a mask was created. The "analyse->measure" tool was used again on the masked vesicles to get a value between 0 and 255, measuring the white to black pixels. This value is later referred to as the edge-vesicles mean greyscale value, G_e .

The second stage of the analysis is performed on the image without the mask area

(edge vesicles). First the distance in pixels of the image itself was set based on the original magnification of the scan or SEM image. Next, parameters that the program will measure were selected in the settings. These parameters were area, mean grey value, minimum and maximum gray value, perimeter, fit ellipse, shape descriptors, Feret's diameter and area fraction. With these parameters, the "analyse-particles" function was used for analysing ellipses, outlines and masks. The principal data obtained from this second stage of the analysis is the area of each vesicle and is generated by the "analysed-particles" function in ellipse mode. This function provides a count of the number of bubbles within the image (excluding the mask) and provides an area of each bubble in units of mm^2 . This count is derived from applying the best fit ellipse to each bubble.

A third stage of the analysis is performed on 8 of the originally obtained 44 images, only those featuring crystals (i.e. macrocrysts) dispersed throughout the bubbly glass groundmass. Before processing, the images are modified to highlight the crystals over a white background. Each image was made binary and then analysed in ImageJ with the "analyse->measure" tool to obtain a mean pixel value (0-255) of the amount of white (the background) to black (the crystal). This value is then used to find a modal percentage of macrocrysts. All of the samples have very low phenocryst modes, with only 1 of the 8 samples having an amount $>0\%$. The effects of this will be discussed in the following section.

5.6.2. Data organization

To organize the output from the ImageJ analysis, a spreadsheet was created for each of the clasts. The data for each clast was organized separately, however the data for images of similar magnifications within the clast data were combined. The final outputs are the NA, NV, and NVm values, as well as several graphical representations of the data (see Results section).

The first inputs into the spreadsheet are the areas of each vesicle. This effectively also counts of the number of bubbles within the image and provides an area of each bubble in units of mm^2 . The data is grouped by magnification and combined into columns containing the individual area measurements for all bubbles at that magnification. The objects measured per magnification were also recorded in the spreadsheet.

Several calculations are carried out for each individual image that was captured of that clast. The following sections describe the values that were calculated.

Reference area

The total image area is calculated by:

$$A_T = \frac{A_p}{(SF)^2} \quad (5.5)$$

where

- A_T = total image area (mm^2)
- A_p = total image area (pixels²)
- SF = scale factor (pixels/mm)

The total image area used is calculated by the image width multiplied by the image height in pixels. The scale factor for SEM images is found by measuring the scale bar in pixels and dividing by the scale to have a factor in pixels/mm and the scale factor for a scan is found by dividing the dpi of the scale by 25.4, also giving a scale factor with units of pixel/mm.

The reference area is calculated by:

$$A_R = A_T - A_T \cdot \frac{G_e}{255} \quad (5.6)$$

where

- A_R = reference area (mm^2)
- G_e = edge-vesicles mean greyscale value (unitless)
- 255 = the highest value indicating area is all black (entirely composed of vesicles)

This calculation is the subtraction of the mask area from the total image area to get the reference area, or the analysed area.

The vesicle fraction is calculated by:

$$V_f = \frac{G_v}{255} \quad (5.7)$$

where

- V_f = vesicle fraction (unitless)
- G_v = vesicles mean greyscale value for all vesicles in image (unitless)

The vesicle fraction, multiplied by 100%, gives the vesicularity in percentage of each individual image. The average of the 11 image vesicle fractions for each clast can be calculated to give the overall sample vesicularity as calculated by image analysis. This however, includes the edge vesicles and smaller vesicles have not been removed from the calculation.

The phenocryst fraction is calculated by:

$$P_f = \frac{G_c}{255} \quad (5.8)$$

where

- P_f = phenocryst fraction (unitless)
- G_p = phenocryst greyscale value (unitless)

This calculation is the value, that if multiplied by 100%, gives the percentage of crystals in the image. It works by taking the greyscale value, or value of black pixels on a white background, in this case crystals on a white background of the image, and comparing them to an entirely black image which has a value of 255. This value is of phenocrysts only [107].

Number density of vesicles

This section discusses the calculations for NA and NV. NA is the measured number density of vesicles (mm^{-2}).

The next step is to calculate the number of vesicles per unit area, NA, by first using the vesicle area measurements from previous steps and finding the equivalent diameter. This is done with the combined areas that are generated by the ImageJ software and should be organized by magnification.

The equivalent diameter, EqD, is the diameter of a sphere that is the same volume of the irregular shape in question. The EqD for each vesicle is calculated by using the geometry of the area of a sphere and the area of each vesicle generated by the ImageJ program:

$$EqD = \sqrt{\frac{4 \cdot A_v}{\pi}} \quad (5.9)$$

where

- EqD = equivalent diameter of a vesicle (mm)
- A_v = area of the vesicle (mm^2)

The equivalent diameters are then binned by value, with each bin being larger than the previous by 100.1 times. Working backwards, the minimum vesicle size dictates the smallest bin size. For the next lowest magnification, the lowest bin will be the next bin after the largest bin size from the magnification that is one higher. For this study, a minimum of 15 pixels is automatically set for the minimum vesicle size as the SEM at the Institute of Earth Sciences has a lower resolution of 50x magnification than that of other, similar work of 25x magnification. In doing this, the results can be compared to other research with similar methods more easily.

Only the vesicles that are counted in the particular magnification bin will be used in the further calculations. For each magnification, the number of vesicles included, V_I , is noted. The bins that are selected for each magnification are on the basis of avoiding empty bins and eliminating gaps in the data collection. Also, the bins are selected such that the decrease of the NA (number density of vesicles) with increasing bin size, is as smooth as possible.

The bulk NA is also a useful value to compute for comparison of how the NA is distributed among the size classes. The bulk NA, $(NA)_B$, for each magnification, is calculated by:

$$(NA)_B = \frac{V_I}{A_{RM}} \quad (5.10)$$

where

- $(NA)_B$ = bulk number of vesicles for a unit area (mm^{-2})
- V_I = vesicles included in reference area
- A_{RM} = reference area for the magnification (mm^2)

The reference area for the magnification, A_{RM} is calculated by summing the reference areas of each image of similar magnifications. As before:

$$A_{RM} = A_T - A_T \cdot \frac{G_e}{255} \quad (5.11)$$

If the reference magnification is 100x, three images are required to calculate the sum, or the total reference area, for the reference magnification, A_{RMT} (mm^2) as:

$$A_{RMT=100} = A_{100aa} + A_{100ab} + A_{100ac} \quad (5.12)$$

The NA for each bin is calculated by taking the frequency of vesicles in the bin and dividing by the reference area for that magnification.

$$NA_{bin} = \frac{f_{bin}}{A_{RMT}} \quad (5.13)$$

where

- NA_{bin} = number of vesicles in the bin per unit area (mm^{-2})
- f_{bin} = frequency of vesicles in the bin (unitless)
- A_{RMT} = total area from the images in the reference magnification (mm^2)

After the above calculations were performed for the individual magnifications, they were repeated to get data on the clast as a whole. By using the bin and NA data from the chosen bins for each magnification, a graph of number of vesicles per unit area (NA) versus vesicle size (EqD) was plotted. The NA of crystals was used for NA in this case, if phenocrysts existed in the images. The NA of images of a particular magnification, was adjusted if in that magnification, a value $>0\%$ was determined for phenocryst fraction earlier, P_f .

Methodology

The adjusted NA for phenocrysts, NA_P is calculated by:

$$(NA)_P = \frac{(NA)_{bin}}{1 - P_f} \quad (5.14)$$

where

- $(NA)_P$ = number of vesicles per unit area (in a particular bin), adjusted for phenocrysts (mm^{-2})

The number of vesicles per area, NA (mm^{-2}), is calculated by summing all NA values for each bin.

$$NA_T = \sum_{bin=1}^{32} NA_{bin} \quad (5.15)$$

where

- NA_T = total vesicles per area of the clast (mm^{-2})

Vesicle size distribution

The VSD is plotted with vesicle size (mm) versus $\ln(n)$.

The n value is calculated by dividing NV by the lower size limit of the bin. This lower size limit for each bin is calculated in the same way as the vesicle size above except class 24 is set to the minimum size (mm) and class sizes >24 are equal to the vesicle size of class x-1, divided by $10^{0.1}$. For class sizes <24 , the vesicle size equals the vesicle size of the class size x+1 multiplied by $10^{0.1}$. The NV values are as before. The \ln value is then taken of the n value (mm^{-3}), which serves as the value on the y-axis and is the number density of vesicles.

Vesicle volume distribution

Each geometric bin above is assigned a class number of 1 through 32, with the largest bin being class size number 1.

The next step is to record the alpha values, $\alpha(\text{unitless})$, assigned to each class size. These alpha values were originally suggested by Sahagian and Proussevitch [72] as a way to introduce the probability variable into the calculations. Their original alpha values were only given for 10 size classes and therefore, the 32 alpha values for the class sizes that are used in this study are obtained from the work of Kathy Cashman (Bruce Houghton, personal correspondence, 2015).

Hbar (mm), is the mean projected height by a spinning particle about a randomly oriented axis that changes. In this research, Hbar is represented by the diameter of the spherical particle of each size class. For each geometric bin, the mid-point in a volume linear scale is used. This is calculated by taking the average of the volume of the bins x and $x+1$, where x = class size number. The volume of the bins themselves are the geometric bin values cubed. The cubed root of the average is then taken to get the Hbar value.

The alpha value and Hbar value are required to get the number of vesicles per volume, NV (mm^{-3}) of each bin. The sum of the NV values of each bin will be the total NV of the clast. NV for a bin was calculated by using Equation 3 in Sahagian and Proussevitch [72]. It makes the 2D data into 3D by way of an iterative process. The larger vesicles that would have been cut at less than their maximum diameter are discounted, since otherwise they might be included as whole vesicles in a smaller class size.

The volume of a sphere with equivalent diameter to Hbar is calculated by:

$$Vol_s = \frac{\pi \cdot Hbar^3}{6} \quad (5.16)$$

where

- Vol_s = volume of sphere with equivalent diameter of Hbar (mm^3)

The volume fraction was then calculated by:

$$F_v = NV \cdot Vol_s \quad (5.17)$$

where

- F_v = volume fraction

The adjusted volume fraction, F_a , is then calculated using a corrective multiplication

factor. This factor is the density-derived vesicularity divided by the sum of the volume fractions. This factor is used if the total volume fraction disagrees with the density-derived vesicularity (otherwise the multipliative factor would have a value of 1). For the same reasoning, the number of vesicles per volume, corrected for melt, NV_m is calculated by multiplying the NV of the clast by 100 and dividing this product by 100 minus the density derived clast vesicularity.

Number density versus vesicularity

Finally, the number density of vesicles, adjusted for the melt, NV_m (mm^{-3}) is plotted against the VG/VL. The VG/VL value is the volumetric ratio of vesicles to melt or the vesicularity of the gas, VG (%) over the vesicularity of the liquid, VL (%) [108].

$$VG/VL = V/(100 - V) \quad (5.18)$$

where

- VG/VL = the volumetric ratio of vesicles (G, gas) to melt (L, liquid)

Points are plotted for the clasts that were imaged and analysed. The calculated vesicularities are used, as well as the mean vesicularity for the sample section from which the clast is derived. The NV_m is assumed to be the same for the mean as for the clast in order to plot the mean points.

6. Results

6.1. Stratigraphy

The stratigraphy of G2011 is graphically displayed in Figures 6.2 and 6.3. There are six units labelled B through G. There are two types of units; pumice lapilli units (B, D, and F) and ash-grade units (C, E, and G). The pumice units have mainly lapilli-sized grains with narrow grain size distribution as the lapilli units have little ash, they are relatively well sorted and clast supported. The ash-grade units have ash-sized grains however the grain size distribution is broad with dispersed pumice lapilli clasts. They are relatively poorly sorted and are matrix supported. All the units feature distinct internal stratigraphy, which suggests that each phase was produced by distinct pulses of deposition. This may in turn, translate into pulsating explosive activity during each phases and may imply that each unit represents a distinct eruption phase. By examining the eruption plume height, it is possible to correlate explosive or intensity pulses to each unit.

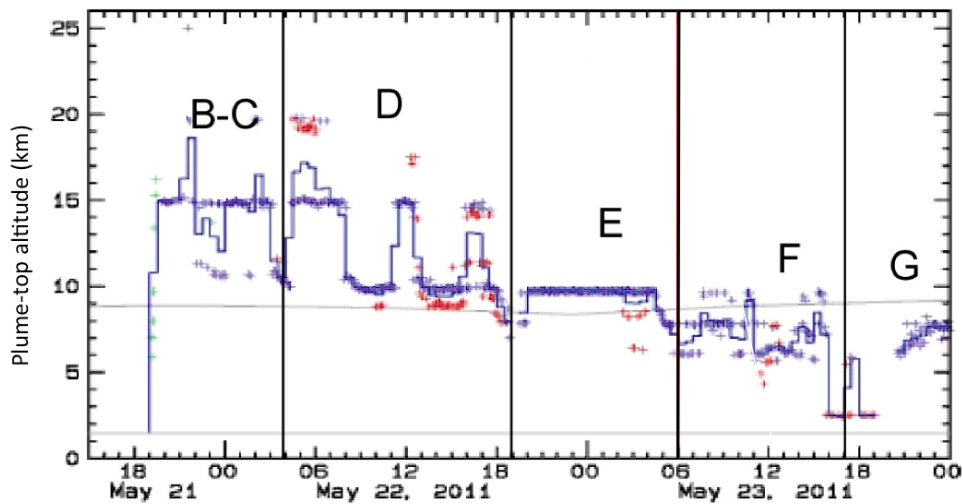


Figure 6.1: The height of the eruption plume with time, with approximate divisions of the stratigraphic units (IMO radar data and personal correspondence Ármann Höskuldsson, 2015).

Results

The eruption column height is illustrated in Figure 6.1. Maximum plume height was in the first 9 hours of the eruption and was between 17-19 km high. This period is considered the time-frame when units B and C were erupted, a pumice lapilli unit and ash-grade unit respectively. Beginning at 04:00 on 22 May, there were three peaks in activity of approximately 17 km, 15 km and 13 km. There were also periods of lower plume height around 10 km. This is considered the time-frame of the largest pumice lapilli unit, D. From 19:00 on 22 May until 06:00 23 May, the plume remained steady at 10 km high and likely produced the E ash-grade unit. The F lapilli unit was produced from 06:00 until 17:00 on 23 May, when the plume fluctuated between 7 km and 10 km and dwindled to 3 km (or undetectable levels) in the last hour. The final unit G, was erupted after 17:00 on 23 May when the plume was around 3-6 km high for a few hours.

The column height can be used to calculate the discharge. Table 6.1 shows the calculations for discharge during the production of each unit based on the maximum and mean plume heights. In accordance with Mastin [109]:

$$H = 1.67Q^{0.259} \quad (6.1)$$

where

- H = plume height (km)
- Q = dense rock equivalent discharge rate (m^3/s)

The dense rock equivalent discharge rate, Q, is converted to mass flow rate (discharge, kg/s) using a magma density of 2750 kgm^{-3} .

Table 6.1: Maximum and mean plume heights and mass discharge rates for each unit.

Unit	Value	Plume height (km)	Mass discharge rate (kg/s^1)
Unit B-C	max	19	3.3E+07
	mean	15	1.3E+07
Unit D	max	17	2.1E+07
	mean	12	5.6E+06
Unit E	max	10	2.8E+06
	mean	10	2.8E+06
Unit F	max	9	1.8E+06
	mean	7	7.0E+05
Unit G	max	5	1.9E+05
	mean	3	2.6E+04

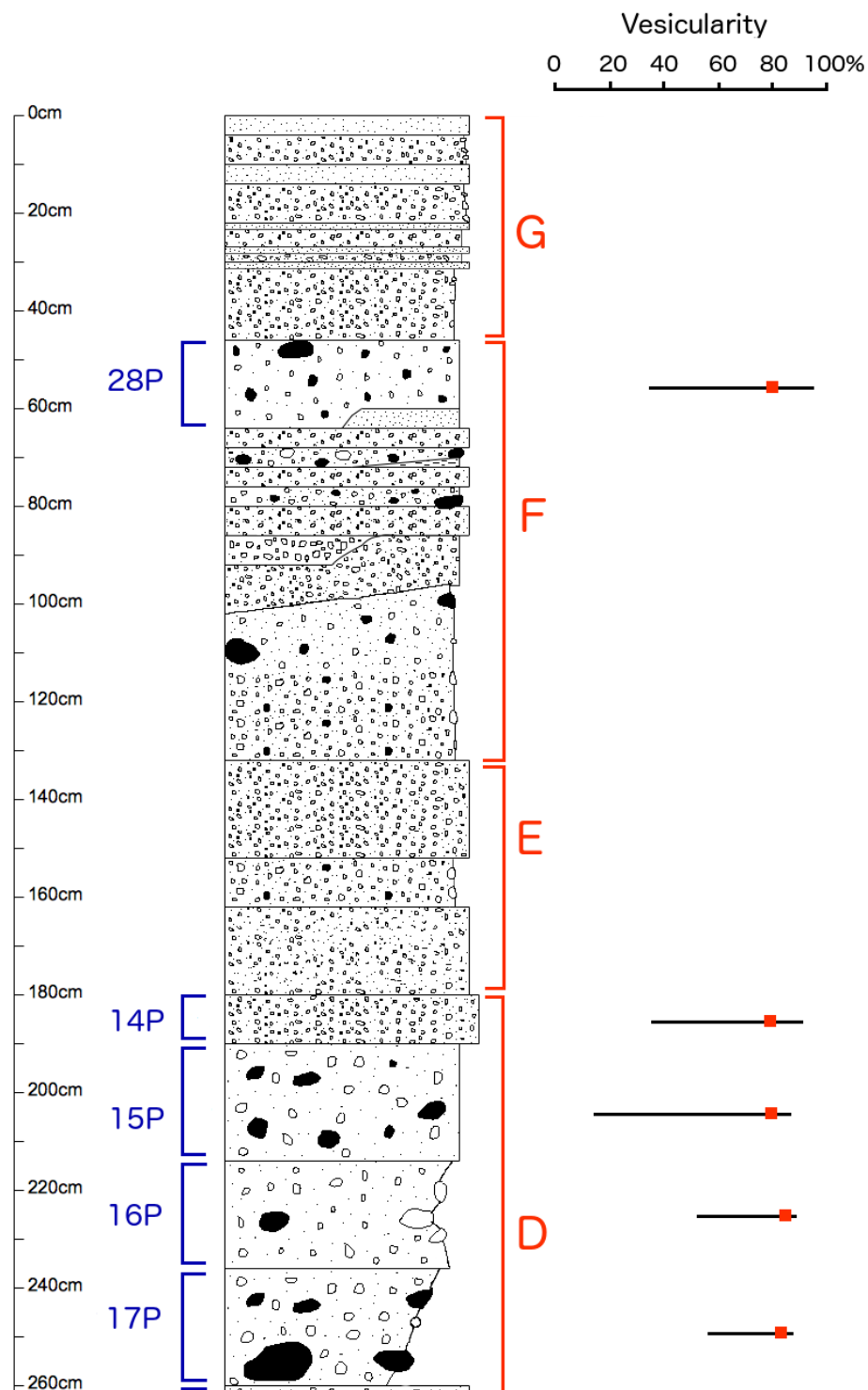


Figure 6.2: 1 of 2. Stratigraphic column, 2011 Grímsvötn deposit. Blue, density samples; Orange, phases; Red square with lines, mean vesicularity and the range.

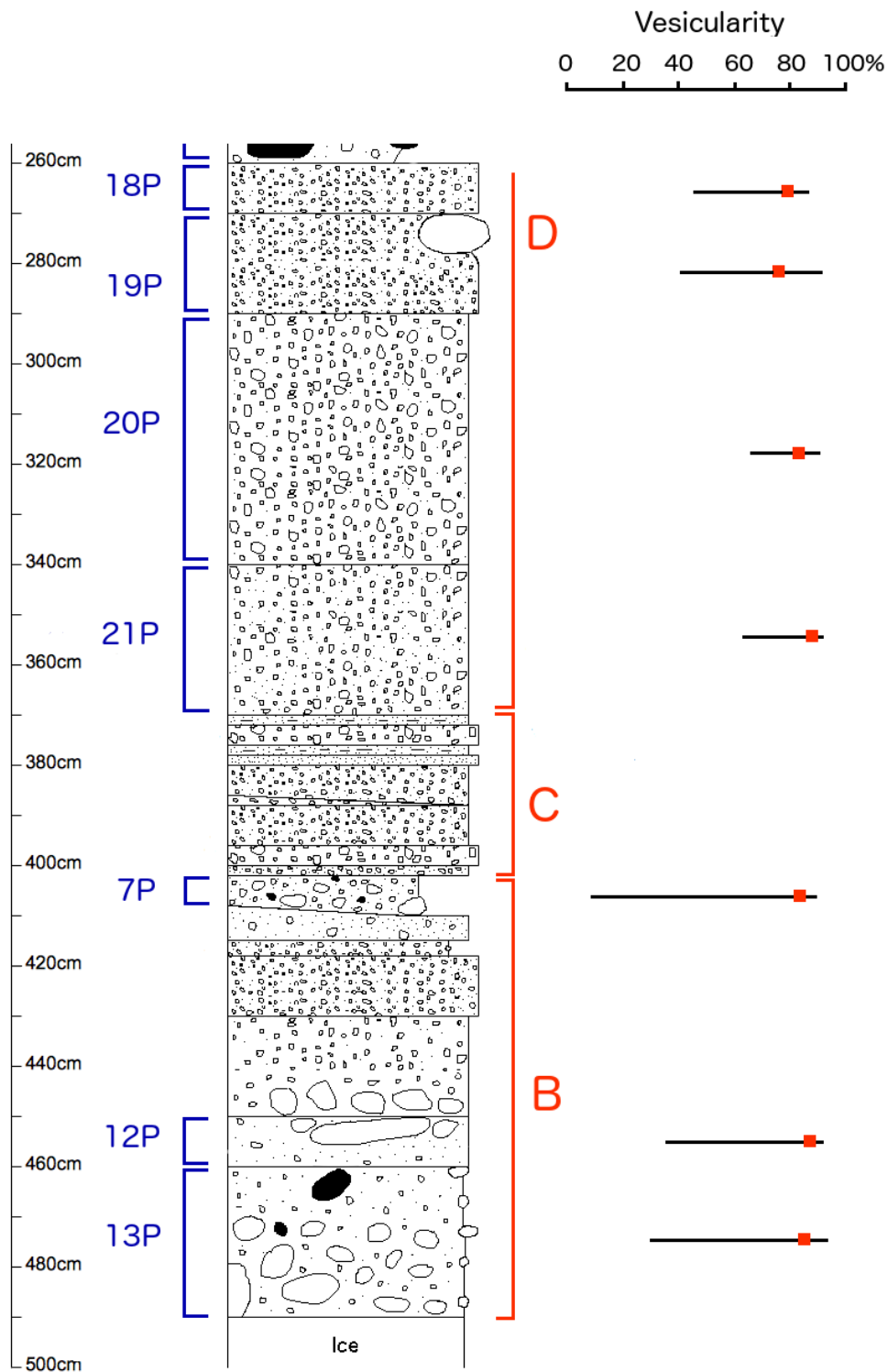


Figure 6.3: 2 of 2. Stratigraphic column, 2011 Grímsvötn deposit. Blue, density samples; Orange, phases; Red square with lines, mean vesicularity and the range.

6.2. Density and vesicularity measurements

The density measurements were performed on all 1198 clasts. The full measurements and calculations can be found in the appendix. Table 6.2 shows, in the order they were erupted, the mean density and mean vesicularity for each of the samples based on the measurements of 100 clasts in each sample, except one (98 clasts measured).

Table 6.2: The mean density, ρ_m and mean vesicularity, V_m measurements for the 12 samples from Grímsvötn 2011.

Sample	ρ_m (g/cm^3)	V_m (%)
13P	0.40	85.4
12P	0.33	87.8
7P	0.50	81.8
21P	0.44	84.0
20P	0.50	81.8
19P	0.58	78.7
18P	0.56	79.5
17P	0.52	81.2
16P	0.47	82.7
15P	0.57	79.2
14P	0.57	79.1
28P	0.57	79.5

The mean densities values span the range from 0.33 to 0.58 g/cm^3 . The vesicularities are calculated from the density measurements and therefore show the same pattern, although the inverse pattern; if density increases, vesicularity decreases by the same factor. Figures 6.4 and 6.5 show the mean density and the mean vesicularity plotted as a function of increasing stratigraphic height (or time in the eruption).

The density decreases with stratigraphic height (Figure 6.4) and the vesicularity increases with stratigraphic height (Figure 6.5). The lowest mean density is sample 12P at 0.33 g/cm^3 and the highest mean density is sample 19P at 0.58 g/cm^3 . The highest mean vesicularity is sample 12P at 87.8%. The lowest V_m is 19P at 78.7%. Overall, the vesicularity values are very high and in a narrow window, showing little change across the samples.

Figure 6.2 shows the mean vesicularities and ranges for each density section sampled, along with the stratigraphic column. The orange labels indicate the phases of the eruption, with the most powerful phases of the eruption being B, D, and F. All density samples are from the pumice lapilli units. Phases C, E, and G are layers containing predominately ash and fine material. Unit B is a lapilli dominated layer that sits on the snow and is thought to be the first erupted material. The ranges vary

6.2. Density and vesicularity measurements

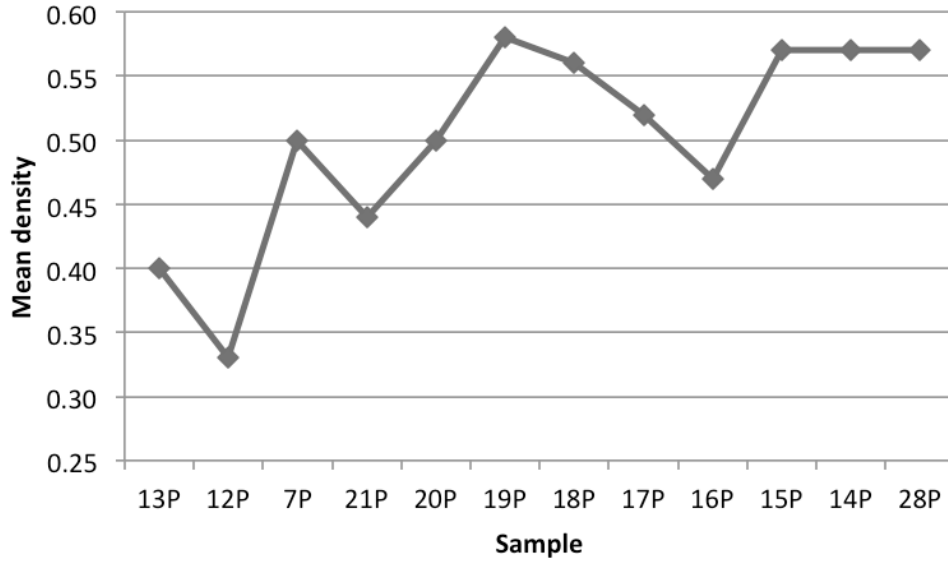


Figure 6.4: The measured mean density of each sample.

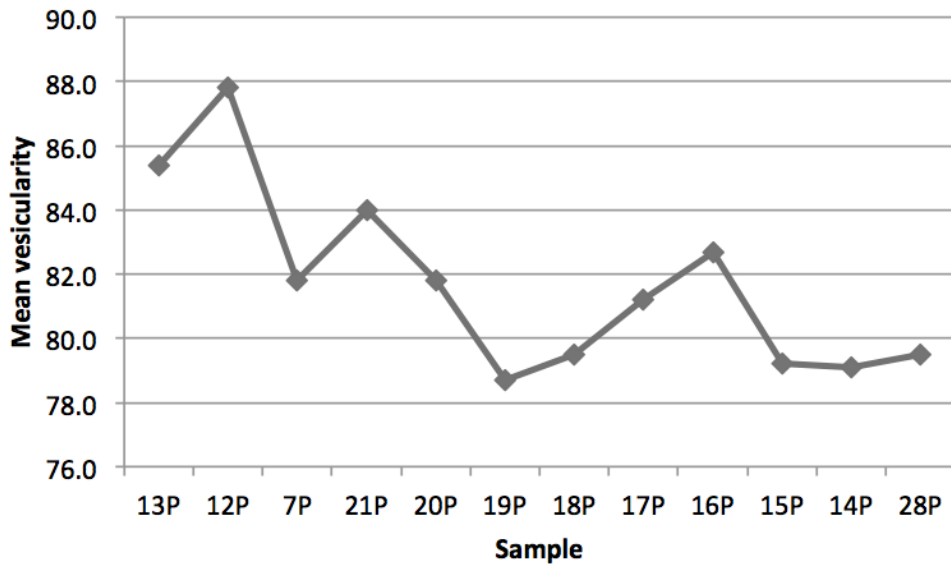


Figure 6.5: The calculated mean vesicularity of each sample.

with seemingly no pattern to stratigraphic layer content. Figures 6.6 to 6.8 show the histograms of the densities and vesicularities of each sample. The values are greatly skewed and crowd around the means, with few outliers at lower vesicularities.

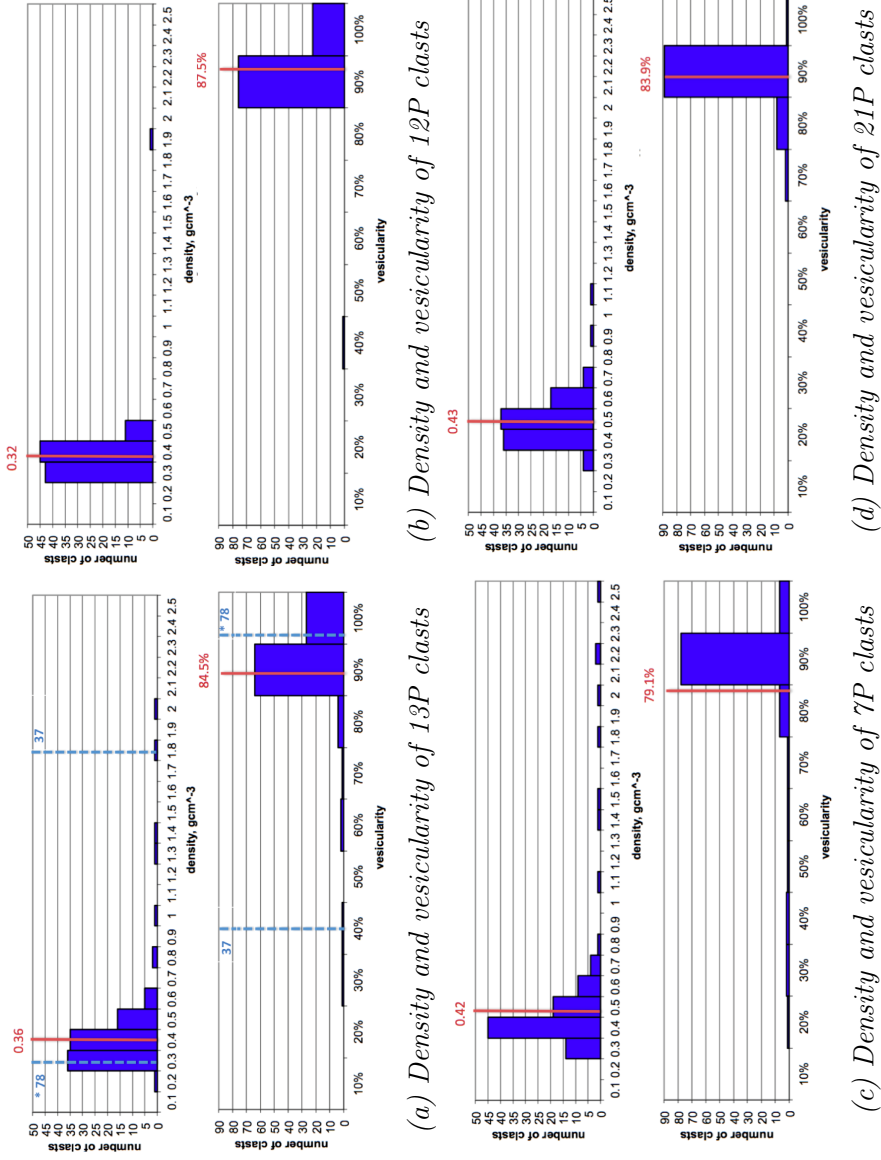


Figure 6.6: Density and vesicularity histograms with frequency of clasts. The red line represents the geometric mean values. The dotted blue lines are the selected samples, with associated clast number. The starred clast numbers represent the clasts that were imaged with SEM.

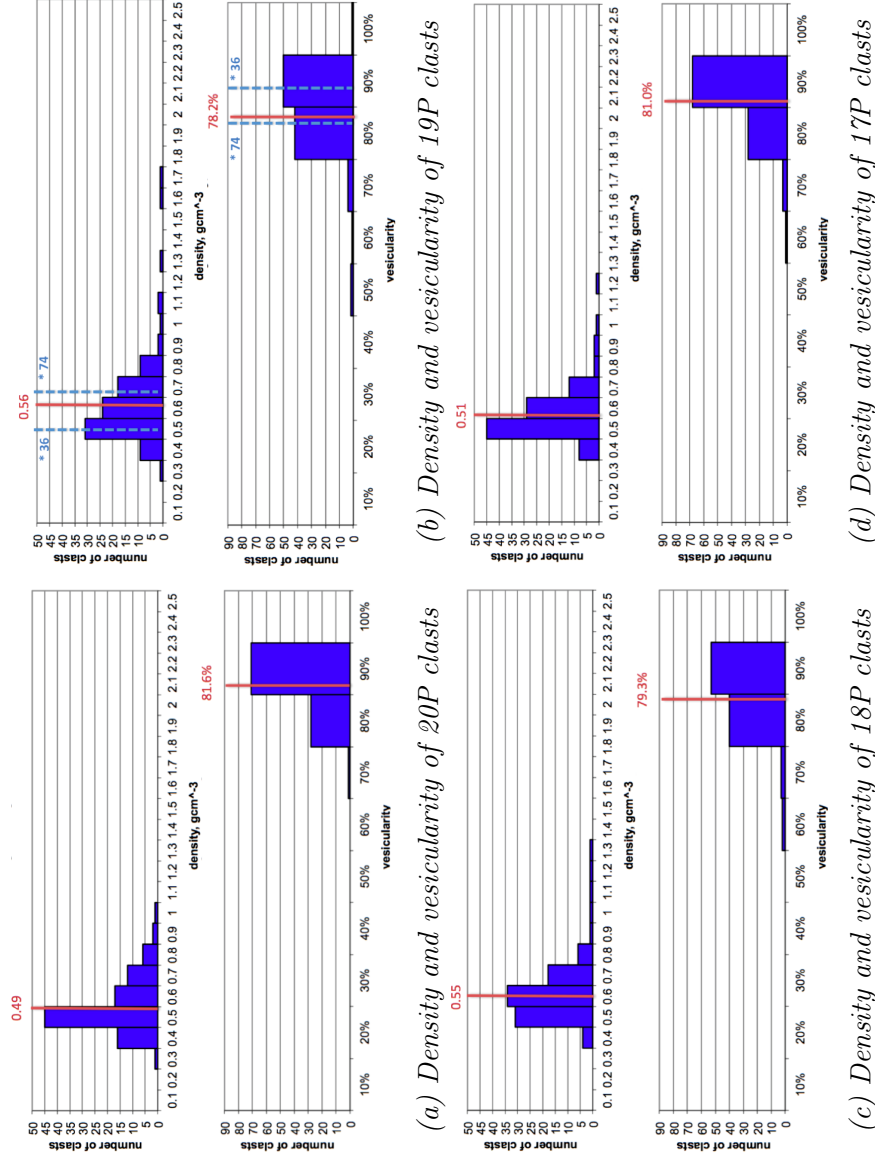


Figure 6.7: Density and vesicularity histograms with frequency of clasts. The red line represents the geometric mean values. The dotted blue lines are the selected samples, with associated clast number. The starred clast numbers represent the clasts that were imaged with SEM.

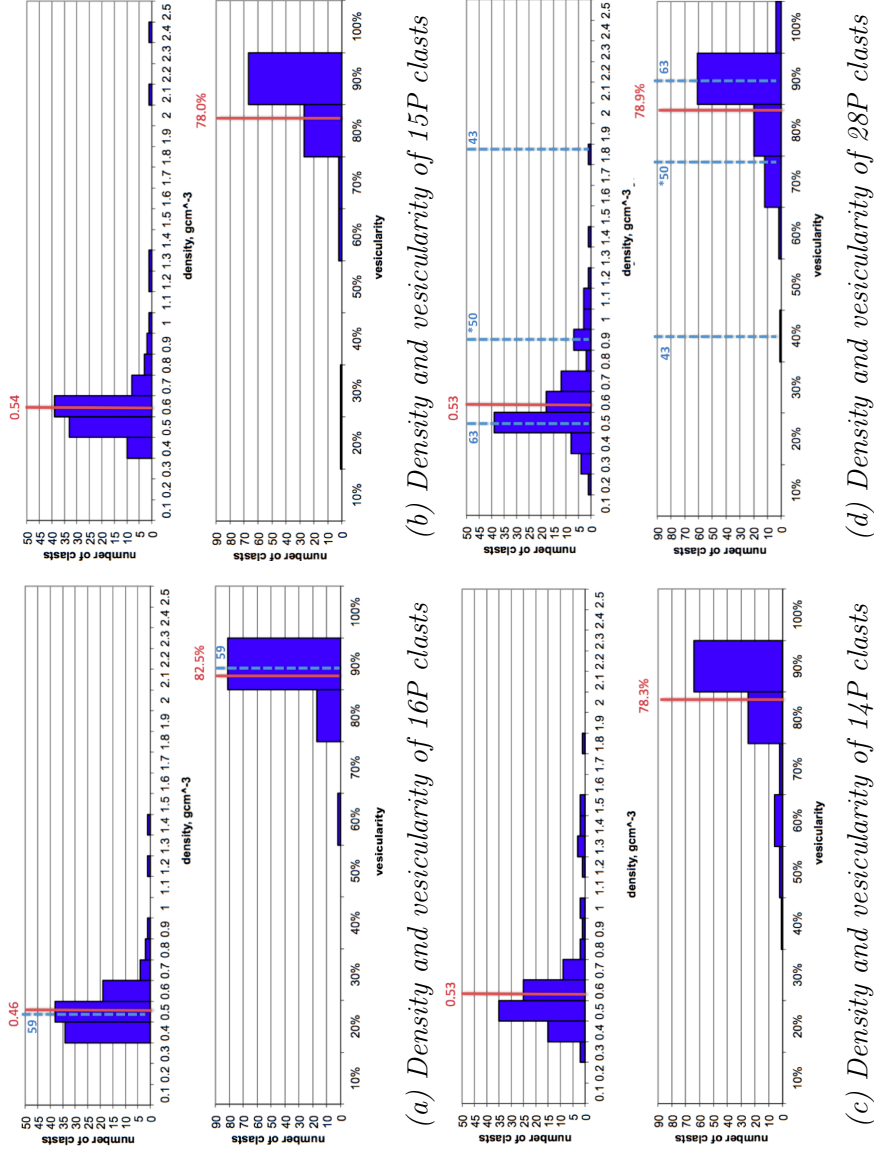


Figure 6.8: Density and vesicularity histograms with frequency of clasts. The red line represents the geometric mean values. The dotted blue lines are the selected samples, with associated clast number. The starred clast numbers represent the clasts that were imaged with SEM.

The histograms of density and vesicularity were studied and grouped according to their modes and skewness to determine any patterns of density of the clasts in various samples. Four basic groups were determined, focusing on the density distributions, as follows:

- Right-skewed distribution: 13P, 7P, 21P, 20P, 19P, 18P, 17P, 16P, 15P (Figures 6.6a, c, d, 6.7 a, b, c, d, 6.8 a, b respectively)
- Imperfect right-skewed distribution: 12P (Figure 6.6b)
- Right-skewed distribution, with a second peak: 14P, 28P (Figures 6.8c and d respectively)

The right-skewed distribution samples share some other similarities as well. The majority of the samples have a tail extending on the right, excluding 21P that has a very small tail and 20P that does not have a tail. The mode of the right-skewed samples varies between $\rho = 0.36$ and 0.56 g/cm^3 .

Sample 12P has an imperfect right-skewed distribution. There are 43% of clasts between $\rho = 0.2$ and 0.3 g/cm^3 and 45% of clasts between $\rho = 0.3$ and 0.4 g/cm^3 . The remainder of the clasts are slightly higher in density.

The right-skewed distribution, with a second peak group contains the last two in the sequence; samples 14P and 28P. Their first peaks are both between $\rho = 0.4$ and 0.5 g/cm^3 , however their second peaks differ. Sample 14P has a small second peak between $\rho = 1.2$ and 1.3 g/cm^3 and sample 28P has a small second peak between $\rho = 0.8$ and 0.9 g/cm^3 . Both samples have a few outliers at higher densities.

After reviewing the density and vesicularity patterns, eight clasts were prepared for imaging in the SEM. These eight clasts are represented as the dotted blue lines in Figures 6.6 to 6.8. Attempts were made at imaging all eight clasts and four clasts were selected to be used for the full image analysis based on the quality of their images and the time-frame available for this work. The clasts listed in Table 6.3 were the selected clasts. They were chosen to show the best representation of distributions from the samples (based on histogram analysis), for showing a range of density measurements and covering the broadest stratigraphic range from the eruption as possible. They were also selected to represent units B, D and F, the three pumice lapilli units from the deposit.

Clast 78 from sample 13P was selected because it is from the mode bin of unit B, the first phase of the eruption. Clast 36 and 74 are from unit D, representing the second pumice lapilli unit in the tephra sequence. Clast 36 is selected because it represent a mid-density range in the distribution of sample 19P. Clast 74 was selected because

Table 6.3: Clasts imaged with the SEM.

Stratigraphic Unit	Clast Number	Measured Density (g/cm ³)	Vesicularity (%)
13P	78	0.23	91.5
19P	36	0.44	83.9
19P	74	0.61	77.6
28P	50	0.85	69.0

is typical for the upper end of the tails of the right-skewed samples. While clasts like 74 are never the mode for a sample, make up 5% of the clast population in seven of the twelve samples used in this study. Clast 50 from sample 28P, which has the highest mean density of the samples. It is from unit F, the top-most pumice lapilli unit, and is similar to clast 74 as it comes from the upper end of the near-mode end of the tail. This particular clast was selected because sample 28P has the highest number of clasts with that particular density.

6.3. Image analyses

The four clasts that were imaged with the SEM (Table 6.3) each have eleven processed images. All decoalesced images can be found in the Appendix. Figure 6.9 shows examples of the decoalesced images at three magnifications, 50x, 100x and 250x, for each sample. In the images, black represents the vesicles and white, the melt.

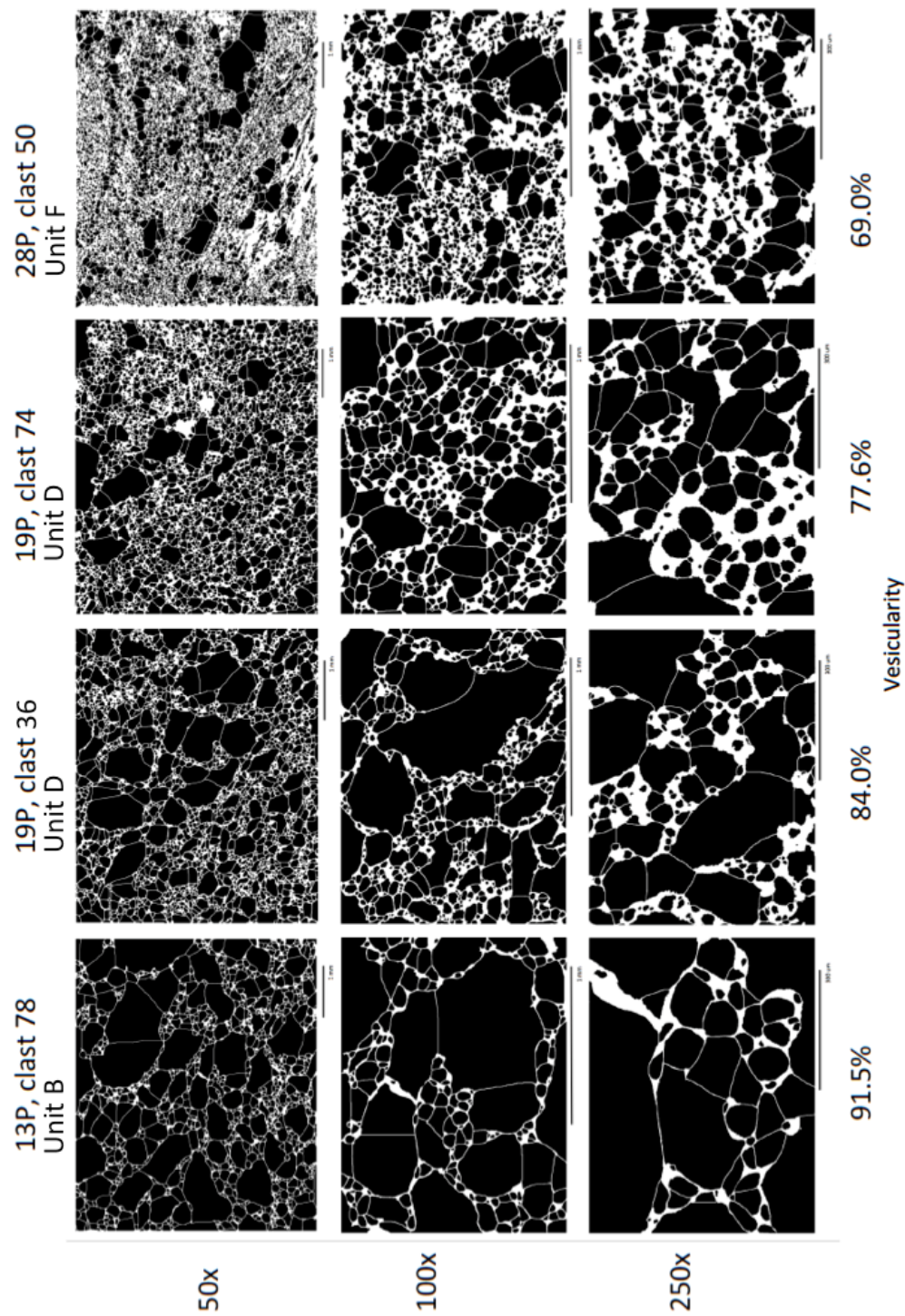


Figure 6.9: Decoalesced images at 50x, 100x and 250x magnifications. Clasts from left to right are in erupted order, clast 78 the earliest and clast 50 the latest. The calculated vesicularity of each clast is along the bottom of the image.

The clasts reached such a high level of vesicularity that the shapes of the bubbles are sub-rounded to polygonal and the textures of the clasts become convoluted in later stages. The interaction of the bubbles caused significant coalescence, to the point where decoalescing the vesicles in the images proves difficult and the vesicularity reaches very high levels. While the vesicularity does not quite reach the levels of reticulite [63], the texture of the clasts, especially clast 13P – 78, shows the vesicles shapes tending towards polygonal forms.

6.3.1. Vesicle size distribution

The vesicle size distribution, VSD, can be seen in Figure 6.10. All four clasts show a negative logarithmic slope with some differences. The range of values is very similar for all four clasts. Clast 78 has a kink in the curve. Clast 36 is smoother, however from vesicle size 1.0mm and higher the graph becomes an almost straight negative line. Clast 74 has several kinks in the curve and clast 50 has a few less prominent kinks in it.

The vesicle size data can be examined to look at the processes of the magma in terms of earlier stages of the ascent to the surface. The vesicle size distribution (VSD) is analysed to show the kinematics of nucleation and growth rate of vesicles. If the slopes are linear and negative, this indicates steady-state nucleation and growth [63] [10]. The clasts in this study have negative slopes that have multiple linear portions, attached by kinks in the line, with slope changes (Figure 6.10). Clasts 78 and 74 show no less than four different slopes and clast 36 and 50 show a slightly smoother curve. The varying slopes indicate multiples stages of nucleation and growth of vesicles, supporting the possibilities of the vesicle volume distributions (VVD). Clast 36 and 50 may indicate more continuous nucleation and growth processes. Coalescence is also a possibility, as the graphs would tend to curve upwards at the end with a larger population of larger bubbles from coalescence. It is also imaginable that nucleation, growth and coalescence could have all occurred in conjunction with each other and in pulses.

6.3.2. Vesicle volume distribution

Through processing the decoalesced images, quantitative results were produced. The vesicle volume distribution, VVD, for all four clasts are plotted in Figure 6.11. They all show multiple peaks (polymodal distribution). The graphs show good correlation between unadjusted and adjusted values. Clast 78 shows multiple peaks but has a strong bimodal undertone. Clast 36 shows is weakly bimodal and possibly trimodal. Clast 74 shows three peaks with a very large second mode. Clast 50 has the flattest

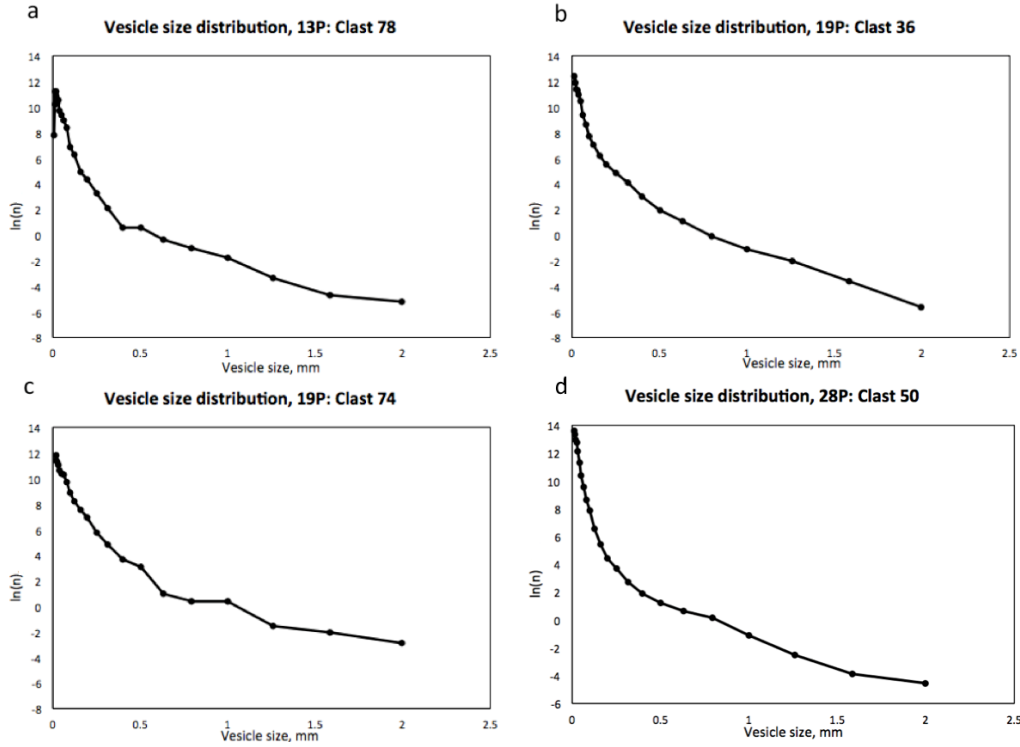


Figure 6.10: The vesicle size distribution, VSD. $\text{Ln}(n)$ (mm^{-3}) by vesicle size (mm).
a) VSD of Sample 13P: Clast 78. b) VSD of Sample 19P: Clast 36. c) VSD of Sample 19P: Clast 74. d) VSD of Sample 28P: Clast 50.

histogram and shows two distinct modes.

The major and minor peaks of the vesicle size (mm) for the VVD are demonstrated in Figure 6.11 by arrows on the major modal values and questions marks on the other minor peaks. These values were then compared across the four clasts to assess whether any of the modes are common among the samples. There is not a simple pattern to the values and thus, no straightforward interpretation exists. There are however some similarities.

The VVD of clast 13P-78 (Figure 6.11a) is polymodal with a strong undertone of bimodality. If it is representing a bimodal distribution, it could be showing two distinct peaks in bubble nucleation that are separated by time (i.e. the time it took for the bubbles to grow to a diameter of 1.3 mm, or the difference in size of the two major peaks). If it is a polymodal distribution, it could be interpreted that the main peaks are the major bubble nucleation event and superimposed on that are other nucleation events or it could be that the size intervals represent different events of coalescence.

The VVD of clast 19P-36 (Figure 6.11b) has one very distinct peak and two potential

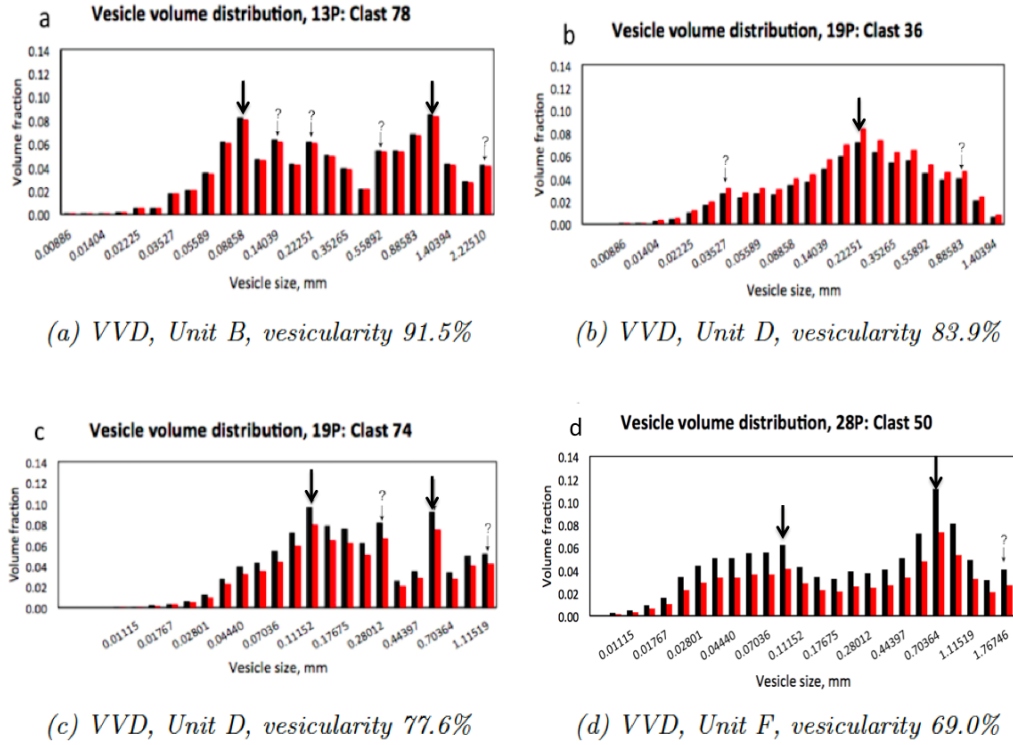


Figure 6.11: The vesicle volume distribution, VVD. Black bars represent the volume fraction. Red bars represent the adjusted volume fraction, using a multiplicative factor to adjust the volume fraction from image analysis with the density-derived volume fraction. Arrows show modal values and question marks are other minor peaks.

peaks that are weaker. It can be regarded as unimodal and therefore the distribution could be interpreted as recording one burst of nucleation or if the minor peaks are included, the distribution is polymodal and can be superimposed nucleation events or size intervals that have been affected by events of coalescence.

The VVD of clast 19P-74 (Figure 6.11c) and clast 28P-50 (Figure 6.11d) can be interpreted as bimodal or polymodal, depending on if the minor peaks are considered, in the same way as clast 13P-78. Interestingly, the main peaks are the same for these two clasts; 0.7 mm and 0.11 mm. Overall, the VVD for the clasts seem to indicate more than one nucleation event occurred to create the vesicle populations in each clast and that these units may be superimposed on each other. Alternatively, they may be showing that several coalescence events were occurring.

6.3.3. Vesicle number density

Another parameter that was calculated through image analyses is given in Table 6.4. It shows the NVm, the number density of objects in given size classes (1 to i) per unit volume adjusted for the melt (mm^{-3}).

Table 6.4: Number density of vesicles, adjusted for the melt (NVm).

Sample	Clast	NVm (cm^{-3})
13P	78	8.10×10^7
19P	36	1.06×10^8
19P	74	6.38×10^7
28P	50	1.65×10^8

Table 6.4 shows the clasts in order from the earliest erupted sample to the latest erupted sample. The trend of the four clasts for the NV value, adjusted for the melt, NVm, shows a relative increase from the earlier to the later samples, however one of the clasts from sample 19P, clast 36, continues with the increasing trend and sample 19, clast 74 does not.

The number density of vesicles, adjusted for the melt, NVm (mm^{-3}) plotted against the VG/VL are shown in Figure 6.12. The VG/VL value is the volumetric ratio of vesicles to melt or the vesicularity of the gas, VG (%) over the vesicularity of the liquid, VL (%) [108]. The plotted points represent the imaged and analysed clasts. Since the clasts used for the analysis were not specifically clasts with the average vesicularity, the average values are also plotted (circles), making the clasts plot closer together in both the NVm and VG/VL values. The NVm is assumed to be the same for the mean as for the clast in order to plot the mean points. The insert shows how different vesiculation processes can be interpreted in terms of points on the graph of vesicle-to-melt ratio and vesicle number density [108]. The points can be interpreted with the insert as growth (G), nucleation (N), collapse (Co), loss (L), coalescence (C) and combinations of these mechanisms of magma vesiculation. There is little change in bubble number density between the clasts. The earliest clast, 13P – 78, has the highest vesicularity but similar NVm, suggesting that its vesicle population had experienced longer period of growth than the others. This is in line with more mature bubble forms in clast 78. The other three clasts form a cluster and it is difficult to draw any firm conclusion about their differences although the bubble population in clasts 36 and 74 appears to have experienced more coalescence and/or growth compared to clast 50. Alternatively, the foam in clast 50 may have undergone partial collapse of the bubble population. The means show similar vesicularities and bubble number densities to each other.

Figure 6.12 shows that the clasts have similar vesicle number densities (NVm),

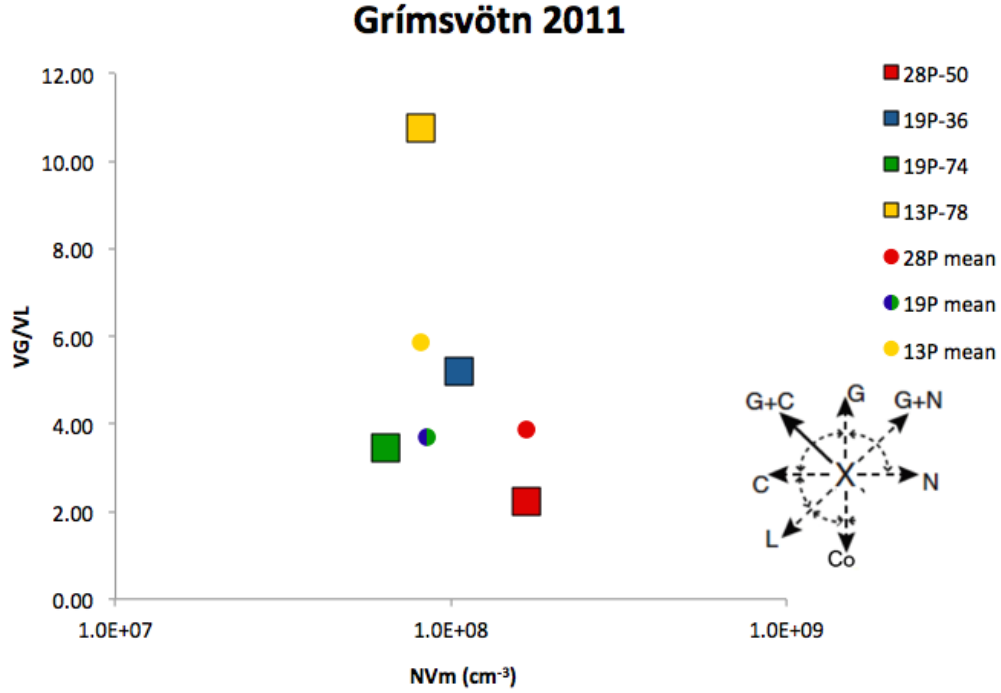


Figure 6.12: The number density of vesicles, adjusted for the melt, NV_m (mm^{-3}) plotted against vesicle gas, VG (%) over vesicle liquid, VL (%). Points plotted are the clasts that were analysed with ImageJ. The insert is taken from Stovall et al. [108]: G = growth, N = nucleation, Co = collapse, L = loss, C = coalescence.

around $1.0 \cdot 10^8 \text{ mm}^{-3}$. The clasts also show similar vesicularities, with a VG/VL value between 2.0 and 5.5, except clast 13P – 78, which has a VG/VL value of around 11.0. With the small variation in NV_m values, the clasts are interpreted to show a growth and coalescence trend. To strengthen this analysis, the textures of the images can add additional information. The later clasts show lower vesicularity but more complex and convoluted shapes, indicating the onset of bubble collapse of highly vesicular magma, possibly because of slower magma ascent. The plot of NV_m and vesicularity helps to tell a different story however and the alternative is that this texture comes from growth and coalescence. This could mean that the textures of the clasts in the 2D images may represent convoluted shapes from a high vesiculation rate [108]. It is possible that the pattern seen in the images, especially for clast 28P – 50, is showing a magma that coalesced significantly, and the thin rows of vesicles in ordered lines seem to be, at least when undecoalesced in the images, to be representing continuous cylindrical pathways where gas was moving through effectively. Together it is possible to interpret both the images and the VG/VL vs NV_m plot to show high levels of growth and coalescence. However, the values of NV_m are quite similar for the clasts and the variation should not be overanalysed. Similarly, for the textures, it is not possible to be certain of what such convoluted textures are showing. It is however, good to note that VVD and VSD result correspondingly

agree with nucleation and coalescence pulses.

To further investigate the changes in vesicle number density of the eruption, and most especially, to compare the G2011 eruption products to other dry basaltic eruptions, the vesicle number density is plotted against the time averaged mass discharge rate of the eruption (i.e. intensity) and can be seen in Figure 6.13.

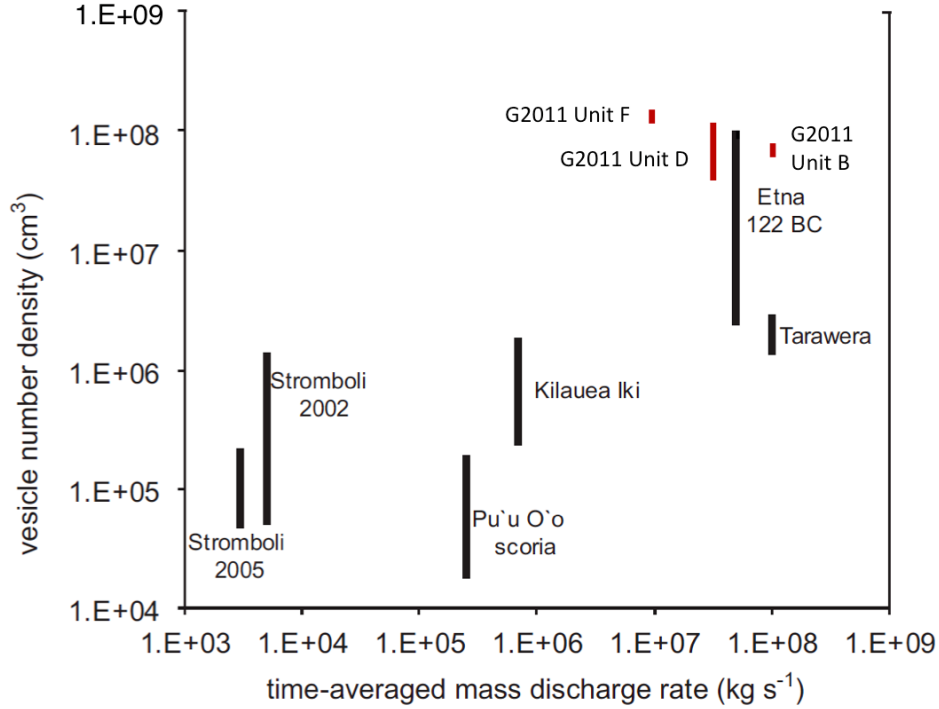


Figure 6.13: The time averaged mass discharge rate of eruptions (kg/s) versus their vesicle number density (cm^3). Grímsvötn lapilli units in red. Modified from Houghton and Gonnermann (2008) [33].

When the available information about the eruption column is analysed, and the discharge is calculated according to Mastin (2007) [109] (Table 6.1), discharge is in the range of $1 \cdot 10^{7.5} kg/s$ to $1 \cdot 10^8 kg/s$ in the first 18 hours and drops to $1 \cdot 10^7 kg/s$ at noon on 22 May. After this time the discharge seems to decrease steadily. The average discharge for the entire eruption is around $2 \cdot 10^6 kg/s$, calculated from a total volume of approximately $0.28 km^3$ divided by time. The intensity of the eruption for the lapilli phases (units B, D, and F) are plotted (Figure 6.13) and show that the intensity was close to that of Etna 122 BC and between Kilauea Iki and Tarawera [33]. The vesicle number density on the other hand, plots closest to the Etna 122 BC vesicle number densities and slightly higher than them in the case of unit F.

Kilauea Iki plots its eruptions of high fountaining, $>400m$, with some weaker in-

tervals of fountaining building localized spatter ramparts with and periods of passive degassing ([33].) Plinian eruptions are plotted, including the 1886 eruption of Tarawera and Etna 122 BC. Both have high mass discharge and vesicle number densities (between $1 \cdot 10^6$ and $1 \cdot 10^8 \text{ cm}^3$). Tarawera was observed in 1886, and a mean discharge is constrained to approximately $8.5 \cdot 10^7 \text{ kg/s}^1$, a discharge rate 3-5 orders larger than Hawaiian eruptions. A suggestion for how this increase in magnitude is possible is that abundant microlites in the Etna clasts represent that the microlites dramatically increased melt viscosity, which limited bubble growth, helping to build up enough gas overpressure for fragmentation during decompression upon ascent [33]. The microlites crystallinities of these clasts are very high compared to Hawaiian and Strombolian clasts, between 60% and 90% of the groundmass, giving enough added viscosity to the magma for basaltic eruptions to have Plinian intensity eruptions [33]. While microlites do not give a good explanation for Grímsvötn 2011 being so explosive, as there was no microlite content in the analysed clasts, Figure 6.13 does show that G2011 plots with other Plinian eruptions of similar intensities and vesicularities.

7. Discussion

While Grímsvötn eruptions would be predicted to be phreatomagmatic [15], the presence of decimetre-thick very ash-poor (or essentially ash-free) pumice lapilli units within the erupted tephra sequence along with the inferred sub-Plinian to Plinian intensity of the eruption are taken to indicate that external water played a minor role in driving the explosive activity, at least during the formation of the lapilli units.

The stratigraphy (Figures 6.2 and 6.3) indicates that the coarser phases of the eruption, phases B, D, and F, deposited lapilli units. However, the finer layers, phases C, E, and G, primarily comprised ash. This case of alternating lapilli pumice layers with ash-grade layers can be explained in two possible ways. The first is that there were changes in eruption intensity so that the lapilli layers indicate high intensity and the ash-grade layers indicate low intensity [110] [11]. To get this change in intensity, it is possible that there were changes in amount of magma supplied to the conduit between low and high intensity phases (magma discharge rate) [111]. This does fit with the observations of the plume (Figure 6.1). Calculations of discharge rates were also carried out for the lapilli layers and can be seen on Figure 6.13. The time averaged mass discharge rates were calculated to be $1 \cdot 10^8 \text{ kg/s}^1$ during unit B, $1 \cdot 10^{7.5} \text{ kg/s}^1$ during unit D, and $1 \cdot 10^7 \text{ kg/s}^1$ during unit F. The lapilli units have high mass discharge, comparable to eruptions like Etna 122 [33].

The second possibility is that the lapilli units are a product of explosive magmatic fragmentation activity and that the ash-grade layers are from quenched granulation upon magma-water interaction of highly expanded and vesiculated magma [69]. Looking further into these possibilities, while the abundance of water in the near-vent region is usually high, the ice was thin at the vent at the time of eruption. The ice had been melted significantly in the vent area during the eruption of 2004 and the eruption broke through the remaining ice in 2011 in less than 1.5 hours. The caldera lake also had low levels of water at the time due to the emptying in October 2010 from a jökulhlaup. As well, a surveillance team from IMO noted that no additional water seemed to have been melted and added to the system in the days following the eruption [14]. The evidence supports that fuel-coolant explosive interactions did not play a big role in driving the explosivity of the eruption but that external water however, may have helped to generate the ash-grade units of the deposit via quench granulation.

The vesicularity indices of the eruption are very high, between 79% and 88%, a relatively uniform value across all samples (Table 6.2 and 6.5). The vesicularity indices of other basaltic pumices are generally much lower. For example, a wet eruption, such as submarine basalts on the Reykjanes Ridge, have vesicularities of 5% at 1000 m depth and 16% at 500 m depth [112]. Houghton et al. [113] used Crater Hill, a monogenetic centre in New Zealand, to study the transitions between explosive and effusive basaltic activity. They identified phreatomagmatic clasts to have unimodal vesicularity distributions with a mean of approximately 35-40% and Hawaiian deposits to have unimodal distributions with means of 65-70%. An eruption in September 2002 at Stromboli had a unimodal vesicularity distribution with means of 70% vesicularity and a tail of 40-50% vesicularity [114]. In comparison, the main Plinian stages of the Fontana lapilli eruption in Nicaragua, produced basaltic pumice with vesicularity between 70-78% [115]. Grímsvötn vesicularities are most closely related to the basaltic Plinian stages of the Fontana lapilli eruption, endorsing the idea that G2011 was a basaltic explosive eruption of sub-Plinian to Plinian intensities.

The vesicularity indices were quite uniform and despite the range of values, most samples show a tightly grouped histogram of vesicularities (Figure 6.6 to 6.8). Dry eruptions tend to have relatively uniform assemblages [11] [12] and a dry magmatic eruption tends to produce clasts with vesicularities around 70-80%, which fits the high vesicularity seen in the clasts [11]. The Grímsvötn 2011 eruption was explosive and came from a shallow source [45], having high vesicularities. The eruption may have been explosive because it either carried enough magmatic gas initially (H_2O and S) that exsolved in an explosive manner upon rise through the conduit and subsequent eruption or through explosive interaction with external water (i.e. glacial derived water).

Sparks (1978) [12] and Houghton and Wilson (1989) [11] suggest that vesicularities of 75% to 83% will be the limit of vesicularity and the point where nucleation of new bubbles is inhibited because the bubbles interfere with each other. The magma of G2011 continued to vesiculate to very high levels, beyond these boundaries, perhaps nearly to the point of creating a magmatic foam. More recently, alternative suggestions have been put forth since a simple fragmentation threshold of approximately 75% does not explain the range in vesicularity that is usually seen in dry (i.e. magmatic) explosive eruptions [11] [116] and that magma may fragment in a brittle way when the time of deformation is shorter than the relaxation time [117]. This means that if loss of volatiles is the sole process in the melt, the relaxation time (from change in viscosity) only happens incrementally but if crystals or microlites or significant magma-water interaction occurs, viscosity can increase quickly [118]. Crystals in the G2011 clasts were $\ll 1\%$, so crystals did play a role in any processes however, magma-water interaction cannot be ruled out in quickly increasing viscosity, and thus fragmentation. It is possible that a magma-water interface occurred at the vent, when the already highly expanded magma might have come into contact

with water, arrested further vesiculation of the magma but fragmenting it at high vesicularities.

When nearing the latter part of the eruption, or the top of stratigraphy, the mean vesicularities decrease slightly for the lapilli units (Figures 6.2 and 6.3). The lower vesicularities might indicate that the vesiculation process was arrested prematurely as the magma was quenched. This could have happened by sudden exposure of the magma to colder fluids (air or water) [34] [35] [36]. The second possibility is that the magma remained in liquid form long enough to outgas and for the empty vesicles to collapse or be destroyed [65]. This would normally lead to convoluted and highly irregular bubble forms. A third way lower vesicularities might occur, is from the gas content in the batch of magma in question being lower than in other parts of the magma column [119] [120]. This would be indicated by few bubbles having formed than in batches rich in volatiles. The second possibility, of the magma having more time to outgas and have collapse textures, seems the most likely, as the imaged clast from sample 28P (lapilli unit F), has convoluted textures and is highly irregular. It is possible that the magma vesiculated to high levels (90%) first, then had more time to outgas and begin the bubble collapse process. The third option, of lower gas content creating less vesicularity is not supported, as the lower vesicularity clast, 28P-50, has a higher vesicle number density (NVm, see Figure 6.12) and a lower number of bubbles would be expected if the gas content had been decreased.

The vesicularity of magma is significantly impacted by the rise rate of bubbles within the magma, the rate of magma rising within the conduit and the discharge rate of the magma [11]. High vesicularity, such as in this eruption, is indicative of a quick rise rate and a fast eruption rate [11]. While a lower discharge would be expected to make the range of vesicularity larger, it would expand the range to lower vesicularities because of additional time in the conduit (i.e. lower rise velocity) and allow for degassing. Some of the samples do have lower vesicularity clasts, however clasts are predominantly in the higher vesicularity values, indicating that the discharge rate did not likely decrease over the course of the eruption. This cannot be the case however, as the plume data (Figure 6.1) shows that the magma discharge decreased during the eruption by more than two orders of magnitude, going from $10^8 \text{ m}^3/\text{s}$ to $10^6 \text{ m}^3/\text{s}$ in less than 24 hours. This means that either the bulk of the section (i.e. unit B to unit E) was formed in less than 24 hours, with unit F following immediately after, while unit G formed over the rest of the event or the vesicles are not telling as clear a story as publications usually hint at. This eruption demonstrates that it is likely that the vesicles' story is not as simple as it seems. For example, while the eruption would be predicted to be phreatomagmatic, the vesicles analysis appears to show that the lapilli units of G2011 were indeed magmatic.

The data presented in this thesis shows that the magma was fully or nearly fully expanded via exsolution of magmatic volatiles before it was quenched. Considering

the environment of the eruption, it is likely that external water played a role in the quenching of magma. This then must have happened when the magma was close to fully expanded from bubble growth induced degassing. As degassing of basaltic magma generally begins at 1 km depth in the conduit and reaches its peak at approximately 1 atm conditions (i.e. the surface), the implication is that the external water contacted the magma when it emerged from the vent [121]. It is at this time that the magma is nearly a foam and possibly a disintegrated foam, which is not an ideal product for fuel-coolant interactions (MFCI) because the foamy magma has high yield strength and therefore, does not form the required interface for such interactions [34] [35] [36]. It is possible that the formation of ash occurred via quenched granulation, thus creating the ash-grade layers of the deposit, units C, E, and G [69].

The major and minor peaks of the vesicle size (mm) for the VVD are demonstrated in Figure 6.11 by arrows on the major modal values and question marks on the other minor peaks and discussed in the results chapter. If one assumes that vesiculation was a near-constant process with steady nucleation of vesicles, followed by growth by expansion and some coalescence, it is possible to interpret the VVD patterns as follows. Perhaps the main peaks represent a burst of bubble nucleation where the bubble size has been modified by subsequent growth and that the lower points represent the build up and tail to the bubble burst events. It is possible also, that the minor peaks represent discrete bubble coalescence events.

The VVD of the clasts (Figure 6.11) are all bimodal or polymodal, depending on the interpretation. If bimodal, it is representing two distinct peaks in bubble nucleation that are separated by time. If it is a polymodal distribution, it could be interpreted that the main peaks are the major bubble nucleation event and superimposed on that are other nucleation events or it could be that the size intervals represent different events of coalescence. It is likely that nucleation pulses or individual events occurred, superimposed with growth and coalescence events to create the distribution of vesicles. The main or larger modes were probably governed by the nucleation events and the other features or smaller modal values, could be a result of bursts of growth or coalescence. Alternatively, they may be showing that several coalescence events were occurring. Using the image textures to distinguish between these two possibilities is difficult based on the heavy coalescence in this particular deposit however the number density of vesicles seems to be more in favour of a coalescence trend but the trend is not strong enough to be certain. It is difficult to distinguish between these possibilities, as the coalescence and manual decoalescence during the process of image analysis, can introduce a user bias by decoalescing bubbles more or less than necessary.

The vesicle size distribution (Figure 6.10) can be examined to look at the processes of the magma in terms of earlier stages of the ascent to the surface. Fitting in with the other assessments of the vesiculation history, the VSD for the four clasts

shows that there were multiple nucleation and growth events. Coalescence may also be indicated by the idea that the graph curves upward near the end. This can be supported by examining the SEM images that were not decoalesced, in which coalescence can be seen by the vesicle walls that appear to be missing where they once were. It is also imaginable that nucleation, growth and coalescence could have all occurred in conjunction, in pulses and overlapping with each other. The G2011 clast vesicle size distributions are certainly indicating a storied and multifaceted history.

The number density of vesicles per unit volume (NVm), adjusted for the melt and for all four clasts is relatively uniform (see Table 6.4). There is a slight net increase in the NVm up section, that is from the first to the last erupted pumice clast (Figure 6.12). The NVm indicates that the Grímsvötn 2011 eruption was uniform to slightly increasing in intensity with time. Looking at the observed eruption intensity (see Table 4.1), the eruption was most intense on the 21 May, the first day of the eruption, with a 20 km high plume. The intensity decreased the next day, as the plume was 10 km. On the 24 May the plume was at 5 km and the following day it had increased up to 12 km. This increase from the 24-25 May could be an indication of the start of unit F (the final lapilli unit in the sequence) and could be the increase in intensity over time that is recorded by the NVm values increasing. It is possible to interpret both the VG/VL vs NVm plot to show high levels of growth and coalescence. However, the values of NVm are quite similar for the clasts and the variations should not be overanalysed. Similarly, for the textures of the SEM images, it is not possible to be certain of what such convoluted textures that are displayed are showing. It is however, good to note that VVD and VSD result correspondingly agree with nucleation and coalescence pulses.

It should also be noted, that the pumice clasts that were selected for analyses do not represent the same location in the density distribution (i.e. are from different stages of the vesiculation process). This was worked around by also looking at the clasts in terms of the mean vesicularities of that particular unit and not overanalysing the order of the events, such as in Figure 6.12. Instead of looking at the clasts in eruptive order, it is best to consider their vesicularities and what they represent in that unit. For example, clast 13P-78 has a vesicularity of 91.5% but the mean of the sample is 84.5%. To attempt to factor in that this might represent a clast with more growth, nucleation or coalescence than the average clast at this time, the means have also been plotted and noted in most figures.

Figure 6.13 compares G2011 clasts to other dry basaltic eruptions with the vesicle number density and time averaged mass discharge rate of the eruption (i.e. intensity). The intensity was close to that of Etna 122 BC and between Kilauea Iki and Tarawera [33]. Etna 122 BC shows very high mass discharge rates and vesicle number density, which is explained by the increase in melt viscosity from microlites [33]. The clasts that were analysed in this study did not have crystal or microlite con-

tent, however Sigmarsson [58] found that some clasts have ample microlites, while others have no microlite content at all. The possibility that the G2011 had ample microlites is low considering this study did not find clasts of this nature, however it could be a point of further investigation.

In light of the lack of microlite to increase magma, other factors must be explored to explain how the G2011 was so explosive. To narrow the discussion, only primary factors that control eruption dynamics will be considered: magma supply rate, conduit geometry, degassing magmatic volatile properties, fluid mechanics of magma ascent and magma fragmentation mechanisms [33]. Magma supply rate and the basaltic nature seem to be approximately equivalent to that of other Plinian eruptions (Figure 6.13). The conduit geometry cannot be precluded from affecting the eruption intensity, however it is outside the scope of this discussion. Degassing and fragmentation mechanisms are likely the main factors in controlling the Grímsvötn eruption. This could mean that the amount of volatiles, the nucleation speed and quantity upon eruption, as well as the fragmentation factors control the intensity of the G2011 eruption. In light of the previous discussion in this chapter, this fits suitably with the previous notions that the magma was fully or nearly fully expanded via exsolution of magmatic volatiles before it was quenched and that the quenching likely happened via dry magmatic fragmentation. Although fragmentation driven by magmatic-water interactions, cannot be ruled out for the formation of the lapilli units, it is an highly unlikely mode of fragmentation because of the difficulty for a magma with such high vesicularity (i.e. nearly foam) to support MFCI because of the foam's high yield strength [34] [35] [36]. The disintegration of such a highly vesicular magma would lead to granulation, and thus leaves an explanation for the ash-grade units [69].

8. Conclusions

Grímsvötn, the most frequently erupting volcano in Iceland, erupted for the second time in the 21st century in 2011. This explosive eruption was more powerful than its predecessor in 2004, producing a 20 km-high ash plume and widespread tephra fall [14]. The Grímsvötn 2011 eruption was a sustained, explosive basaltic eruption of sub-Plinian to Plinian intensity. We set out to answer the following questions:

- What are the density and vesicularity of the pumice lapilli clasts from this eruption and how do they change over the course of the eruption?
- What is the vesicle size distribution of the pumice lapilli clasts and how does it change over the course of the eruption?
- What can these values tell us about the eruption style, especially fragmentation and degassing of magma that occurred during this eruption?

To look at the density and vesicularity of the clasts from this eruption, we first examined the tephra sequence. The tephra sequence of the Grímsvötn 2011 eruption has alternating units of basaltic pumice lapilli and ash-grade units. This study has shown that these units represent alternating eruption intensities or explosive magmatic activity producing lapilli units and quenched granulation producing ash-grade units. While the observations of the eruption plume alternate in intensity, it does not show a good correlation with the number of units or correlation with discharge rates. The second possibility is more likely, due to the likelihood of water playing some role in this eruption, which began as subglacial. The evidence supports the idea that while fuel-coolant explosive interactions did not drive the explosive activity of the eruption, it may have caused quenched granulation of highly expanded and vesiculated magma, creating the ash-grade layers [69]

The mean vesicularity of the 12 measured samples, representing a transect through the tephra fall deposit, are extremely high, between 78.7% and 87.8% and relatively uniform (see Figures 6.2 and 6.3). These values for clast vesicularities indicate that the rising magma column was effectively degassed and highly expanded upon eruption. Sparks (1978) [12] and Houghton and Wilson (1989) [11] suggest that vesicularities of 75% to 83% will be the limit of vesicularity and the point where

nucleation is inhibited because the bubbles interfere with each other, however this eruption shows that a basaltic explosive eruption can have systematically higher vesicularity values than this theoretical value. This raises some interesting questions about its applicability to all explosive eruptions and demonstrates that reality is more complex than understood. The eruption may have been explosive because it either carried enough magmatic gas initially (H_2O and S) that exsolved in an explosive manner upon rise through the conduit and subsequent eruption, or through explosive interaction with external water (i.e. glacial-derived water). A dry magmatic eruption tends to produce clasts with vesicularities around 70-80%, which fits the high vesicularities seen in the clasts and thus, it does not support the idea that external water interaction drove the explosivity of the lapilli units [11]. The glacier thickness at the time of eruption was thin due to the 2004 Grímsvötn eruption melting much of the glacier near the vent, and therefore, the implication is that the relative abundance of the pumice lapilli units is a strong indicator that external water did not interact with the bulk of the magma until it had reached full expansion and subsequent fragmentation via exsolution of magmatic gases.

The vesicle size distribution plots for the four imaged clasts show bimodal or polymodal distributions, indicating that there were likely several pulses of nucleation and growth. The vesicle volume distribution for the clasts seem to indicate more than one nucleation event occurred to create the vesicle populations and that these units may be superimposed on each other, or they may be showing that several coalescence events were occurring. The vesicle number density shows that the analysed clasts have similar vesicle number densities (NVm), around $1.0 \cdot 10^8 \text{ mm}^{-3}$ and similar mean vesicularities, with a VG/VL value between 2.0 and 5.5. With the small variation in NVm values, the clasts may also be interpreted to show a growth and coalescence trend. Using the image textures it may be possible to distinguish between these possibilities. The textures of the vesicles, as seen in the SEM images (Figure 6.9), shows high vesicularity, with significant coalescence of bubbles and thin walls. The form of the bubbles is generally sub-round and separated by thin walls. These foamy clasts also have smaller domains where the bubbles tend more toward polygonal form, and collapse structures are not observed. The bubble pattern shows that bubble coalescence was an important process during vesiculation. This data shows that the G2011 clasts are indicating an elaborate history, likely with superimposed events of nucleation, growth and coalescence.

When looking at the intensity of the eruption and comparing the vesicularities and intensities to other studied eruptions, G2011 is most similar to the basaltic Plinian eruption of Etna 122 BC [33]. While the intensity of the Etna eruptions are explained by microlite content increasing the viscosity of the magma, G2011 clasts do not have as high of a microlite content. The volatile content, namely the magma that was fully or nearly expanded from exsolution of magmatic volatiles before quenching and fragmentation, is likely what drove the explosive activity and controlled the eruption intensity during the Grímsvötn 2011 within-glacier event. However, intensity-passive

disintegration of foamy magma may explain the presence of the ash-grade units [69]. This means that the explosive activity and the intensity of the eruption were mainly driven by exsolution and expansion of magmatic gases and implies magmatic or “dry” explosive phases of the eruption occurred in what is considered a “wet” environment. Since grain-size analyses and vesicle size distributions of the ash-grade layers were out of the scope of this project, it is tough say without some degree of uncertainty, what the origin of the ash-grade layers is. However, there are at least two possibilities to explain their formation.

The first possibility is that the ash-grade layers could represent magma that underwent explosive fuel-coolant interaction and erupted as a consequence of this interaction, superimposed on the magmatic gas exsolution and expansion that was already occurring. This would suggest that the explosive phases that produced the ash-grade units should be more intense than those producing the lapilli units, since the magmatic gases and magma-water interactions are both adding to the intensity in the case of the ash-grade units. In this scenario, this would also imply that external water would need to have come into contact with the magma before its full expansion and disintegration had time to occur, at a shallow depth of >100 m depth, but less than <1 km [121].

The second possibility is that the ash-grade layers could represent magma that underwent the same processes as the pumice layers (i.e. full expansion and magmatic disintegration to lapilli pumice) before external water interaction occurred. The external water would interact with gas and foamy lapilli size particles temperature instead of a batch of melt. This would mean that the conditions for having an effective external magma-water interface to drive an explosive magma-water type interaction are not favourable. The magmatic disintegration, which in this case drives the explosive intensity of the erupted mixture, has already happened when the external water comes into contact with the magma. The external water would have done nothing more than quench the foamy lapilli sized particles, forming hydrofractures across the already solidified and thin bubble walls. The consequence is disintegration of the pumice lapilli into ash-sized grains. There are then two sub-scenarios; one that would promote the notion that the pumice lapilli and ash-grade units represent distinct and separate phases, meaning that the eruption changed between “dry” and “wet” eruption conditions over six eruption phases, or one that promotes a continuous “dry” (magmatic) eruption where the external water only manages to interact with the periphery of the erupting mixture and generated the inter-dispersed ash-grade units. The latter scenario requires time difference in the deposition of the pumice lapilli and the ash-grade units, in which premature deposition of the ash would have to be delayed. This can be explained by the process of aggregation requiring some time to develop to its maximum capacity (i.e. for the plume to reach or generate the right conditions for ash aggregation). This scenario implies pairing of the pumice lapilli and ash-grade units and thus would indicate that the eruption had three main phases.

Conclusions

While we cannot differentiate between the scenarios listed above because we have not undertaken all the observations and measurements required, this could be a point of future research. Especially for the ash-grade units, where we do not have adequate information about the exact grain size, further work could be done. The vesicularity of the ash grains, their morphology and form of the bubbles they may contain could be studied and compared to the pumice lapilli results. Also, the ash-grade units could be examined for pumice lapilli clasts of a similar nature to the lapilli units. Also, for the future, a study could be carried out using both clasts representing the mean and the extreme populations for completeness, however the use of non-mean clasts in this study, does not appear to change the data and nor the conclusions, dramatically. Additionally, a study of the volatile contents of lapilli versus ash would be useful. If the ash formed by explosive magma-water interaction, a range of the degassed groundmass glass sulphur values is expected [121]. If the ash formed by full expansion, magmatic disintegration to lapilli pumice and then further external water interaction occurred, degassed sulphur values are expected to be identical to that obtained from the pumice lapilli and across the full grain population.

References

- [1] H. Wei, R. S. J. Sparks, R. Liu, Q. Fan, Y. Wang, H. Hong, H. Zhang, H. Chen, C. Jiang, J. Dong, and others, “Three active volcanoes in China and their hazards,” *Journal of Asian Earth Sciences*, vol. 21, no. 5, pp. 515–526, 2003. [Online]. Available: <http://www.sciencedirect.com/science/article/pii/S1367912002000810>
- [2] J.-C. Thouret, F. Lavigne, K. Kelfoun, and S. Bronto, “Toward a revised hazard assessment at Merapi volcano, Central Java,” *Journal of Volcanology and Geothermal Research*, vol. 100, no. 1, pp. 479–502, 2000. [Online]. Available: <http://www.sciencedirect.com/science/article/pii/S0377027300001529>
- [3] A. Robock, “Volcanic eruptions and climate,” *Reviews of Geophysics*, vol. 38, no. 2, pp. 191–219, 2000. [Online]. Available: <http://onlinelibrary.wiley.com/doi/10.1029/1998RG000054/full>
- [4] T. Thordarson, S. Self, D. J. Miller, G. Larsen, and E. G. Vilmundardóttir, “Sulphur release from flood lava eruptions in the Veidivötn, Grímsvötn and Katla volcanic systems, Iceland,” *Geological Society, London, Special Publications*, vol. 213, no. 1, pp. 103–121, 2003. [Online]. Available: <http://sp.lyellcollection.org/content/213/1/103.short>
- [5] T. J. Casadevall, *Volcanic ash and aviation safety: proceedings of the first international symposium on volcanic ash and aviation safety*. DIANE Publishing, 1994, vol. 2047. [Online]. Available: https://www.google.com/books?hl=en&lr=&id=pKY_VLqMTgsC&oi=fnd&pg=PR3&dq=ash+plume+aircraft+volcano&ots=Nd6eOHMaCM&sig=Vkr0d13dG0YyzHdpb29s-Z0Lk2g
- [6] M. T. Gudmundsson, R. Pedersen, K. Vogfjörð, B. Thorbjarnardóttir, S. Jakobsdóttir, and M. J. Roberts, “Eruptions of Eyjafjallajökull Volcano, Iceland,” *Eos, Transactions American Geophysical Union*, vol. 91, no. 21, pp. 190–191, 2010. [Online]. Available: <http://onlinelibrary.wiley.com/doi/10.1029/2010EO210002/abstract>

REFERENCES

- [7] T. Thordarson and S. Self, “The laki (skaftar fires) and grimsvotn eruptions in 1783–1785,” *Bulletin of Volcanology*, vol. 55, no. 4, pp. 233–263, 1993. [Online]. Available: <http://link.springer.com/article/10.1007/BF00624353>
- [8] S. Hreinsdottir, F. Sigmundsson, M. J. Roberts, H. Bjornsson, R. Grapenthin, P. Arason, T. arnaddottir, J. Holmjarn, H. Geirsson, R. A. Bennett, and others, “Volcanic plume height correlated with magma-pressure change at grimsvotn volcano, iceland,” *Nature Geoscience*, vol. 7, no. 3, pp. 214–218, 2014. [Online]. Available: <http://www.nature.com/articles/doi:10.1038%2Fngeo2044>
- [9] G. Vilardo, F. Sansivero, and G. Chiodini, “Long-term TIR imagery processing for spatiotemporal monitoring of surface thermal features in volcanic environment: a case study in the Campi Flegrei (Southern Italy).” *Journal of Geophysical Research: Solid Earth*, 2015. [Online]. Available: <http://onlinelibrary.wiley.com/doi/10.1002/2014JB011497/abstract>
- [10] T. Shea, B. F. Houghton, L. Gurioli, K. V. Cashman, J. E. Hammer, and B. J. Hobden, “Textural studies of vesicles in volcanic rocks: an integrated methodology,” *Journal of Volcanology and Geothermal Research*, vol. 190, no. 3, pp. 271–289, 2010. [Online]. Available: <http://www.sciencedirect.com/science/article/pii/S0377027309004624>
- [11] B. F. Houghton and C. J. N. Wilson, “A vesicularity index for pyroclastic deposits,” *Bulletin of volcanology*, vol. 51, no. 6, pp. 451–462, 1989. [Online]. Available: <http://link.springer.com/article/10.1007/BF01078811>
- [12] R. S. J. Sparks, “The dynamics of bubble formation and growth in magmas: a review and analysis,” *Journal of Volcanology and Geothermal Research*, vol. 3, no. 1, pp. 1–37, 1978.
- [13] N. Thomas, C. Jaupart, and S. Vergnolle, “On the vesicularity of pumice,” *Journal of Geophysical Research: Solid Earth (1978–2012)*, vol. 99, pp. 15 633–15 644, 1994. [Online]. Available: <http://onlinelibrary.wiley.com/doi/10.1029/94JB00650/full>
- [14] I. M. O. (IMO), “Update on volcanic activity in grimsvotn: Status reports, photos and facts,” *Icelandic Meteorological Office website*, 2011. [Online]. Available: <http://en.vedur.is/earthquakes-and-volcanism/articles/nr/2180>
- [15] T. C. Jude-Eton, T. Thordarson, M. T. Gudmundsson, and B. Oddsson, “Dynamics, stratigraphy and proximal dispersal of supraglacial tephra during the ice-confined 2004 eruption at Grimsvotn Volcano, Iceland,” *Bulletin of volcanology*, vol. 74, no. 5, pp. 1057–1082, 2012. [Online]. Available: <http://link.springer.com/article/10.1007/s00445-012-0583-3>

- [16] S. Thorarinsson, “Some new aspects of the Grímsvötn problem,” *Journal of Glaciology*, vol. 2, pp. 267–275, 1953. [Online]. Available: <http://adsabs.harvard.edu/abs/1953JGlac...2..267T>
- [17] M. T. Gudmundsson, F. Sigmundsson, and H. Björnsson, “Ice–volcano interaction of the 1996 Gjálp subglacial eruption, Vatnajökull, Iceland,” *Nature*, vol. 389, no. 6654, pp. 954–957, 1997. [Online]. Available: <http://www.nature.com/articles/doi:10.1038%2F40122>
- [18] I. T. Bjarnason, “An iceland hotspot saga,” *Jokull*, vol. 58, pp. 3–16, 2008. [Online]. Available: http://www.mantleplumes.org/WebDocuments/hotspot_saga_fin.pdf
- [19] S. P. Jakobsson and M. T. Gudmundsson, “Subglacial and intraglacial volcanic formations in iceland,” *Jokull*, vol. 58, pp. 179–196, 2008. [Online]. Available: http://www.hi.is/~mtg/pdf/2008Jokull58_SPJ-MTG_subglac.pdf
- [20] L. A. Lawver and R. D. Müller, “Iceland hotspot track,” *Geology*, vol. 22, no. 4, pp. 311–314, 1994. [Online]. Available: <http://geology.gsapubs.org/content/22/4/311.short>
- [21] A. E. Gripp and R. G. Gordon, “Young tracks of hotspots and current plate velocities,” *Geophysical Journal International*, vol. 150, no. 2, pp. 321–361, 2002. [Online]. Available: <http://gji.oxfordjournals.org/content/150/2/321.short>
- [22] A. W. Hofmann and W. M. White, “Mantle plumes from ancient oceanic crust,” *Earth and Planetary Science Letters*, vol. 57, no. 2, pp. 421–436, 1982. [Online]. Available: <http://www.sciencedirect.com/science/article/pii/0012821X82901613>
- [23] M. A. Richards, R. A. Duncan, and V. E. Courtillot, “Flood basalts and hot-spot tracks: plume heads and tails,” *Science*, vol. 246, no. 4926, pp. 103–107, 1989. [Online]. Available: <http://www.sciencemag.org/content/246/4926/103.short>
- [24] M. J. Fouch, “The Yellowstone Hotspot: Plume or Not?” *Geology*, vol. 40, no. 5, pp. 479–480, 2012. [Online]. Available: <http://geology.gsapubs.org/content/40/5/479.short>
- [25] R. S. White, D. McKenzie, and R. K. O’Nions, “Oceanic crustal thickness from seismic measurements and rare earth element inversions,” *Journal of Geophysical Research: Solid Earth (1978–2012)*, vol. 97, no. B13, pp. 19 683–19 715, 1992. [Online]. Available: <http://onlinelibrary.wiley.com/doi/>

REFERENCES

10.1029/92JB01749/full

- [26] F. A. Darbyshire, R. S. White, and K. F. Priestley, “Structure of the crust and uppermost mantle of iceland from a combined seismic and gravity study,” *Earth and Planetary Science Letters*, vol. 181, no. 3, pp. 409–428, 2000. [Online]. Available: <http://www.sciencedirect.com/science/article/pii/S0012821X00002065>
- [27] P. Einarsson, “Plate boundaries, rifts and transforms in iceland,” *Jokull*, vol. 58, no. 12, pp. 35–58, 2008. [Online]. Available: http://jardvis.hi.is/sites/jardvis.hi.is/files/Pdf_skjol/Jokull58_pdf/jokull58-einarsson.pdf
- [28] H. Bjornsson and F. Palsson, “Icelandic glaciers,” *Jokull*, vol. 58, pp. 365–386, 2008.
- [29] T. Thordarson and a. Hoskuldsson, “Postglacial volcanism in iceland,” *Jokull*, vol. 58, pp. 197–228, 2008. [Online]. Available: <http://www.geo.mtu.edu/~raman/papers2/Thordarson%20and%20Hoskuldsson%202008%20Postglacial%20volcanism.pdf>
- [30] T. Thordarson and G. Larsen, “Volcanism in iceland in historical time: Volcano types, eruption styles and eruptive history,” *Journal of Geodynamics*, vol. 43, no. 1, pp. 118–152, 2007. [Online]. Available: <http://www.sciencedirect.com/science/article/pii/S0264370706000652>
- [31] T. Thordarson and A. Hoskuldsson, *Iceland*. Harpenden: Dunedin Academic Press Ltd., Jan. 2002.
- [32] S. P. Jakobsson and M. T. Gudmundsson, “The three igneous rock series of iceland,” *Jokull*, vol. 58, pp. 179–196, 2008.
- [33] B. F. Houghton and H. M. Gonnermann, “Basaltic explosive volcanism: constraints from deposits and models,” *Chemie der Erde-Geochemistry*, vol. 68, no. 2, pp. 117–140, 2008. [Online]. Available: <http://www.sciencedirect.com/science/article/pii/S0009281908000159>
- [34] K. H. Wohletz, “Mechanisms of hydrovolcanic pyroclast formation: grain-size, scanning electron microscopy, and experimental studies,” *Journal of Volcanology and Geothermal Research*, vol. 17, no. 1, pp. 31–63, 1983. [Online]. Available: <http://www.sciencedirect.com/science/article/pii/0377027383900616>
- [35] —, “Explosive magma-water interactions: Thermodynamics, explosion mechanisms, and field studies,” *Bulletin of Volcanology*, vol. 48, no. 5, pp.

- 245–264, 1986. [Online]. Available: <http://link.springer.com/article/10.1007/BF01081754>
- [36] R. Buettner and B. Zimanowski, “Physics of thermohydraulic explosions,” *Physical Review E*, vol. 57, no. 5, p. 5726, 1998. [Online]. Available: <http://journals.aps.org/pre/abstract/10.1103/PhysRevE.57.5726>
- [37] H. Mattsson and A. Hoskuldsson, “Geology of the Heimaey volcanic centre, south Iceland: early evolution of a central volcano in a propagating rift?” *Journal of volcanology and geothermal research*, vol. 127, no. 1, pp. 55–71, 2003. [Online]. Available: <http://www.sciencedirect.com/science/article/pii/S0377027303001781>
- [38] R. S. J. Sparks, L. Wilson, and H. Sigurdsson, “The pyroclastic deposits of the 1875 eruption of Askja, Iceland,” *Philosophical Transactions of the Royal Society of London. Series A, Mathematical and Physical Sciences*, vol. 299, no. 1447, pp. 241–273, 1981. [Online]. Available: <http://classic.rsta.royalsocietypublishing.org/content/299/1447/241.abstract>
- [39] R. J. Carey, B. F. Houghton, and T. Thordarson, “Tephra dispersal and eruption dynamics of wet and dry phases of the 1875 eruption of Askja Volcano, Iceland,” *Bulletin of Volcanology*, vol. 72, no. 3, pp. 259–278, 2010. [Online]. Available: <http://link.springer.com/article/10.1007/s00445-009-0317-3>
- [40] B. P. Kokelaar and G. P. Durant, “The submarine eruption and erosion of Surtla (Surtsey), Iceland,” *Journal of Volcanology and Geothermal Research*, vol. 19, no. 3, pp. 239–246, 1983. [Online]. Available: <http://www.sciencedirect.com/science/article/pii/0377027383901129>
- [41] M. T. Gudmundsson and T. Hognadottir, “Volcanic systems and calderas in the vatnajokull region, central iceland: Constraints on crustal structure from gravity data,” *Journal of Geodynamics*, vol. 43, no. 1, pp. 153–169, 2007. [Online]. Available: <http://www.sciencedirect.com/science/article/pii/S0264370706000664>
- [42] C. J. Wolfe, I. T. Bjarnason, J. C. VanDecar, and S. C. Solomon, “Seismic structure of the Iceland mantle plume,” *Nature*, vol. 385, no. 6613, pp. 245–247, 1997. [Online]. Available: <http://www.higp.hawaii.edu/~cecily/385245a0.pdf>
- [43] B. A. oladottir, “Holocene eruption history and magmatic evolution of the sub-glacial vatnajokull volcanoes, grimsvotn, bardarbunga and kverkfjoll, iceland,” 2009.
- [44] M. T. Gudmundsson, F. Sigmundsson, H. Bjornsson, and T. Hognadottir,

REFERENCES

- “The 1996 eruption at gjalp, vatnajokull ice cap, iceland: efficiency of heat transfer, ice deformation and subglacial water pressure,” *Bulletin of Volcanology*, vol. 66, no. 1, pp. 46–65, 2004. [Online]. Available: <http://link.springer.com/article/10.1007/s00445-003-0295-9>
- [45] M. T. Gudmundsson and J. Milsom, “Gravity and magnetic studies of the subglacial grimsvotn volcano, iceland: implications for crustal and thermal structure,” *Journal of Geophysical Research: Solid Earth (1978–2012)*, vol. 102, pp. 7691–7704, 1997. [Online]. Available: <http://onlinelibrary.wiley.com/doi/10.1029/96JB03808/full>
- [46] H. Björnsson, S. Björnsson, and T. Sigurgeirsson, “Penetration of water into hot rock boundaries of magma at Grímsvötn,” 1982. [Online]. Available: <http://www.nature.com/articles/295580a0>
- [47] T. C. Jude-Eton, “Eruption dynamics within an emergent subglacial setting: a case study of the 2004 eruption of grímsvötn volcano, iceland,” 2013.
- [48] M. T. Gudmundsson and H. Björnsson, “Eruptions in Grimsvotn, Vatnajokull, Iceland, 1934-1991,” *Jokull*, vol. 41, pp. 21–45, 1991. [Online]. Available: <http://jokulljournal.is/40-49/J41p21.pdf>
- [49] C. Caseldine, A. Russell, J. Hardardóttir, and O. Knudsen, *Iceland - Modern Processes and Past Environments*. Elsevier, Apr. 2005.
- [50] R. Alfaro, B. Brandsdóttir, D. P. Rowlands, R. S. White, and M. T. Gudmundsson, “Structure of the Grímsvötn central volcano under the Vatnajökull icecap, Iceland,” *Geophysical Journal International*, vol. 168, no. 2, pp. 863–876, 2007. [Online]. Available: <http://gji.oxfordjournals.org/content/168/2/863.short>
- [51] H. Björnsson, “Subglacial lakes and jokulhlaups in iceland,” *Global and Planetary Change*, vol. 35, no. 3, pp. 255–271, 2003. [Online]. Available: <http://www.sciencedirect.com/science/article/pii/S0921818102001303>
- [52] E. Sturkell, P. Einarsson, F. Sigmundsson, H. Geirsson, H. Olafsson, R. Pedersen, E. de Zeeuw-van Dalfsen, A. T. Linde, S. I. Sacks, and R. Stefansson, “Volcano geodesy and magma dynamics in iceland,” *Journal of Volcanology and Geothermal Research*, vol. 150, no. 1, pp. 14–34, 2006. [Online]. Available: <http://www.sciencedirect.com/science/article/pii/S0377027305002520>
- [53] E. C. Sturkell, F. Sigmundsson, P. Einarsson, S. Hreinsdóttir, T. Villemín, H. Geirsson, B. G. Ofeigsson, F. Jouanne, H. Björnsson, G. B. Gudmundsson,

- and others, “Deformation cycle of the grimsvotn sub-glacial volcano, iceland, measured by GPS,” in *AGU Fall Meeting Abstracts*, vol. 1, 2011, p. 04. [Online]. Available: <http://adsabs.harvard.edu/abs/2011AGUFM.V31H..04S>
- [54] E. Sturkell, P. Einarsson, F. Sigmundsson, S. Hreinsdóttir, and H. Geirsson, “Deformation of Grímsvötn volcano, Iceland: 1998 eruption and subsequent inflation,” *Geophysical research letters*, vol. 30, no. 4, 2003. [Online]. Available: <http://onlinelibrary.wiley.com/doi/10.1029/2002GL016460/full>
- [55] S. S. Jakobsdóttir, “Seismicity in Iceland: 1994–2007,” *Jökull*, vol. 58, pp. 75–100, 2008. [Online]. Available: http://earthice.hi.is/sites/jardvis.hi.is/files/Pdf_skjol/Jokull58_pdf/jokull58-jakobsdottir.pdf
- [56] S. Hreinsdottir, “Grimsfjall - gps time series (grim and gfum),” *Institute of Earth Sciences, University of Iceland and Icelandic Meteorological Office (IMO)*, 2013. [Online]. Available: <http://strokkur.raunvis.hi.is/~sigrun/GFUM.html>
- [57] M. T. Gudmundsson, A. Hoskuldsson, G. Larsen, T. Thordarson, B. A. Oladottir, B. Oddsson, J. Gudnason, T. Hognadottir, J. A. Stevenson, B. F. Houghton, and others, “The may 2011 eruption of grimsvotn,” *EGU General Assembly Conference Abstracts*, vol. 14, 2012. [Online]. Available: <http://adsabs.harvard.edu/abs/2012EGUGA..14I2119G>
- [58] O. Sigmarsson, B. Haddadi, S. Carn, S. Moune, J. Gudnason, K. Yang, and L. Clarisse, “The sulfur budget of the 2011 Grímsvötn eruption, Iceland,” *Geophysical Research Letters*, vol. 40, no. 23, pp. 6095–6100, 2013. [Online]. Available: <http://onlinelibrary.wiley.com/doi/10.1002/2013GL057760/full>
- [59] P. J. Wallace, “Volcanic SO₂ emissions and the abundance and distribution of exsolved gas in magma bodies,” *Journal of Volcanology and Geothermal Research*, vol. 108, no. 1, pp. 85–106, 2001. [Online]. Available: <http://www.sciencedirect.com/science/article/pii/S0377027300002791>
- [60] —, “Volatile solubility experimental and theoretical considerations,” *University of Oregon, Conférence universitaire de Suisse occidentale*, pp. 1–25, 2015. [Online]. Available: <http://mineral.cuso.ch/fileadmin/mineral/document/Solubility.pdf>
- [61] J. A. Wolff and J. M. Sumner, “Lava fountains and their products,” In: *Sigurðsson, H., Houghton, B., McNutt, S. R., Rymer, H., Stix, J. (Eds.) Encyclopedia of volcanoes. Academic Press*, 2000.
- [62] *Modeling volcanic processes: the physics and mathematics of volcanism*. Cam-

REFERENCES

- bridge University Press, 2013, ch. Dynamics of magma ascent in the volcanic conduit.
- [63] M. T. Mangan and K. V. Cashman, “The structure of basaltic scoria and reticulite and inferences for vesiculation, foam formation, and fragmentation in lava fountains,” *Journal of Volcanology and Geothermal Research*, vol. 73, no. 1, pp. 1–18, 1996. [Online]. Available: <http://www.sciencedirect.com/science/article/pii/0377027396000182>
 - [64] E. A. Blackburn, L. Wilson, and R. J. Sparks, “Mechanisms and dynamics of strombolian activity,” *Journal of the Geological Society*, vol. 132, no. 4, pp. 429–440, 1976. [Online]. Available: <http://jgs.lyellcollection.org/content/132/4/429.short>
 - [65] J. C. Eichelberger, C. R. Carrigan, H. R. Westrich, and R. H. Price, “Non-explosive silicic volcanism,” *Nature*, vol. 323, no. 6089, pp. 598–602, 1986. [Online]. Available: ftp://seis.es.uwo.ca/pub/pjgonzal/4Pepe/Eichelbergeretal_Nature1986.pdf
 - [66] K. Cashman and J. Blundy, “Degassing and crystallization of ascending andesite and dacite,” *Philosophical Transactions of the Royal Society of London A: Mathematical, Physical and Engineering Sciences*, vol. 358, no. 1770, pp. 1487–1513, 2000. [Online]. Available: <http://rsta.royalsocietypublishing.org/content/358/1770/1487.short>
 - [67] M. M. Morrissey, B. Zimanowski, K. H. Wohletz, and R. Buetner, “Phreatomagmatic fragmentation,” In: *Sigurðsson, H., Houghton, B., McNutt, S. R., Rymer, H., Stix, J. (Eds.) Encyclopedia of volcanoes. Academic Press*, 2000.
 - [68] B. Zimanowski, R. Büttner, V. Lorenz, and H.-G. Häfele, “Fragmentation of basaltic melt in the course of explosive volcanism,” *Journal of Geophysical Research: Solid Earth (1978–2012)*, vol. 102, no. B1, pp. 803–814, 1997. [Online]. Available: <http://onlinelibrary.wiley.com/doi/10.1029/96JB02935/full>
 - [69] P. Kokelaar, “Magma-water interactions in subaqueous and emergent basaltic,” *Bulletin of Volcanology*, vol. 48, no. 5, pp. 275–289, 1986. [Online]. Available: <http://link.springer.com/article/10.1007/BF01081756>
 - [70] B. Zimanowski and K. H. Wohletz, “Physics of phreatomagmatism,” *Terra Nostra, International Maar Conference, Daun, Germany*, vol. 6, pp. 515–523, 2000.
 - [71] A. C. Rust and K. V. Cashman, “Permeability of vesicular silicic

- magma: inertial and hysteresis effects,” *Earth and Planetary Science Letters*, vol. 228, no. 1, pp. 93–107, 2004. [Online]. Available: <http://www.sciencedirect.com/science/article/pii/S0012821X04005771>
- [72] D. L. Sahagian and A. A. Proussevitch, “3d particle size distributions from 2d observations: stereology for natural applications,” *Journal of Volcanology and Geothermal Research*, vol. 84, no. 3, pp. 173–196, 1998. [Online]. Available: <http://www.sciencedirect.com/science/article/pii/S0377027398000432>
- [73] S.-R. Song, K. W. Jones, B. W. Lindquist, B. A. Dowd, and D. L. Sahagian, “Synchrotron x-ray computed microtomography: studies on vesiculated basaltic rocks,” *Bulletin of Volcanology*, vol. 63, no. 4, pp. 252–263, 2001. [Online]. Available: <http://link.springer.com/article/10.1007/s004450100141>
- [74] M. Polacci, D. R. Baker, L. Mancini, G. Tromba, and F. Zanini, “Three-dimensional investigation of volcanic textures by x-ray microtomography and implications for conduit processes,” *Geophysical Research Letters*, vol. 33, no. 13, 2006. [Online]. Available: <http://onlinelibrary.wiley.com/doi/10.1029/2006GL026241/full>
- [75] M. Polacci, D. R. Baker, L. Mancini, S. Favretto, and R. J. Hill, “Vesiculation in magmas from stromboli and implications for normal strombolian activity and paroxysmal explosions in basaltic systems,” *Journal of Geophysical Research: Solid Earth (1978–2012)*, vol. 114, 2009. [Online]. Available: <http://onlinelibrary.wiley.com/doi/10.1029/2008JB005672/full>
- [76] D. R. Baker, L. Mancini, M. Polacci, M. D. Higgins, G. A. R. Gualda, R. J. Hill, and M. L. Rivers, “An introduction to the application of x-ray microtomography to the three-dimensional study of igneous rocks,” *Lithos*, vol. 148, pp. 262–276, 2012. [Online]. Available: <http://www.sciencedirect.com/science/article/pii/S0024493712002319>
- [77] A. LaRue, D. R. Baker, M. Polacci, P. Allard, and N. Sodini, “Can vesicle size distributions assess eruption intensity during volcanic activity?” *Solid Earth*, vol. 4, no. 2, pp. 373–380, 2013. [Online]. Available: <http://www.solid-earth.net/4/373/2013/se-4-373-2013.pdf>
- [78] S. Okumura, M. Nakamura, S. Takeuchi, A. Tsuchiyama, T. Nakano, and K. Uesugi, “Magma deformation may induce non-explosive volcanism via degassing through bubble networks,” *Earth and Planetary Science Letters*, vol. 281, no. 3, pp. 267–274, 2009. [Online]. Available: <http://www.sciencedirect.com/science/article/pii/S0012821X09001381>
- [79] G. A. Gualda and M. Rivers, “Quantitative 3d petrography using x-ray

REFERENCES

- tomography: application to bishop tuff pumice clasts,” *Journal of Volcanology and Geothermal Research*, vol. 154, no. 1, pp. 48–62, 2006. [Online]. Available: <http://www.sciencedirect.com/science/article/pii/S0377027306000424>
- [80] A. A. Proussevitch, D. L. Sahagian, and W. D. Carlson, “Statistical analysis of bubble and crystal size distributions: application to colorado plateau basalts,” *Journal of Volcanology and Geothermal Research*, vol. 164, no. 3, pp. 112–126, 2007. [Online]. Available: <http://www.sciencedirect.com/science/article/pii/S0377027307000960>
- [81] W. Degruyter, A. Burgisser, O. Bachmann, and O. Malaspinas, “Synchrotron x-ray microtomography and lattice boltzmann simulations of gas flow through volcanic pumices,” *Geosphere*, vol. 6, no. 5, pp. 470–481, 2010. [Online]. Available: <http://geosphere.gsapubs.org/content/6/5/470.short>
- [82] M. D. Higgins, “Measurement of crystal size distributions,” *American Mineralogist*, vol. 85, no. 9, pp. 1105–1116, 2000. [Online]. Available: <http://ammin.geoscienceworld.org/content/85/9/1105.short>
- [83] A. Mock and D. A. Jerram, “Crystal size distributions (CSD) in three dimensions: insights from the 3d reconstruction of a highly porphyritic rhyolite,” *Journal of Petrology*, vol. 46, no. 8, pp. 1525–1541, 2005. [Online]. Available: <http://petrology.oxfordjournals.org/content/46/8/1525.short>
- [84] D. J. Morgan and D. A. Jerram, “On estimating crystal shape for crystal size distribution analysis,” *Journal of Volcanology and Geothermal Research*, vol. 154, no. 1, pp. 1–7, 2006. [Online]. Available: <http://www.sciencedirect.com/science/article/pii/S0377027306000382>
- [85] A. A. Proussevitch, D. L. Sahagian, and E. P. Tsentalovich, “Statistical analysis of bubble and crystal size distributions: Formulations and procedures,” *Journal of Volcanology and Geothermal Research*, vol. 164, no. 3, pp. 95–111, 2007. [Online]. Available: <http://www.sciencedirect.com/science/article/pii/S0377027307000972>
- [86] A. C. Rust, M. Manga, and K. V. Cashman, “Determining flow type, shear rate and shear stress in magmas from bubble shapes and orientations,” *Journal of Volcanology and Geothermal Research*, vol. 122, no. 1, pp. 111–132, 2003. [Online]. Available: <http://www.sciencedirect.com/science/article/pii/S0377027302004870>
- [87] A. Toramaru, “BND (bubble number density) decompression rate meter for explosive volcanic eruptions,” *Journal of Volcanology and Geothermal Research*, vol. 154, no. 3, pp. 303–316, 2006. [Online]. Available:

- <http://www.sciencedirect.com/science/article/pii/S0377027306001363>
- [88] M. Masotta, H. Ni, and H. Keppler, “In situ observations of bubble growth in basaltic, andesitic and rhyodacitic melts,” *Contributions to Mineralogy and Petrology*, vol. 167, no. 2, pp. 1–14, 2014. [Online]. Available: <http://link.springer.com/article/10.1007/s00410-014-0976-8>
 - [89] H. Gaonac’h, S. Lovejoy, and D. Schertzer, “Scaling vesicle distributions and volcanic eruptions,” *Bulletin of volcanology*, vol. 67, no. 4, pp. 350–357, 2005. [Online]. Available: <http://link.springer.com/article/10.1007/s00445-004-0376-4>
 - [90] A. G. Simakin, P. Armienti, and M. B. Epel’baum, “Coupled degassing and crystallization: experimental study at continuous pressure drop, with application to volcanic bombs,” *Bulletin of volcanology*, vol. 61, no. 5, pp. 275–287, 1999. [Online]. Available: <http://link.springer.com/article/10.1007/s004450050297>
 - [91] J. D. Blower, J. P. Keating, H. M. Mader, and J. C. Phillips, “Inferring volcanic degassing processes from vesicle size distributions,” *Geophysical research letters*, vol. 28, no. 2, pp. 347–350, 2001. [Online]. Available: <http://onlinelibrary.wiley.com/doi/10.1029/2000GL012188/full>
 - [92] C. Klug, K. Cashman, and C. Bacon, “Structure and physical characteristics of pumice from the climactic eruption of mount mazama (crater lake), oregon,” *Bulletin of Volcanology*, vol. 64, no. 7, pp. 486–501, 2002. [Online]. Available: <http://link.springer.com/article/10.1007/s00445-002-0230-5>
 - [93] S. Lovejoy, H. Gaonac’h, and D. Schertzer, “Bubble distributions and dynamics: The expansion-coalescence equation,” *Journal of Geophysical Research: Solid Earth (1978–2012)*, vol. 109, 2004. [Online]. Available: <http://onlinelibrary.wiley.com/doi/10.1029/2003JB002823/full>
 - [94] D. Sahagian, “Bubble migration and coalescence during the solidification of basaltic lava flows,” *The Journal of Geology*, pp. 205–211, 1985. [Online]. Available: <http://www.jstor.org/stable/30066297>
 - [95] H. Gaonac’h, S. Lovejoy, J. Stix, and D. Schertzer, “A scaling growth model for bubbles in basaltic lava flows,” *Earth and Planetary Science Letters*, vol. 139, no. 3, pp. 395–409, 1996. [Online]. Available: <http://www.sciencedirect.com/science/article/pii/0012821X96000398>
 - [96] E. R. Johnson, P. J. Wallace, K. V. Cashman, H. D. Granados, and A. J. Kent, “Magmatic volatile contents and degassing-induced

REFERENCES

- crystallization at volcan jorullo, mexico: implications for melt evolution and the plumbing systems of monogenetic volcanoes,” *Earth and Planetary Science Letters*, vol. 269, no. 3, pp. 478–487, 2008. [Online]. Available: <http://www.sciencedirect.com/science/article/pii/S0012821X08001593>
- [97] M. E. Hartley, J. MacLennan, M. Edmonds, and T. Thordarson, “Reconstructing the deep CO₂ degassing behaviour of large basaltic fissure eruptions,” *Earth and Planetary Science Letters*, vol. 393, pp. 120–131, 2014. [Online]. Available: <http://www.sciencedirect.com/science/article/pii/S0012821X14001125>
- [98] A. S. Lloyd, “Timescales of magma ascent during explosive eruptions: Insights from the re-equilibration of magmatic volatiles,” 2014. [Online]. Available: <http://academiccommons.columbia.edu/catalog/ac:176973>
- [99] P. Moitra, H. M. Gonnermann, B. F. Houghton, and T. Giachetti, “Relating vesicle shapes in pyroclasts to eruption styles,” *Bulletin of volcanology*, vol. 75, no. 2, pp. 1–14, 2013. [Online]. Available: <http://link.springer.com/article/10.1007/s00445-013-0691-8>
- [100] H. M. Wright, K. V. Cashman, E. H. Gottesfeld, and J. J. Roberts, “Pore structure of volcanic clasts: measurements of permeability and electrical conductivity,” *Earth and Planetary Science Letters*, vol. 280, no. 1, pp. 93–104, 2009. [Online]. Available: <http://www.sciencedirect.com/science/article/pii/S0012821X0900034X>
- [101] A. B. Clarke, A. Neri, B. Voight, G. Macedonio, and T. H. Druitt, “Computational modelling of the transient dynamics of the august 1997 vulcanian explosions at soufriere hills volcano, montserrat: influence of initial conduit conditions on near-vent pyroclastic dispersal,” *MEMOIRS-GEOLOGICAL SOCIETY OF LONDON*, vol. 21, pp. 319–348, 2002. [Online]. Available: http://www.researchgate.net/profile/B_Voight/publication/249552807_Computational_modelling_of_the_transient_dynamics_of_the_August_1997_Vulcanian_explosions_at_Soufriere_Hills_Volcano_Montserrat_influence_of_initial_conduit_conditions_on_near-vent_pyroclastic_dispersal/links/0deec5240ae586cade000000.pdf
- [102] O. Melnik and R. S. J. Sparks, “Dynamics of magma ascent and lava extrusion at soufrière hills volcano, montserrat,” *Geological Society, London, Memoirs*, vol. 21, no. 1, pp. 153–171, 2002. [Online]. Available: <http://mem.lyellcollection.org/content/21/1/153.short>
- [103] —, “Modelling of conduit flow dynamics during explosive activity at soufrière hills volcano, montserrat,” *Geological Society, London*,

- Memoirs*, vol. 21, no. 1, pp. 307–317, 2002. [Online]. Available: <http://mem.lyellcollection.org/content/21/1/307.short>
- [104] H. M. Gonnermann and M. Manga, “Explosive volcanism may not be an inevitable consequence of magma fragmentation,” *Nature*, vol. 426, no. 6965, pp. 432–435, 2003. [Online]. Available: <http://www.nature.com/articles/nature02138>
- [105] D. A. Huerta, V. Sosa, M. C. Vargas, and J. C. Ruiz-Suárez, “Archimedes’ principle in fluidized granular systems,” *Physical Review E*, vol. 72, no. 3, p. 031307, 2005. [Online]. Available: <http://journals.aps.org/pre/abstract/10.1103/PhysRevE.72.031307>
- [106] T. G. team, “Gnu image manipulation program,” *GIMP 2.8.14*, 1997-2014. [Online]. Available: www.gimp.org
- [107] W. Rasband, “Imagej,” *U.S. National Institutes of Health, Bethesda, Maryland, USA*, 1997-2014. [Online]. Available: <http://imagej.nih.gov/ij/>
- [108] W. K. Stovall, B. F. Houghton, H. Gonnermann, S. A. Fagents, and D. A. Swanson, “Eruption dynamics of Hawaiian-style fountains: the case study of episode 1 of the Kīlauea Iki 1959 eruption,” *Bulletin of volcanology*, vol. 73, no. 5, pp. 511–529, 2011. [Online]. Available: <http://link.springer.com/article/10.1007/s00445-010-0426-z>
- [109] L. G. Mastin, “A user-friendly one-dimensional model for wet volcanic plumes,” *Geochemistry, Geophysics, Geosystems*, vol. 8, no. 3, 2007. [Online]. Available: <http://onlinelibrary.wiley.com/doi/10.1029/2006GC001455/full>
- [110] G. Rolandi, S. Maraffi, P. Petrosino, and L. Lirer, “The Ottaviano eruption of Somma-Vesuvio (8000 y BP): a magmatic alternating fall and flow-forming eruption,” *Journal of Volcanology and Geothermal Research*, vol. 58, no. 1, pp. 43–65, 1993. [Online]. Available: <http://www.sciencedirect.com/science/article/pii/037702739390101V>
- [111] S. Carey and H. Sigurdsson, “The intensity of plinian eruptions,” *Bulletin of Volcanology*, vol. 51, no. 1, pp. 28–40, 1989. [Online]. Available: <http://link.springer.com/article/10.1007/BF01086759>
- [112] J. G. Moore and J.-G. Schilling, “Vesicles, water, and sulfur in Reykjanes Ridge basalts,” *Contributions to Mineralogy and Petrology*, vol. 41, no. 2, pp. 105–118, 1973. [Online]. Available: <http://link.springer.com/article/10.1007/BF00375036>

REFERENCES

- [113] B. F. Houghton, C. J. N. Wilson, and I. E. M. Smith, “Shallow-seated controls on styles of explosive basaltic volcanism: a case study from New Zealand,” *Journal of Volcanology and Geothermal Research*, vol. 91, no. 1, pp. 97–120, 1999. [Online]. Available: <http://www.sciencedirect.com/science/article/pii/S037702739900058X>
- [114] N. C. Lautze and B. F. Houghton, “Physical mingling of magma and complex eruption dynamics in the shallow conduit at Stromboli volcano, Italy,” *Geology*, vol. 33, no. 5, pp. 425–428, 2005. [Online]. Available: <http://geology.gsapubs.org/content/33/5/425.short>
- [115] L. Costantini, B. F. Houghton, and C. Bonadonna, “Constraints on eruption dynamics of basaltic explosive activity derived from chemical and microtextural study: the example of the Fontana Lapilli Plinian eruption, Nicaragua,” *Journal of Volcanology and Geothermal Research*, vol. 189, no. 3, pp. 207–224, 2010. [Online]. Available: <http://www.sciencedirect.com/science/article/pii/S0377027309004405>
- [116] C. Klug and K. V. Cashman, “Vesiculation of May 18, 1980, Mount St. Helens magma,” *Geology*, vol. 22, no. 5, pp. 468–472, 1994. [Online]. Available: <http://geology.gsapubs.org/content/22/5/468.short>
- [117] D. B. Dingwell, “The glass transition in hydrous granitic melts,” *Physics of the Earth and Planetary Interiors*, vol. 107, no. 1, pp. 1–8, 1998. [Online]. Available: <http://www.sciencedirect.com/science/article/pii/S0031920197001192>
- [118] B. F. Houghton, C. J. N. Wilson, P. Del Carlo, M. Coltelli, J. E. Sable, and R. Carey, “The influence of conduit processes on changes in style of basaltic Plinian eruptions: Tarawera 1886 and Etna 122 BC,” *Journal of Volcanology and Geothermal Research*, vol. 137, no. 1, pp. 1–14, 2004. [Online]. Available: <http://www.sciencedirect.com/science/article/pii/S0377027304001581>
- [119] C. Jaupart, “Gas loss from magmas through conduit walls during eruption,” *Geological Society, London, Special Publications*, vol. 145, no. 1, pp. 73–90, 1998. [Online]. Available: <http://sp.lyellcollection.org/content/145/1/73.short>
- [120] M. V. Stasiuk, J. Barclay, M. R. Carroll, C. Jaupart, J. C. Ratté, R. S. J. Sparks, and S. R. Tait, “Degassing during magma ascent in the Mule Creek vent (USA),” *Bulletin of Volcanology*, vol. 58, no. 2-3, pp. 117–130, 1996. [Online]. Available: <http://link.springer.com/article/10.1007/s004450050130>
- [121] T. Thordarson, S. Self, N. Oskarsson, and T. Hulsebosch, “Sulfur, chlorine, and fluorine degassing and atmospheric loading by the 1783–1784 AD Laki

REFERENCES

(Skaftár Fires) eruption in Iceland,” *Bulletin of Volcanology*, vol. 58, no. 2-3, pp. 205–225, 1996. [Online]. Available: <http://link.springer.com/article/10.1007/s004450050136>

A. Appendix

Table A.1: Vesicularity values for samples; index (mean vesicularity), range, maximum value, minimum value.

Sample	Vesicularity Index (%)	Range (%)	Max (%)	Min (%)
13P	85.4	63.6	92.8	29.2
12P	87.8	57.3	91.7	34.4
7P	81.8	80.2	91.4	11.2
21P	84.0	28.0	91.3	63.3
20P	81.8	22.9	89.7	66.8
19P	78.7	50.1	91.3	41.2
18P	79.5	30.4	86.2	55.8
17P	81.2	29.9	87.0	57.0
16P	82.7	36.1	88.6	52.5
15P	79.2	72.4	86.5	14.1
14P	79.1	52.9	89.7	36.8
28P	79.5	58.1	93.6	35.5